الجـــــــــــــــمهـوريـــة
الجـــــــــزائرية الديمـــــقراطية
الشـــــــعبية

People's Democratic Republic of Algeria

وزارة
التـــــــــــــــعليـم
العـــــالي والبـــــحث العـــلمـي

Ministry of Higher Education and Scientific Research

جـــــــــامعة أبي بكـر بلقـايد –
تـلمســـــــان –

University of Aboubakr Belkaïd –Tlemcen– Faculty of Technology

Laboratory of Computational Mechanics

THESIS

Presented for obtaining the degree of DOCTORATE 3rd Cycle

In Mechanical Engineering

Specialty Mechanical Construction

Presented by Ahmed SAIM

Subject

Dynamic of non-uniform rotors made of axially functionally graded materials

Dynamique des rotors non uniformes en matériaux à gradient évalué axialement

Public defense of this dissertation took place on **October 9, 2025**, before the jury of the thesis committee:

AMIRAT Mohamed	**Professor**	Univ. Tlemcen	**Chairman**
BOUKHALFA Abdelkrim	**Professor**	Univ. Tlemcen	**Supervisor**
HAMZA CHERIF Sidi Mohammed	**Professor**	Univ. Tlemcen	**Examiner** 1
SERDOUN Sidi Mohammed Nadjib	**Assoc. Prof. 'A'**	ESSAT. Tlemcen.	**Examiner** 2


بِسْمِ ٱللَّهِ ٱلرَّحْمَٰنِ ٱلرَّحِيمِ

In the name of Allah, the Most Gracious, the Most Merciful.

I dedicate this thesis to my Creator, whose infinite mercy and guidance have illuminated every step of my journey.

To my beloved mother, whose unconditional love, sacrifices, and prayers have been my greatest source of strength.

To the cherished memory of my father—may Allah grant him eternal peace—whose values and teachings continue to inspire and guide me.

To my dear brothers and sisters, for their constant encouragement, support, and belief in me.

To my colleagues and friends, whose companionship and encouragement made this path more meaningful and fulfilling.

To my supervisor(s), for their invaluable guidance, patience, and unwavering support throughout this work.

And finally, to my university, for providing me with the knowledge, resources, and foundation upon which this academic journey was built.

Declaration

I, Ahmed SAIM, hereby declare that this thesis is my original work and has not been submitted for any other degree or examination at any university. All sources of information and assistance used in this thesis have been acknowledged. I understand that any act of plagiarism or academic dishonesty may lead to severe consequences.

Ahmed SAIM
صايم احمد

2025

Acknowledgements

I begin by expressing my deepest gratitude to Allah, whose divine guidance has illuminated my path and granted me the strength to overcome every challenge.

I would like to extend my heartfelt appreciation to my dedicated supervisor, Professor Abdelkrim Boukhalfa, whose wisdom, guidance, and mentorship have been instrumental in shaping this research.

I am deeply grateful to my examiners, Professor Mohamed Amirat, dProfessor Sidi Mohammed Hamza Cherif and Associate Professor Sidi Mohammed Nadjib Serdoun, for graciously accepting the responsibility of evaluating my work and for their insightful feedback that has enriched the quality of this thesis.

My sincere thanks go as well to, all members of the MecaComp Laboratory, my peers, and the broader scientific community for fostering an environment of intellectual growth and collaboration.

I am especially grateful to my colleagues at work for their invaluable assistance during this critical period. Their unwavering support and encouragement went above and beyond, greatly enhancing both my productivity and my well-being.

To my cherished family and friends, whose love, patience, and constant encouragement have been my greatest pillar of strength, I owe a profound debt of gratitude. This achievement is as much yours as it is mine, for you have been the foundation upon which my academic journey was built.

ABSTRACT

Cette étude présente une analyse numérique du comportement de tourbillonnement d'un arbre creux non uniforme en rotation, constitué de matériaux à gradient fonctionnel axial (FGM). The material properties vary continuously along the axial direction according to a power-law distribution. Using Timoshenko beam theory, the shaft is modeled with the p-version of the finite element method (FEM), while Lagrange's formalism is applied to derive the differential equations governing the motion of the rotating system. The proposed model is used to analyze the system's whirl frequencies, critical spinning speeds, and the influence of key parameters on the behavior and stability of dimensionless natural frequencies. These parameters include the slenderness ratio, material composition, radius variation, variable rotating speed, and power-law index, evaluated under various boundary conditions (B.C.). The effects of these factors performance of spinning hollow non-uniform shaft are understood. The validity of the proposed model is confirmed through comprehensive comparisons of numerical and analytical results with existing data in the literature. This work paves the way for innovative industrial applications in advanced rotating structures.

KEYWORDS

Spinning hollow shaft; non-uniform profile; axially FGM; whirling frequency; Timoshenko beam theory

الملخّص

تقدِّم هذه الدراسةُ تحليلًا عدديًا لسلوك الاهتزازات الدوّامية (التوربيلونية) لعمودٍ أجوفٍ غير منتظم الشكل يدور ويتكوَّن تتغيّر خصائص المادة تدريجيًا على طول الاتجاه المحوري وفق .(FGM) من مواد متدرّجة الخواص على طول المحور تمّ نمذجة العمود بالاعتماد ،(Timoshenko Beam Theory) قانونٍ أسيٍّ للقدرة. باستخدام نظرية العتبات لتيموشينكو بينما استُخدم المنهج اللاغرانجي لاشتقاق المعادلات ،(FEM p-version) من طريقة العناصر المحدودة p على النسخة التفاضلية التي تحكم حركة النظام الدوّار. يُستعمل النموذج المقترح لتحليل ترددات الاهتزازات الدوّامية للنظام والسرعات الحرجة للدوران، ودراسة تأثير المعاملات الرئيسية على استقرار وسلوك الترددات الطبيعية غير البعدية. وتشمل هذه المعاملات نسبة النحافة، تركيب المادة، تغيّر نصف القطر، سرعة الدوران المتغيّرة، ومعامل قانون القدرة، وذلك تحت شروط تقييد مختلفة. أُكِّدت صحة النموذج المقترح من خلال مقارنات عددية وتحليلية شاملة مع نتائج منشورة في المراجع السابقة، مما يثبت دقّته وكفاءته. تُمهِّد هذه النتائج الطريق نحو تطبيقات صناعية مبتكرة في مجال الهياكل الدوّارة المتقدّمة.

الكلمات المفتاحية :

نظرية عتبة –تردد دوّامي – (FGM)مواد متدرّجة الخواص محوريًا –مقطع غير منتظم –عمود أجوف دوّار تيموشينكو.

RÉSUMÉ

Cette étude présente, pour la première fois, une étude numérique du comportement tourbillonnaire d'un arbre non-uniforme creux en rotation, composé de matériaux à gradient fonctionnel axial (MGF). Les propriétés du matériau varient continûment le long de la direction axiale selon une loi de puissance. En utilisant la théorie des poutres de Timoshenko, l'arbre est modélisé par la version p de la méthode des éléments finis (MEF), tandis que le formalisme de Lagrange est appliqué pour dériver les équations différentielles régissant le mouvement du système en rotation. Le modèle proposé est utilisé pour analyser les fréquences de tourbillonnement du système, les vitesses critiques de rotation et l'influence de paramètres clés sur le comportement et la stabilité des fréquences naturelles adimensionnelles. Ces paramètres comprennent l'élancement, la composition du matériau, la variation du rayon, la vitesse de rotation variable et l'indice de loi de puissance, évalués sous diverses conditions aux limites (C.L.). Les effets de ces facteurs sur les performances d'un arbre non-uniforme creux en rotation sont compris. La validité du modèle proposé est confirmée par des comparaisons exhaustives des résultats numériques et analytiques avec les données existantes dans la littérature. Ces travaux ouvrent la voie à des applications industrielles innovantes dans les structures rotatives avancées.

MOTS CLÉS :

Arbre creux tournant ; profil non-uniforme ; FGM axial ; fréquence de tourbillonnement ; théorie de la poutre de Timoshenko.

Contents

Contents

List of figures

List of tables

Nomenclature

V (x, y, z)	Displacement in y direction.
W (x, y, z)	Displacement in z direction.
β_x	Rotation angles of the cross-section about the y-axis.
β_y	Rotation angles of the cross-section, about the z-axis.
(x, y, z)	Cartesian coordinates.
(x, r, θ)	Cylindrical coordinates.
E	Young modulus.
ρ	Masse density.
ν	Poisson coefficient.
n	Power law index.
ω	Natural frequency, eigen-value.
ω^*	Dimensionless frequency.
Ω	Rotational speed
$\boldsymbol{\alpha}$	Radius coefficient.
ξ	Local and non-dimensional co-ordinates.
L	Length.
Q_{ij}	Elastic constants.
R_i	Inner Radius.
R_1	Radius at $x = 0$.

R_2	Radius at $x = L$.
R(x)	Radius at $0 < x < L$.
$\{q_i\}$	Generalized coordinates, with (i = V, W, β_x, β_y).
$[N]$	Matrix of the shape functions.
$[M]$	Mass matrix.
$[K]$	Stiffness matrix. Gyroscopic
$[G]$	Gyroscopic matrix.
E_C	Kinetic energy.
E_d	Strain energy.
P	Number of the shape functions or number of hierarchical terms.
K_s	Shear correction factor.

General Introduction

General Introduction

Rotating machinery—such as pumps, compressors, turbines, and high-speed spindles—plays a crucial role in a wide range of industrial applications, including power generation, aerospace, petrochemical processes, and advanced manufacturing. Improving their efficiency and operational performance often requires increasing the rotational speed. However, during operation, the natural frequencies of such systems are strongly influenced by the rotation speed. This interdependence can lead to severe dynamic issues, particularly resonance, which threatens both structural integrity and operational reliability. Consequently, accurate prediction of critical rotational speeds and detailed dynamic analysis are essential to ensure stability and prevent failure.

In recent decades, the use of Functionally Graded Materials (FGMs) has become an effective approach to enhance the performance of structural and rotating components. FGMs exhibit a continuous spatial variation of mechanical properties, enabling smooth transitions between different material phases. This unique characteristic minimizes stress concentrations, improves strength-to-weight ratios, and increases resistance to thermal and dynamic loads—making them ideal candidates for high-speed rotating systems.

Problematic

- Despite the advantages of FGMs, the dynamic behavior of rotors made of axially graded materials remains complex due to several interrelated factors:
- Spatial variation of the physical properties of FGM rotors;
- Complex geometric configurations (non-uniform shapes, hollow or variable-radius profiles);
- Influence of the gradient parameter, radius ratio (L/R), rotational speed, and boundary conditions;
- Absence of reliable experimental validations.
- These challenges highlight the need for an accurate and adaptable numerical model capable of describing the whirling behavior, stability, and critical speeds of rotating FGM shafts under various physical and geometrical conditions.

Main Challenges

- The study of FGM rotors presents several major challenges:
- Capturing the coupled effects of material gradation, geometry, and rotation speed on dynamic behavior;
- Developing a robust numerical method capable of accurately predicting whirl frequencies and critical speeds;
- Integrating gyroscopic effects and variable material properties into the governing equations;
- Validating the developed model against available analytical and numerical results.

Novelty and Research Objectives

This research introduces a numerical model for the dynamic analysis of hollow, non-uniform FGM rotors with axial gradation, incorporating gyroscopic effects. The originality lies in the application of the p-version of the Finite Element Method (FEM), which improves computational accuracy by enriching the polynomial order of the shape functions instead of refining the mesh. The proposed model enables an in-depth investigation of how gradient parameters, geometry, rotation speed, and boundary conditions influence the whirling frequencies, critical rotational speeds, and stability of such systems.

Objectives

- Develop a MATLAB program based on the p-version FEM for the modal analysis of flexible, axially graded rotors.
- Study the influence of mechanical and geometrical parameters (slenderness ratio, gradient index, radius variation, rotational speed, and boundary conditions) on dimensionless natural frequencies.
- Construct the Campbell diagram to identify and interpret critical rotational speeds.
- Validate the proposed model by comparing the obtained results with analytical and numerical data available in the literature.
- Provide insights for the design optimization of advanced rotating structures using FGMs.

Thesis Structure

This thesis is organized into six chapters:

- **Chapter I** introduces the fundamentals of rotor dynamics and composite materials, with a special focus on axially Functionally Graded Materials (FGMs) and their mechanical advantages.
- **Chapter II** presents the beam theories used for modeling rotating shafts, including the Timoshenko theory, which captures shear deformation and rotary inertia effects. The strain and kinetic energy formulations are developed using the Lagrangian formalism.
- **Chapter III** details the numerical modeling using the p-version of FEM, highlighting its formulation, discretization, and advantages for dynamic analysis of non-uniform FGM rotors.
- **Chapter IV** describes the MATLAB implementation, including input parameters, matrix formulation, assembly, and eigenvalue problem solution.
- **Chapter V** presents the numerical results, analyzing the influence of different parameters on whirl frequencies and critical speeds. Campbell diagrams are used to visualize frequency evolution, and comparisons with literature results validate the model.
- **Chapter VI** concludes the work, summarizes the main findings, and suggests perspectives for future research in the dynamic modeling of advanced rotating systems.

.

Chapter 1

1. Literature review

1.1. Dynamics of rotors

1.1.1. Introduction

The continuous progress in industrial technologies imposes growing demands in terms of mechanical performance, energy efficiency, and reliability, especially for rotating machinery such as turbines (figure 1.1), compressors (figure 1.2), engines (figure 1.3), and pumps (figure 1.4). These machines are built around rotors, which serve as critical elements ensuring the transmission of power and the structural integrity of the system during high-speed rotation. However, operating under such conditions subjects rotors to complex dynamic phenomena gyroscopic effects, centrifugal forces, unbalances, and critical resonances that may compromise stability or induce fatigue and vibrations. This makes the dynamic study of rotors a vital field in applied mechanics, focusing on the analysis of vibratory behavior under various configurations and operating conditions. Since the pioneering works of Stodola and Jeffcott in the early 20th century, rotor modeling has evolved to incorporate more complex systems, including multiple disks, non-uniform geometries, damping, and hydrodynamic bearings. These developments have led to modern models capable of accurately predicting dynamic responses using numerical methods such as the finite element method (FEM), now essential for the safe and optimized design of rotating components.

In parallel, the emergence of advanced materials, particularly functionally graded materials (FGMs), has opened new pathways for enhancing the mechanical and thermal performance of structural elements. Introduced in Japan in the 1980s, FGMs are characterized by a gradual and continuous variation of their physical properties such as stiffness, density, or thermal conductivity typically along a specific direction. This tailored gradation eliminates abrupt interfaces and reduces stress concentrations, common issues in traditional composite materials. FGMs combine the advantages of metals and ceramics to offer superior strength, heat resistance, and corrosion protection, making them ideal for aerospace, energy, and space applications. In the context of rotating structures, incorporating FGMs allows not only for a more efficient material distribution but also for enhanced resistance to vibrational instabilities. Despite their potential, the dynamic behavior of non-uniform hollow rotors made from axially graded FGMs remains relatively underexplored. In particular, the influence of geometric

variation coupled with power-law-based material gradation has not been thoroughly addressed in the literature.

This thesis contributes to filling this gap by presenting, for the first time, a comprehensive numerical investigation of the whirling dynamics of a hollow, non-uniform rotor composed of axially graded FGM. The Timoshenko beam theory, which accounts for shear deformation and rotary inertia, is adopted alongside the p-version of the finite element method to derive the system's characteristic matrices mass, stiffness, and gyroscopic. The equations of motion are established using Lagrangian formalism. The model is then implemented in a computational program, and validated through comparison with existing results. Several case studies are performed to assess the impact of key parameters such as the slenderness ratio, radius variation, power-law index, material distribution, and boundary conditions on the system's natural frequencies and stability thresholds. Ultimately, this study not only deepens the understanding of FGM rotor behavior under complex dynamic loads but also provides a solid foundation for the design of more resilient and efficient rotating machinery in advanced engineering fields.

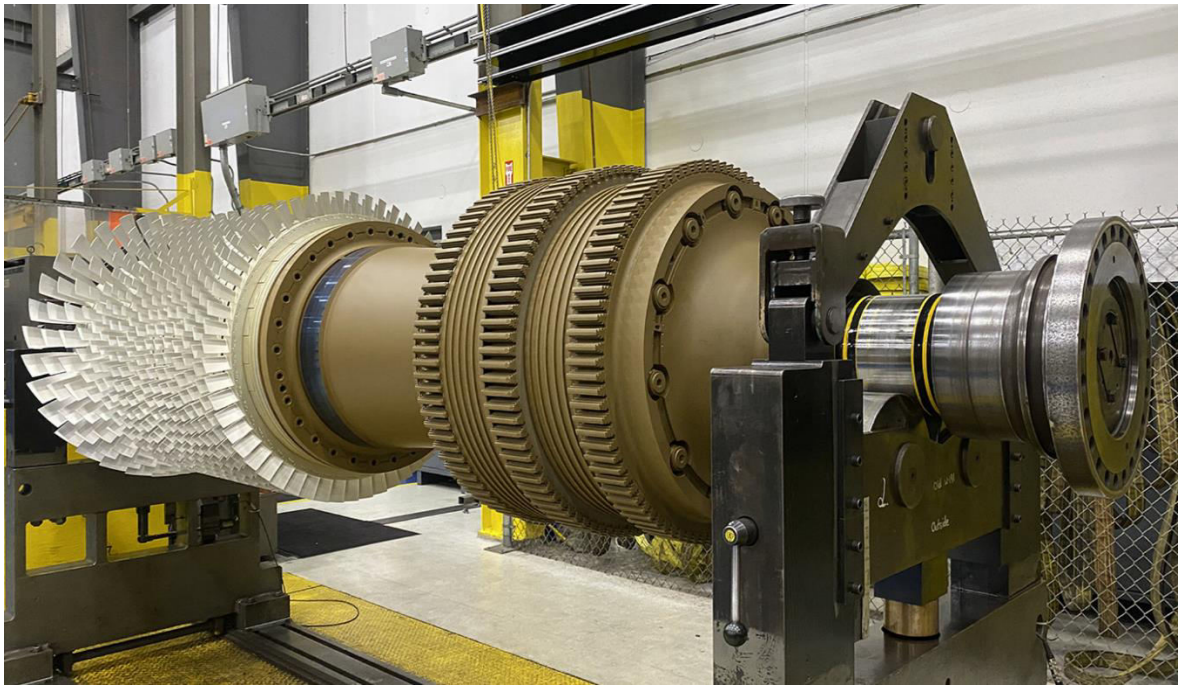

Fig 1. 1 Gas turbine shaft [1]

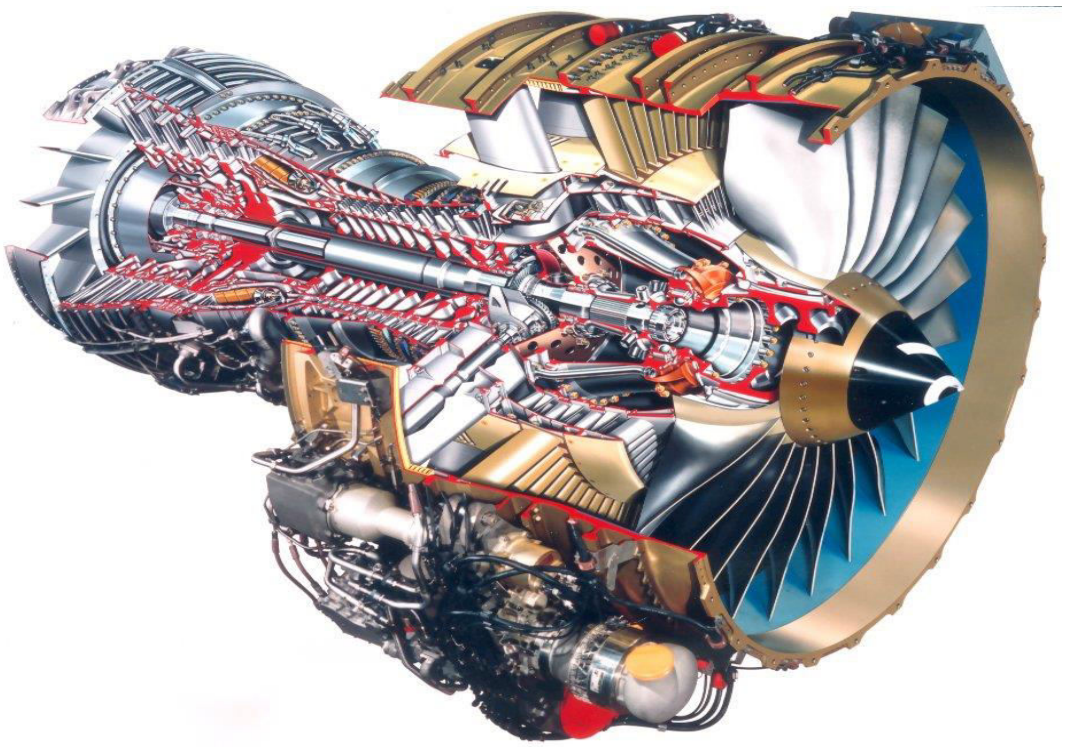

Fig 1. 2 Turbocharger [2]

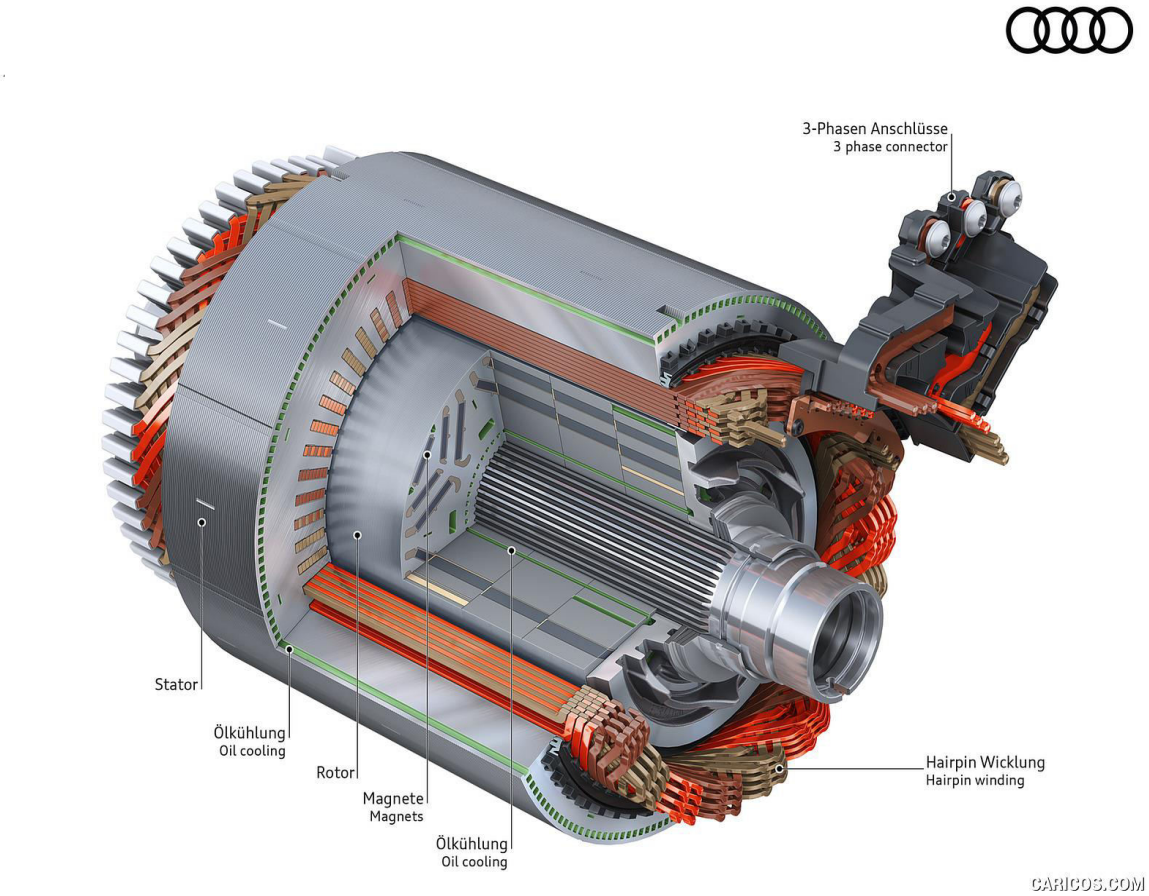

Fig 1. 3 Rotor and stator of the rear-mounted electric motor (permanently excited synchronous machine – PSM) [3]

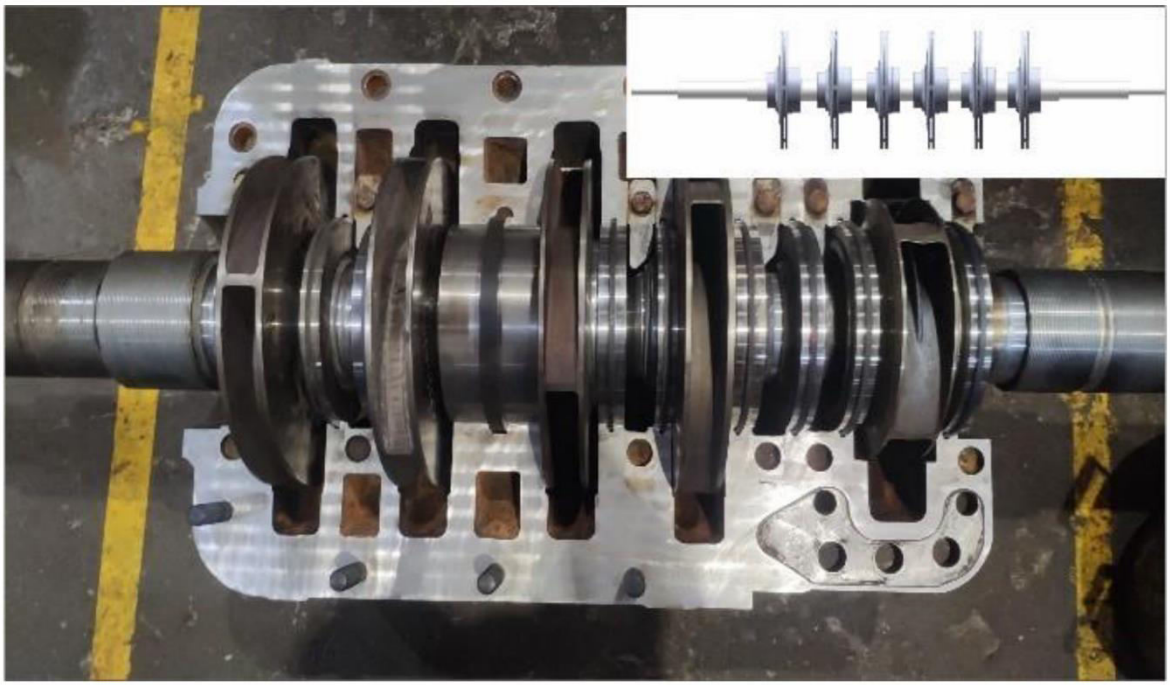

Fig 1. 4 Mechanical layout of a real multi-stage centrifugal pump [4]

1.1.2. Brief history of non-uniform rotors

The development of rotor dynamics as a field dates back to the late 19th and early 20th centuries, primarily in response to the growing need to understand the behavior of rotating machinery, such as turbines, generators, and compressors. Early investigations, such as those by Rankine (1869) and Stodola (1903), focused on uniform rotors with simple geometry and constant material properties. These foundational works laid the groundwork for the classical rotor dynamics theories, which typically assumed idealized, symmetric shaft configurations. However, real-world rotors often deviate from these assumptions due to manufacturing tolerances, design constraints, material distribution, or operational requirements. This led to the emergence of the concept of non-uniform shaft, i.e., rotors with variations in geometry such as conicity or step changes in diameter Figure 1.5, and Figure 1.6.

Fig 1. 5 Concept of non-uniform shaft [5]

Such variations have significant effects on the rotor's mass and stiffness distributions, influencing their dynamic behavior, including critical speeds, mode shapes, and stability.

The first substantial studies that acknowledged rotor non-uniformity appeared in the mid-20th century, particularly as analytical and numerical methods advanced. Timoshenko's beam theory (1921), which incorporated shear deformation and rotary inertia, provided a more accurate framework for analyzing non-uniform shafts compared to the earlier Euler-Bernoulli beam model. Later developments saw this theory being adapted to analyze rotors with tapered geometries and variable cross-sections [6]. In the 1960s and 1970s, researchers began to employ finite element methods (FEM) to solve increasingly complex rotor dynamics problems.

Fig 1. 6 Shaft with variable section [7]

This computational advancement allowed the modeling of rotors with arbitrary non-uniform profiles, stepped diameters, and graded materials. Notably, Gunter and his collaborators introduced early FEM formulations for rotor systems that could accommodate geometric discontinuities and support flexibility. The emergence of functionally graded materials (FGMs) in the 1980s and 1990s further stimulated interest in non-uniform rotors. These advanced materials feature continuous variation in composition and structure, leading to smooth gradients in mechanical properties. Incorporating FGMs into rotating shafts introduced new challenges, particularly regarding how material gradation interacts with geometric non-uniformity to affect the system's dynamic response [8].

By the early 2000s, the modeling of axially functionally graded rotors with non-uniform geometry became more common in aerospace, energy, and biomedical applications. Advanced formulations combining Timoshenko beam theory, Lagrangian mechanics, and refined FEM

enabled detailed analysis of these complex systems under various loading and boundary conditions [9].

Recent research trends focus on the nonlinear dynamic analysis of non-uniform rotors, including the effects of gyroscopic moments, thermal gradients, crack propagation, and material damping. Studies by Rao (2009) and Friswell (2010) emphasized the role of non-uniformity in predicting instabilities and improving rotor reliability. The coupling between structural gradation, geometric asymmetry, and operational parameters like rotation speed and temperature has become central in modern rotor design.

Today, non-uniform rotors are a subject of active research, especially in the context of smart materials, additive manufacturing, and rotor-based energy systems. The accurate prediction of their vibrational characteristics remains a critical area, especially for high-speed and mission-critical rotating machinery.

1.1.3. Dynamics of non-uniform rotors made functionally graded materials (FGM)

Non-uniform rotors constitute a specialized category of rotating machinery components in which the geometry varies along the axial direction. These variations may involve changes in diameter, wall thickness, or complex profiles such as conical, frustoconical, parabolic, or exponential shapes. When these rotors are manufactured using functionally graded materials (FGMs), their dynamic behavior becomes even more intricate due to the combined influence of geometry and material gradation.

FGMs are engineered composites that exhibit a gradual and continuous variation of material properties such as Young's modulus, density, or Poisson's ratio across one or more spatial dimensions. This gradation allows designers to tailor the mechanical and thermal performance of components more effectively than with conventional homogeneous materials. In non-uniform FGM rotors, this variation is superimposed on the geometric non-uniformity, leading to non-linear distributions of mass, stiffness, and damping. These variations significantly influence key dynamic characteristics, including natural frequencies, critical speeds, vibration modes, and system stability.

Analyzing such systems demands advanced modeling techniques. Classical beam theories, like Euler–Bernoulli, are often insufficient for capturing the full complexity of short or thick rotors. Instead, Timoshenko beam theory is commonly employed, as it accounts for shear deformation and rotary inertia. The inclusion of gyroscopic effects is also crucial, particularly in high-speed

applications. Finite element methods (FEM) are widely adopted for their ability to model both geometric and material gradients using power-law or exponential functions to describe the spatial variation of properties.

This modeling approach facilitates the prediction of vibrational behavior, the identification of instabilities, and the design optimization of rotors subjected to complex loading and boundary conditions. In addition, the use of FGMs in non-uniform rotors has shown potential in enhancing structural integrity, reducing weight, and extending service life. Such rotors are increasingly relevant in advanced sectors such as aerospace, energy, and biomechanics, where performance and reliability are paramount.

Nevertheless, the coupling between geometry and material gradients presents significant challenges in mathematical formulation, numerical implementation, and experimental validation. Continued advancements in computational modeling and additive manufacturing are expected to further enhance the practical application of non-uniform FGM rotors.

1.2. Functionally Graded Materials (FGMs)

1.2.1. Introduction

Functionally graded materials (FGMs) are a class of advanced composite materials characterized by a continuous variation in composition and structure, designed to achieve specific spatial property gradients. Unlike traditional composites that often suffer from abrupt interfaces between dissimilar materials, FGMs provide a smooth transition from one constituent to another most commonly between a metal and a ceramic offering an innovative solution to many of the limitations inherent in conventional laminated or layered materials. The concept of FGMs emerged in the late 1980s, primarily in Japan, driven by the need for materials capable of withstanding extreme thermal gradients in aerospace and nuclear environments. Since then, FGMs have evolved significantly, finding applications across a wide spectrum of disciplines, including biomechanics, aerospace, energy systems, defense technologies, and thermal barrier coatings. This versatility stems from their ability to tailor mechanical, thermal, and chemical properties according to functional requirements by controlling the spatial distribution of their constituents.

FGMs are typically engineered by varying the volume fraction of two or more base materials across a given dimension axially, radially, or even in multiple directions. This gradation leads to corresponding changes in material properties such as Young’s modulus, thermal co

nductivity, density, and thermal expansion coefficient. The most common gradation profiles follow power-law, exponential, or sigmoid distributions, and these are mathematically formulated to predict the effective properties of the composite using homogenization techniques such as the rule of mixtures, Mori–Tanaka scheme, or Voigt–Reuss models. One of the key advantages of FGMs lies in their ability to resist stress concentrations and delamination that are common in traditional multi-material assemblies. In thermally demanding environments, for instance, ceramic-to-metal FGMs provide excellent thermal resistance on one side (the ceramic-rich surface) while maintaining toughness and structural support on the metal-rich side. This unique property makes them ideal for components subjected to high thermal and mechanical loads, such as heat shields, turbine blades, and nuclear reactor walls. In addition to their thermal and mechanical advantages, FGMs also offer enhanced corrosion and wear resistance, tailored biocompatibility for implants, and acoustic insulation in dynamic systems. Their performance can be finely adjusted not only during design but also during fabrication using advanced manufacturing techniques such as powder metallurgy, additive manufacturing (e.g., direct energy deposition, selective laser melting), centrifugal casting, or chemical vapor deposition.

The design and analysis of FGMs involve a multidisciplinary approach combining materials science, mechanics of continua, computational modeling, and manufacturing engineering. Because of the inherent complexity of their material gradients, analytical and numerical methods play a crucial role in predicting the behavior of FGMs under static, dynamic, and thermal loading conditions. Modern finite element analysis (FEA) tools are particularly well suited for simulating FGM behavior and are widely used to optimize gradient profiles for desired performance outcomes.

In conclusion, functionally graded materials represent a major advancement in the field of materials engineering, offering the potential to design components with unprecedented performance and multifunctionality. As the demand for high-performance materials continues to grow in critical technological sectors, the importance of FGMs is expected to increase, with ongoing research aimed at expanding their capabilities, improving their manufacturability, and integrating them into next-generation structural and functional systems.

1.2.2. Overview of the history of functionally graded materials FGM

The concept of functionally graded materials (FGMs) emerged in the 1980s as a response to growing challenges in high-performance engineering applications, particularly in aerospace and nuclear industries. Traditional composite materials often composed of discrete layers of metals

and ceramics were prone to mechanical failure due to sharp interfaces between materials with mismatched thermal and mechanical properties. This mismatch frequently resulted in delamination, stress concentrations, and failure under extreme thermal loads. The need for a new class of materials that could gradually transition between different constituents led to the development of FGMs.

The earliest documented development of FGMs can be traced back to 1984 in Japan [10], during a research program funded by the Japanese Science and Technology Agency (STA) and the Ministry of Education, Culture, Sports, Science and Technology (MEXT). The research focused on thermal barrier coatings for spacecraft and rocket engines. These applications required materials that could withstand thermal gradients in excess of 1000°C across a few millimeters without undergoing mechanical failure. The idea was to design materials with a continuous change in composition from a heat-resistant ceramic on the surface to a tough metal at the core, ensuring both thermal protection and structural integrity. In 1987, Japanese researchers Koizumi and Hirai officially introduced the term "functionally graded material". Their work laid the foundation for the development of theoretical models to describe material gradation and analyze the thermo-mechanical behavior of such structures. Early efforts focused on simple one-dimensional gradation, often governed by power-law distributions of material properties. These studies rapidly expanded into more complex two-dimensional and three-dimensional gradation, leading to a broader understanding of how FGMs could be applied in different engineering contexts.

By the 1990s, research into FGMs had expanded internationally. Advances in powder metallurgy and surface modification techniques enabled experimental production of FGMs with controlled gradients. This decade also saw the application of finite element methods (FEM) and homogenization techniques to model the effective behavior of FGMs in structural components. During this period, a growing number of applications emerged in fields such as thermal barrier coatings for turbines, biomedical implants (such as dental prostheses and bone plates), and wear-resistant components in mechanical systems. In the 2000s and 2010s, the rise of additive manufacturing revolutionized the fabrication of FGMs. Techniques such as laser engineered net shaping (LENS), selective laser melting (SLM), and direct energy deposition (DED) allowed unprecedented control over material composition during layer-by-layer manufacturing. These technologies facilitated the creation of highly complex FGM geometries, enabling broader industrial adoption. Simultaneously, computational models were refined to account for porosity, multi-phase behavior, and nonlinear gradients in material properties.

Today, FGMs represent a mature area of research and a growing field of practical application. They are employed not only in aerospace and energy systems, but also in electronics, biomedical devices, and defense structures. The continued development of smart materials, multi-functional composites, and AI-driven design tools further expands the possibilities for FGMs in future technologies.

Between 1987 and 1989, the Japanese government launched a large-scale research program entitled "Fundamental study on the relaxation of thermal stresses in high temperature materials using raded structures" see Figure 1.7, with a budget exceeding one billion yen [11]. More than thirty organizations including universities, research institutes, and industrial companies participated in this initiative aimed at designing and producing prototypes of functionally graded materials (FGMs). The first experimental samples, approximately 10 mm thick and 30 mm in diameter, demonstrated the ability to withstand temperatures up to 2000 K and thermal gradients as high as 1000 K.

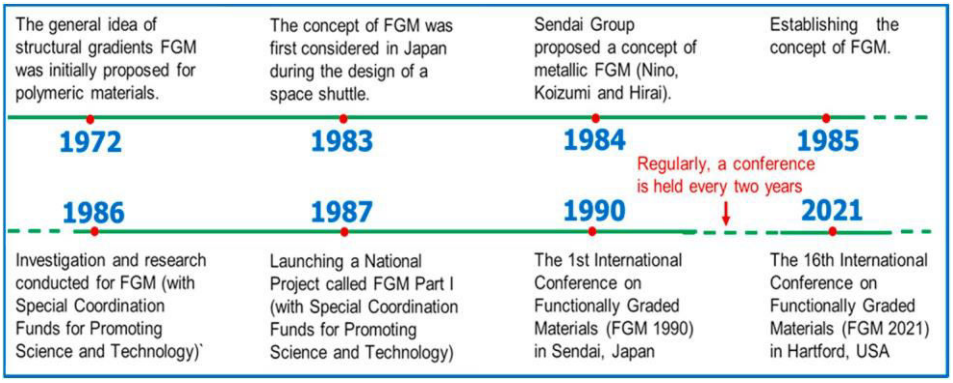

Fig 1. 7 Key historical milestones in the research and development of functionally graded materials (FGMs) [12].

Between 1990 and 1991, research efforts shifted toward the fabrication of larger and more geometrically complex components. Functionally graded materials (FGMs) began to find applications in several emerging industries, including automotive, defense, biomedical engineering, and semiconductors. During this period, theoretical investigations were initiated to assess the mechanical and dynamic performance of FGMs, particularly in rotating structures such as rotors.

It is worth noting that the concept of material gradation is not new; numerous examples exist in nature [13]. Some of the most prominent examples can be found in biological tissues such as bones, teeth, and skin, whose properties vary gradually in terms of hardness and ductility much like the graded characteristics observed in both animal and plant tissues [14]. Figures 1.8 and

1.9 illustrate several natural examples and technical applications that require graded properties. A notable example is dental crowns, which demand high ductility on the inner side to resist fatigue and high hardness on the outer surface to withstand wear [15].

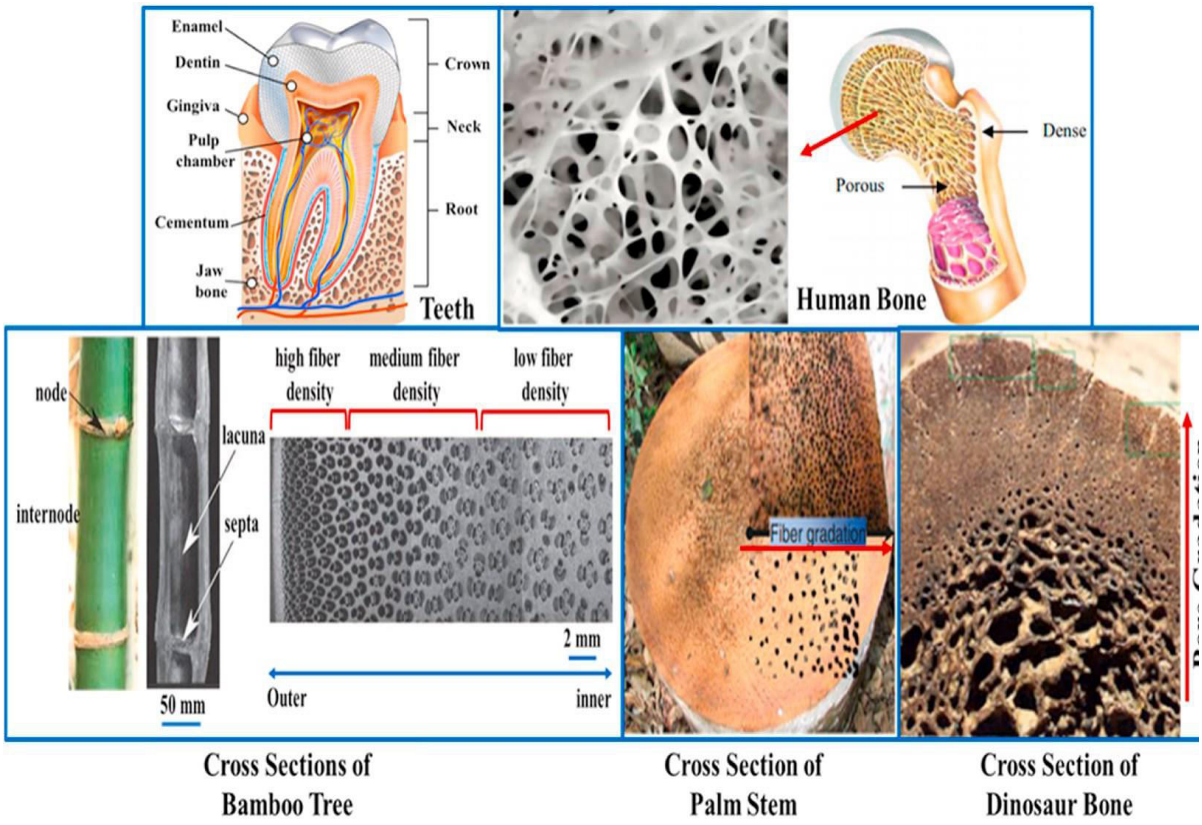

Fig 1. 8 Nature-inspired functionally graded structures [16, 17]

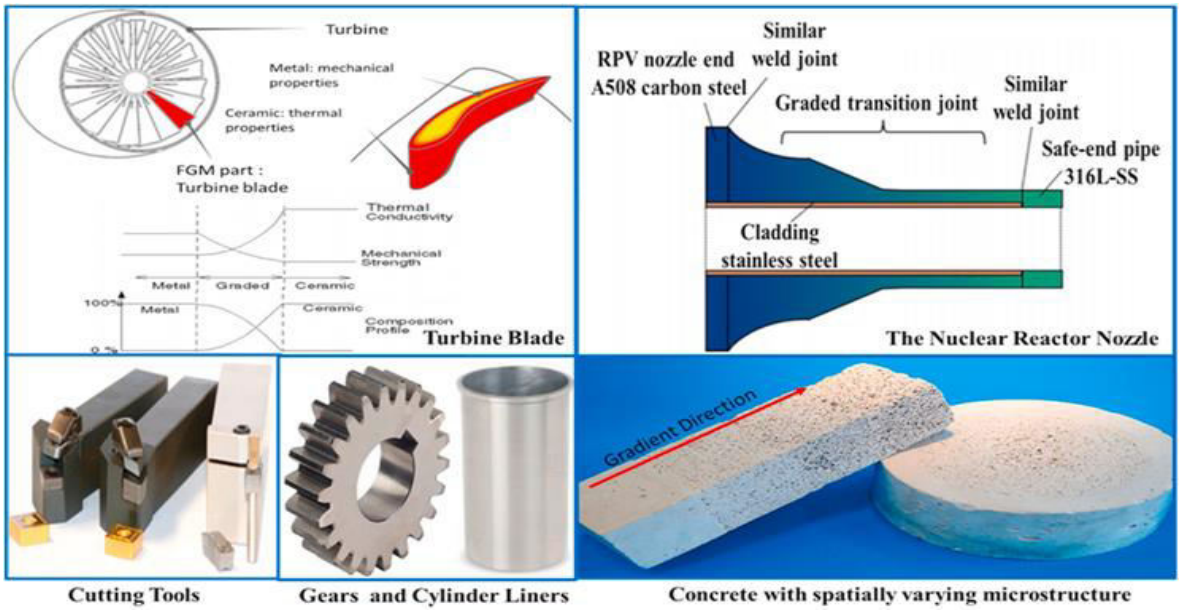

Fig 1. 9 Industrial examples of FGMs designed for property gradation [16, 17]

Figure 1.10 illustrates the contribution of various manufacturing methods to the production of functionally graded materials (FGMs), based on data extracted from the Web of Science system between 1990 and December 2024. Although FGMs first emerged in the mid-1980s, their real expansion began in the 1990s, followed by a continuous increase in scientific publications on the topic see Figure 1.11.

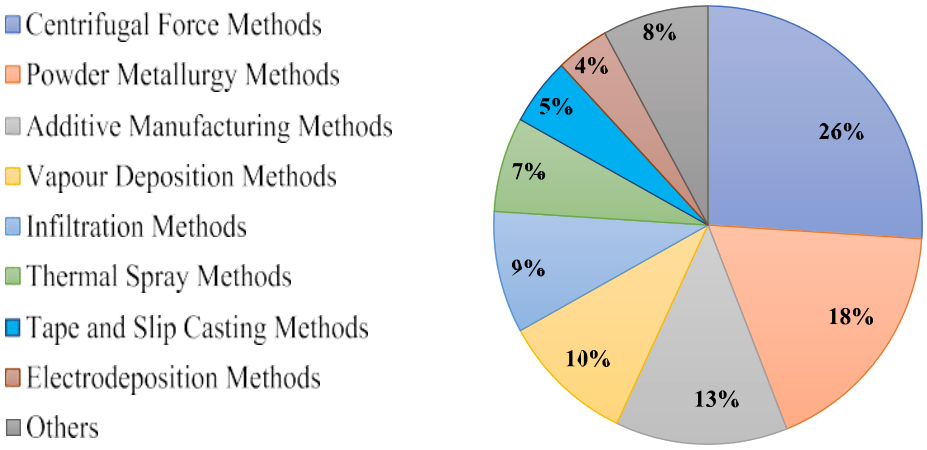

Fig 1. 10 Manufacturing contributions to FGM development from 1990 to December 2024 (Web of Science data) [12]

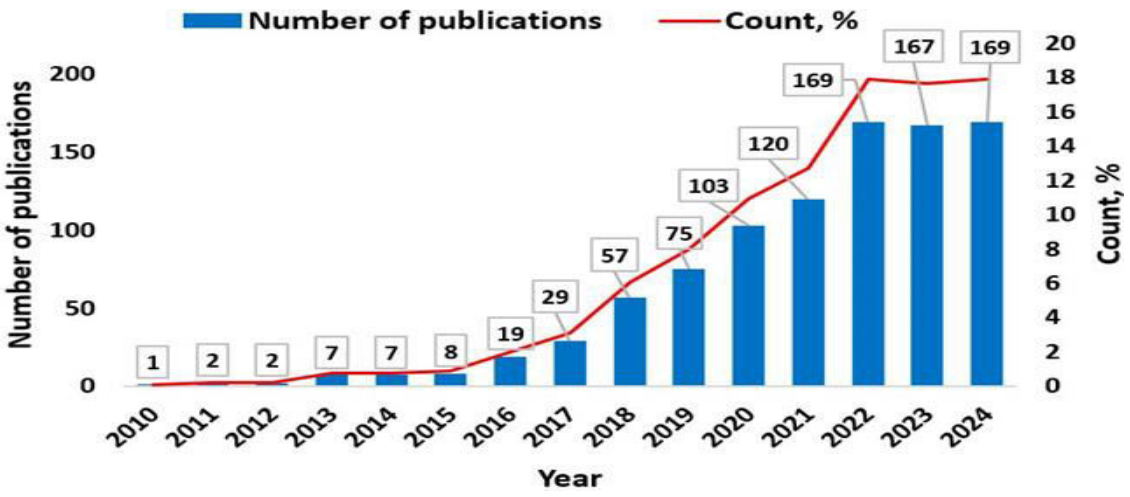

Fig 1. 11 Annual distribution of publications [12]

The temporal progression of published research articles, as illustrated in Figure 1.11, indicates a modest level of activity during the initial period from 2010 to 2015, with annual publications fluctuating between 1 and 8. This limited output suggests that the topic was either in its infancy or had not yet garnered significant interest within the scientific community. A notable shift occurs in 2016, marked by a substantial rise to 19 publications, signaling a growing recognition of the subject's relevance. This upward momentum continues, reaching 29 publications in 2017. The trend accelerates considerably in subsequent years, with 57 articles in 2018 and 75 in 2019. The period from 2020 to 2021 represents the most pronounced phase of growth, with the number of publications increasing sharply from 120 to 169. This peak likely reflects a surge in academic attention and a broader appreciation of the field's significance in addressing emerging challenges. From 2021 to 2024, the publication rate stabilizes at 169 annually, indicating that the domain has entered a mature stage characterized by steady research output rather than exponential expansion.

Several researchers have played a fundamental role in the scientific advancement of the field. M. Koizumi introduced the concept of FGM rotors with a radial distribution of material properties[18]. W. Kim proposed long cutting tools optimized for high-speed machining, based on a model employing Timoshenko beam theory and the Galerkin method [19]. J.N. Reddy significantly contributed to a deeper understanding of FGM plates through the finite element method [20], while M.Y. Chang studied composite rotors equipped with rigid disks and supported by bearings [21]. Other notable works include those of Wang and Zhang on carbon nanotube-reinforced FGMs [22], Boukhalfa and Hadjoui on the free vibrations of rotating composite shafts [23], and Jafari Mehrabadi et al**.** on circular FGM plates [24]. In 2024, during the 17th International Symposium on FGMs (ISFGM2024) held in Portugal, recent innovations highlighted the use of FGMs in advanced fields such as biomedical implants, optical systems, and thermal devices. The integration of additive manufacturing technologies, artificial intelligence, and multi-scale optimization now enables the design of customized components with complex gradients tailored to actual service conditions.An analysis of the most prolific sources in the field reveals that the journal additive manufacturing stands out as the primary outlet, with a total of 80 published articles. This is followed by materials design, which accounts for 38 publications. The international journal of advanced manufacturing technology ranks third, contributing 30 papers to the literature. Other notable sources include materials (26

publications), the journal of materials research and technology *(JMRT)* (24 publications), and both the journal of alloys and compounds and metals, each with 23 articles. Additionally, materials science and engineering A – structural materials: properties, microstructure and processing, Journal of manufacturing processes (20 publications), and materials letters (17 publications) are also among the leading contributors in this research domain. Figure 1.12 presents the geographical distribution of publications, highlighting each country's contribution in both absolute numbers and percentage terms. The United States emerges as the most prolific contributor, with 260 publications, representing approximately 27% of the total output. China follows closely, accounting for 223 publications and a 23% share. Other significant contributors to the literature include India, with 95 publications, as well as England and Germany, with 74 and 73 publications respectively. In contrast, countries such as Turkey, Ireland, and Sweden exhibit more modest levels of research activity in the field, each contributing between 10 and 12 publications.

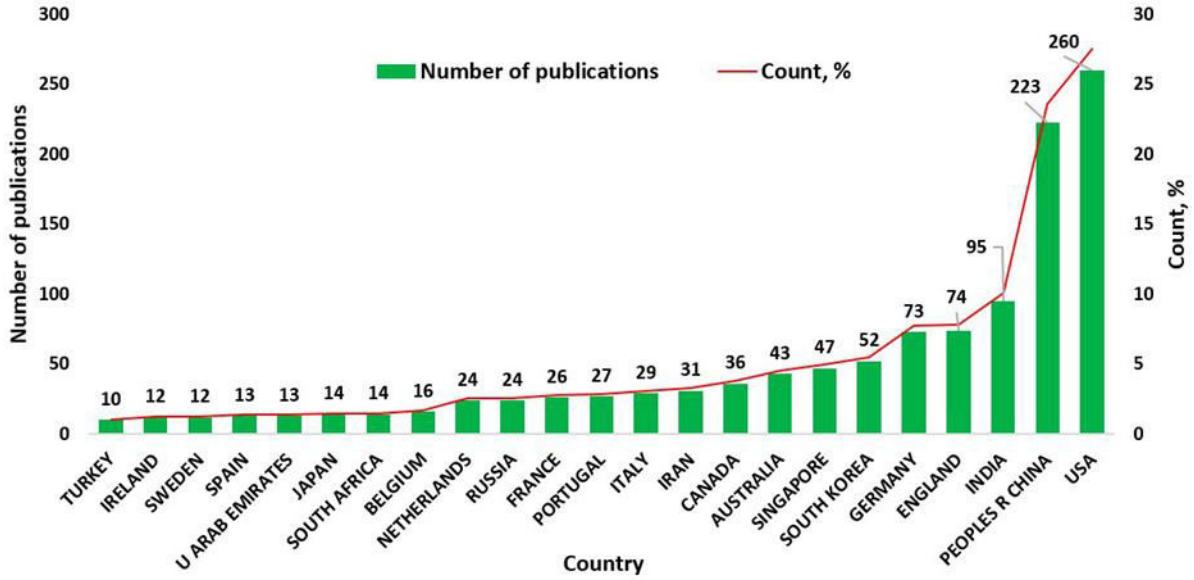

Fig 1. 12 Number of scientific publications by country [12].

These findings underscore the leading roles of the USA and China in research productivity, reflecting their substantial investment and strategic emphasis on advancing the field. In contrast, the contributions from other countries remain moderate to limited, indicating varying levels of engagement and resource allocation.

1.2.3. Concept and Classification of FGM Materials

Functionally Graded Materials can be categorized according to several criteria, such as their dimensional scale, structural configuration, gradient profile, and the nature of the constituent materials, as illustrated in Figures 1.13 and 1.14

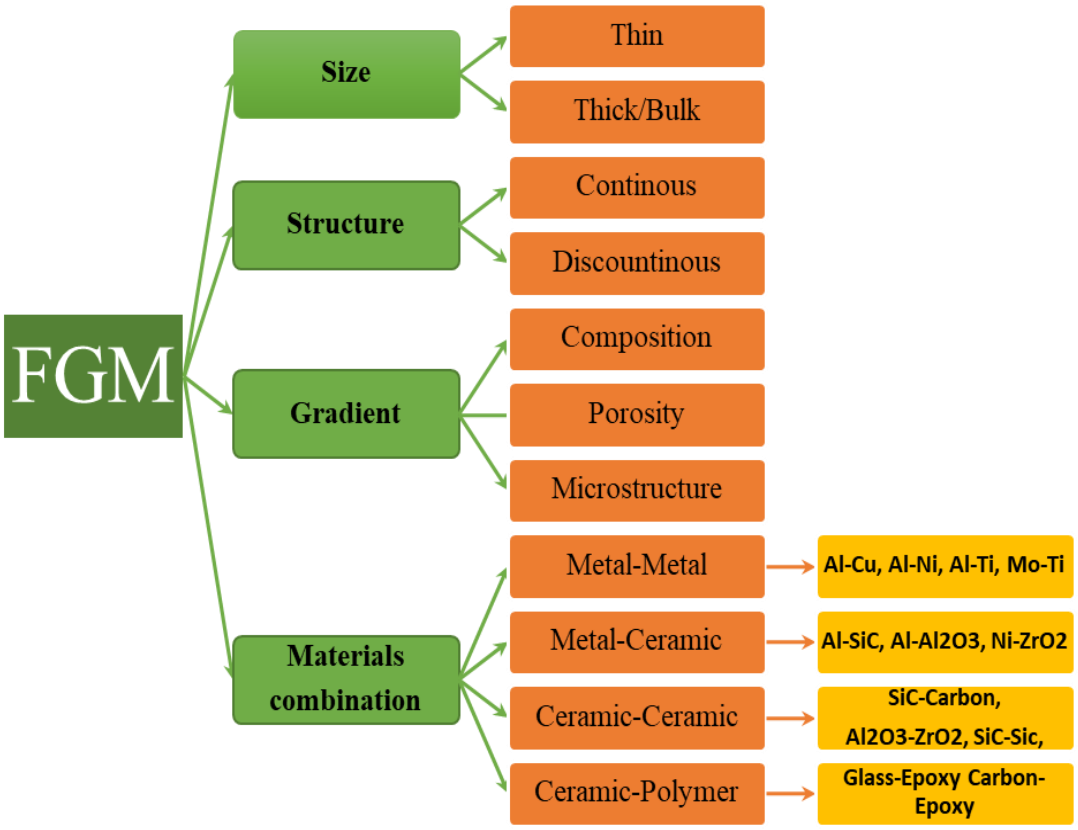

Fig 1. 13 FGMs classification

Fig 1. 14 Comparative schematic of microstructure and properties: FGMs versus traditional composites [10, 25, 26].

The concept of functionally graded materials emerged in the late 1980s thanks to the work of a group of researchers at the National Aerospace Laboratory in Japan. Their objective was to design components capable of withstanding extreme thermal and mechanical stresses, particularly in propulsion systems and the structures of space shuttles, as well as to serve as thermal barriers in nuclear reactor chambers [8, 10].

A material is classified as FGM when it consists of at least two base materials or alloys, distributed continuously or discontinuously throughout the volume of the piece. When it involves a gradual distribution, it is referred to as continuous gradient materials [27]. In this case, the composition and microstructure evolve gradually throughout the piece, thereby allowing for a controlled variation of its properties. This makes it possible to engineer gradients of mechanical, physical, or chemical properties within a single component. The gradual variation of mechanical properties within functionally graded materials (FGM) gives them an optimised structural behaviour, suitable for complex service conditions. These materials are particularly valued in high-tech fields such as aeronautics, aerospace, nuclear, semiconductors, and civil engineering. They are also experiencing notable growth in biomedical applications. In general, FGM are developed from combinations of ceramics and metals, whose respective mechanical properties are compared in Table 1.1

Table 1. 1 Mechanical and physical properties comparison between ceramics and metals [25]

Phase	Position / Function	Main mechanical characteristics
Ceramic	Face exposed to high temperatures	- Excellent thermal resistance - Good resistance to oxidation - Low thermal conductivity
Ceramic - Metal	Transition zone with graded composition	-Elimination of interface discontinuities - Reduction of thermal stresses
Metal	Face exposed to low temperatures	- Good mechanical resistance - High thermal conductivity - High toughness

Figure 1.15 below illustrates the gradual variation in composition, and consequently in microstructure, in a functionally graded material (FGM). This continuous transition generates a gradient that directly influences the overall properties of the material. In some cases, an FGM can be composed of a single base material, but exhibiting distinct microstructures according to the zones, which also allows for differentiated functional behavior [10, 18, 28].

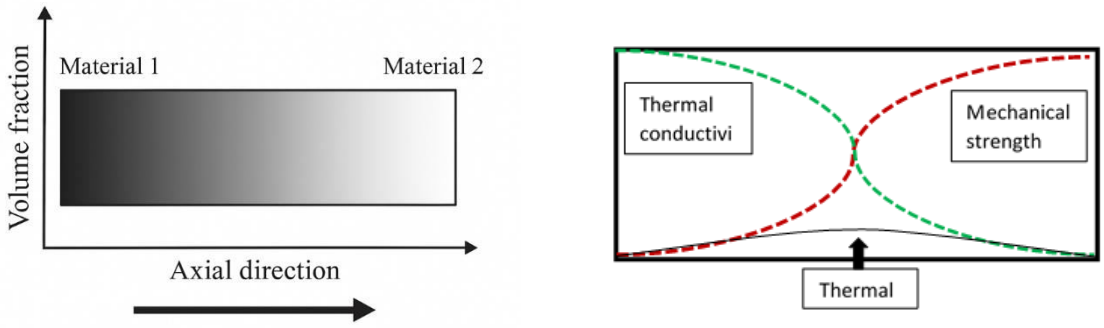

Fig 1. 15 Illustration of axially graded material properties concept [25, 26].

1.2.4. Analytical modelling of FGM layers with axial variation

Functionally Graded Materials (FGM) are advanced composite materials composed of two or more phases with distinct physical properties, continuously distributed in space according to a variable microstructure. When it comes to axial gradation, the distribution of constituents varies along the longitudinal axis of the part, axis x, which allows for local optimisation of mechanical and structural performance in this direction. In this type of configuration, the volume fractions of the base materials gradually evolve along the x-axis, resulting in a continuous variation of the effective mechanical properties, such as the Young's modulus, density, or thermal conductivity, along the axis of the component.

Two main approaches can be used to model this axial variation in FGM layers:

- Approach by discrete slices of quasi-homogeneous layers: The FGM material is divided into a series of segments or slices along the x-axis. Each segment is considered homogeneous, with a constant volume fraction for the base materials. This method allows for a piecewise approximation of the continuous variation of properties (see Figure 1.16.a). It is often used in analytical models or in finite element discretisation.

- Continuous grading approach along the x-axis: In this approach, the volume fraction varies continuously according to a function of the axial coordinate x, see Figure 1.16.b. Several mathematical functions are used in the literature to model this gradation, including:

  - Power-law distribution : $V_m(x) = \left(\frac{x}{L}\right)^n$ (1. 1)

  - Exponential distribution: $V_m(x) = e^{\beta x}$ (1. 2)

  - Sigmoid function, for smoother transitions.

Experimental studies have shown that the exponential and power laws are the most commonly used material gradation models for functionally graded materials (FGMs). This study adopts the power-law gradient assumption. A hollow parabolic shaft made of an axially graded FGM composed of two constituents zirconia (ZrO_2) and aluminum (Al). The effective material properties P(x) along the axial direction of the shaft's cross-section are defined as in Eq.1.3 [29], corresponding to the material distribution along the x-axis.

$$\mathrm{P(x)} = (\mathrm{P_2} - \mathrm{P_1})(\mathrm{x})^{\mathrm{n}} + \mathrm{P_1} \quad (1.\ 3)$$

According to power law distribution, the variations of material properties along the axial direction of circular a hollow non-uniform shaft can be expressed as [29] :

$$\begin{cases} \mathrm{E(x)} = (\mathrm{E_2} - \mathrm{E_1})(\mathrm{x})^{\mathrm{n}} + \mathrm{E_1} \\ \rho(\mathrm{x}) = (\rho_2 - \rho_1)(\mathrm{x})^{\mathrm{n}} + \rho_1 \\ \nu(\mathrm{x}) = (\nu_2 - \nu_1)(\mathrm{x})^{\mathrm{n}} + \nu_1 \end{cases} \quad (1.\ 4)$$

Where n represents the index for material gradient, and P signifies the material characteristics, encompassing variables such as ρ density, E Young's modulus, as well as υ Poisson's ratio. P_1 and P_2 denote their respective values at the shaft's left and right extremist. Figure 1.16 illustrates the change in in density ρ and Young's modulus, respectively, for a shaft with a unit length, under different values of n. It is evident that the proportion of aluminum grows as the value of n approaches infinity. It is advised that the value of n should fall between the range of $1/3 \leq n \leq 3$. Any number outside of this range would lead to a material with an excessively high

proportion of one of its components, namely aluminum. It can be observed that the material exhibits homogeneous behavior when n = 0 or as n→+∞.

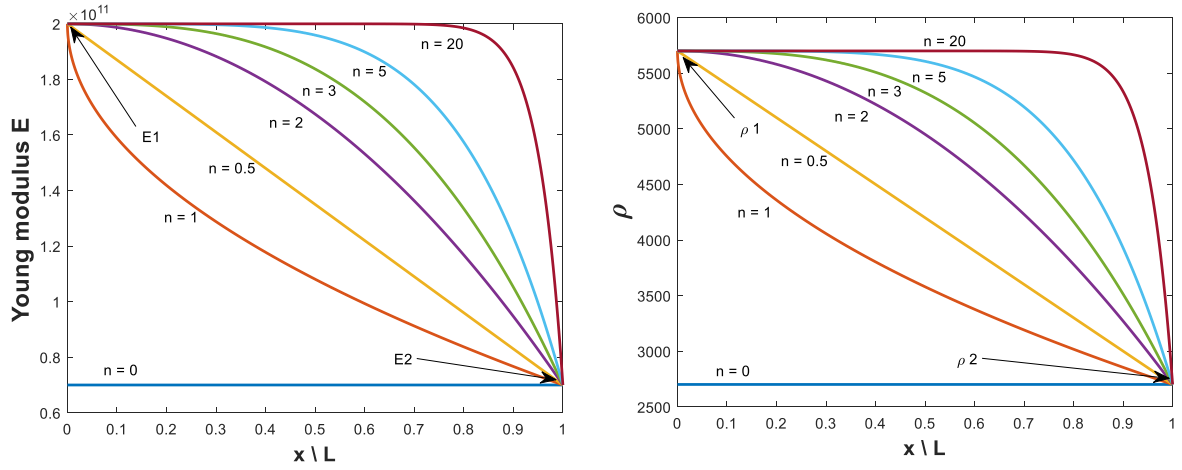

a) **b)**

Fig 1. 16 Axial variation of. a) Young modulus E; b) density ρ

1.2.5. Areas of application of functionally graded materials (FGM)

Functionally graded materials are used in a wide range of technological fields due to their unique ability to combine, within a single component, physical or mechanical properties that are often contradictory. This concept is based on a gradual transition from one material to another, allowing the avoidance of discontinuities and sharp interfaces that are typically responsible for stress concentrations or material failure. FGMs were originally developed in the 1980s as part of Japan's aerospace and space programs. The initial objective was to design components capable of simultaneously providing excellent thermal conductivity on the side exposed to high temperatures (e.g., in contact with hot gases) and good thermal insulation on the opposite side, thereby protecting internal structures. This ability to thermally grade materials while maintaining mechanical strength paved the way for advanced applications in thermal protection systems for engines and turbine coatings.

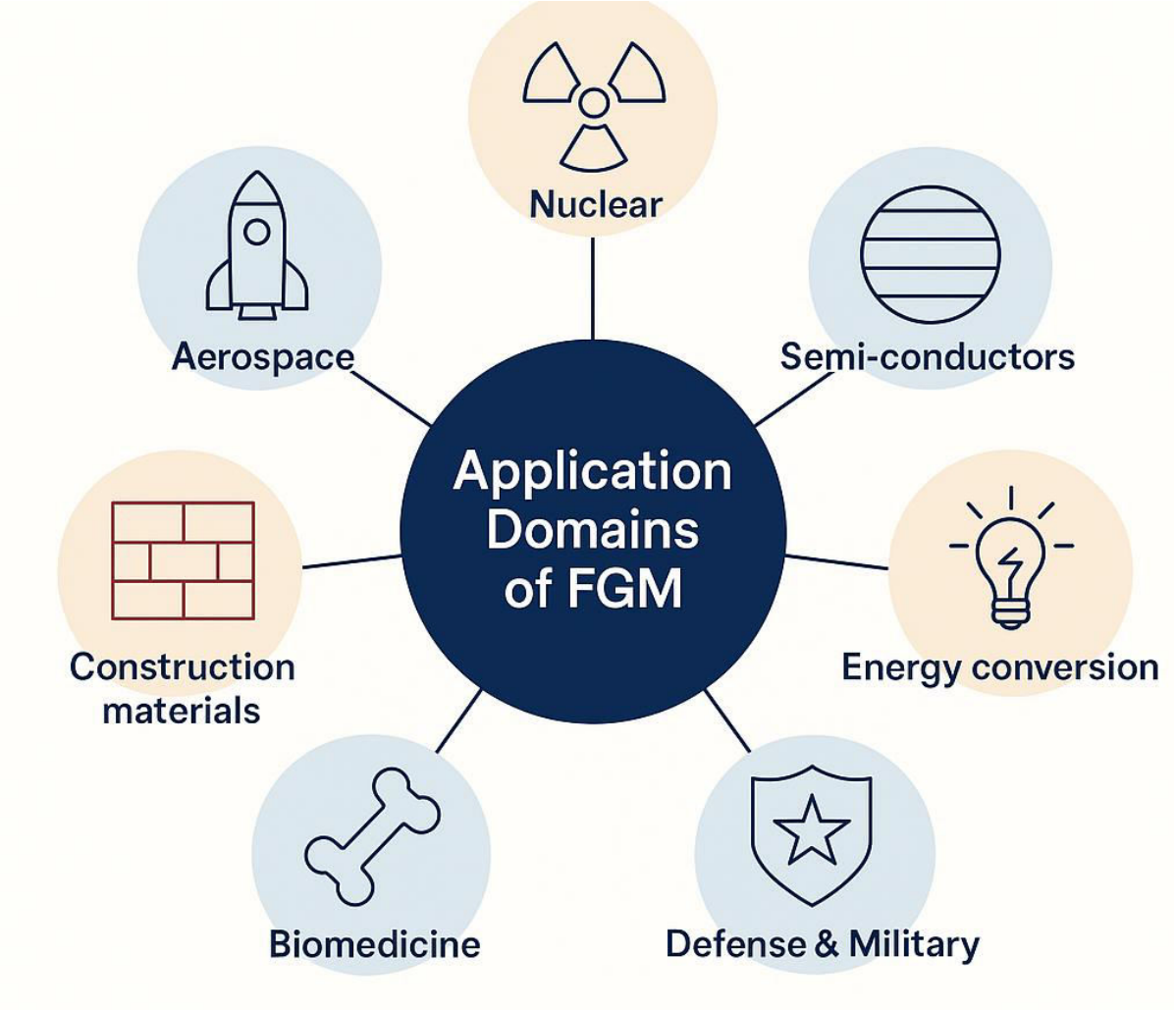

Fig 1. 17 Overview of FGM application domains.

Today, the use of FGMs has expanded significantly into other industrial sectors, including:

- **Aerospace:** Originally developed to reduce thermal stresses in spacecraft, functionally graded materials (FGMs) have since found broad applications in aerospace [26]. They are now used in various components such as rocket engines, gear structures, heat exchangers, and parts exposed to extreme temperatures or wear, including solar panels, turbine coatings, and missile nose cones (see Figure 18 and 19) [30]. For instance, Al_2O_3/Al FG composites, known for their thermal and corrosion resistance, are employed in engine parts and rocket nozzles. To enhance bonding between layers, advanced methods like hot pressing of W/W-Cu composites have been introduced [31]. Additionally, research on FG polymer–ceramic composites has investigated how processing parameters affect their mechanical properties, supporting their use in aerospace applications[32].

Fig 1. 18 Functionally graded material parts used in aerospace [12].

- **Automotive sector:** Many automotive components, including diesel engine pistons, cylinder liners, combustion chambers, racing car brakes, driveshafts, and flywheels, require graded properties to withstand varying thermal, pressure, or mechanical stresses. As a result, FGMs with tailored gradients are well suited for these applications, as illustrated in Figure 19. FGMs are also used in automotive body coatings; however, their high production cost limits their widespread adoption, restricting use primarily to critical parts in vehicles [33]. Kimberly et al. [34] successfully fabricated functionally graded Al_2O_3/Al_2TiO_5 composites via powder metallurgy to investigate the effects of graded structures on microstructure, physical, and thermal properties relevant to automotive applications. Their findings demonstrated enhanced mechanical and thermal performance, particularly for car brake rotors. Similarly, Ram et al. [35] produced FG Al–Mg_2Si composites using centrifugal casting to examine the influence of process parameters on microstructure and mechanical properties for automotive cylinder liners. The study showed that the graded composites exhibited improved properties compared to conventional counterparts, meeting the specific requirements of their intended applications.

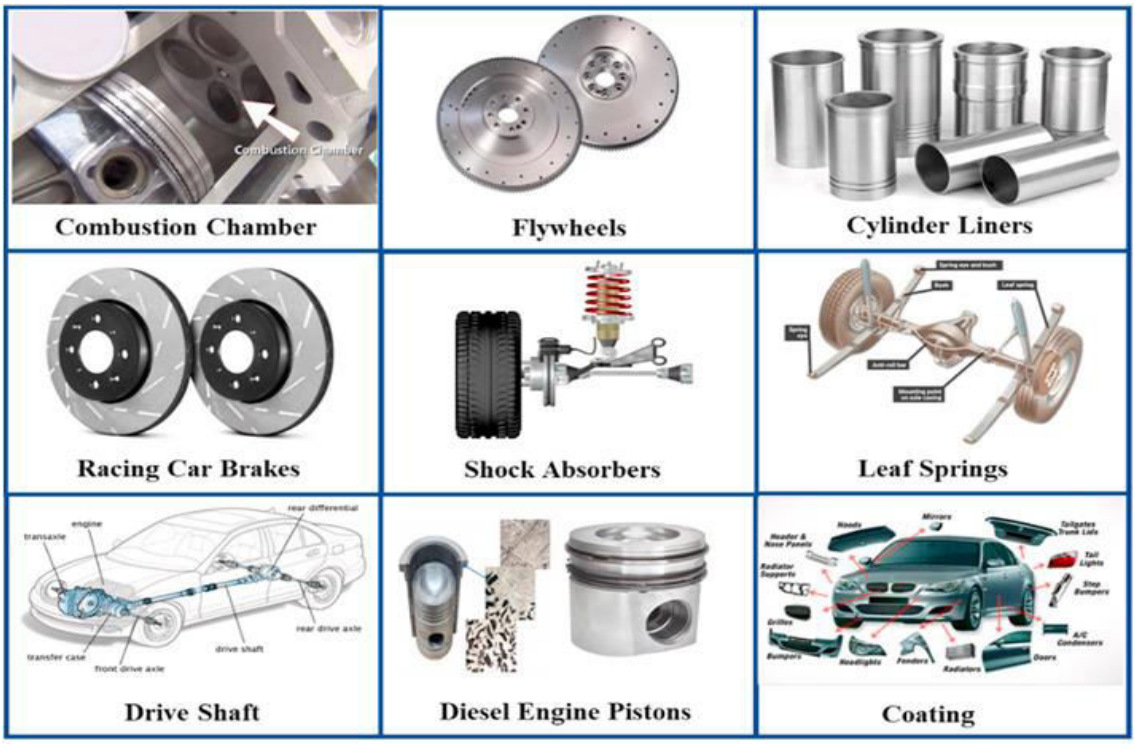

Fig 1. 19 Functionally graded material parts used in the automotive industry [12].

- **Energy sector:** Beyond previously mentioned sectors, functionally graded materials (FGMs) with tailored gradient structures hold significant promise in energy, electronics, and optoelectronic applications. Thermal gradients in FGMs are increasingly utilized in various energy systems to replace the traditional use of single materials operating under extreme temperatures. Examples include thermal power generation, solar energy components, and energy conversion devices such as capacitors, sensors, and electrodes [36, 37]. Additionally, graded materials find applications in batteries, semiconductor devices (including transistors, diodes, and optoelectronics), piezoelectric components, and integrated circuits [38].

- **Nuclear industry:** for structural components exposed to radiation and extreme temperatures, FGMs provide enhanced resistance to damage.
- **Construction materials:** The functional gradation of concrete components enables the internal composition of structural elements to be tailored to meet specific mechanical and thermal performance demands. This is achieved by continuously varying material properties such as porosity, strength, and stiffness along one, two, or even three spatial axes. Such a gradation strategy facilitates mass reduction while also allowing the integration of multiple

functionalities within the same element. In particular, decreasing porosity tends to enhance the mechanical performance of concrete, whereas increasing porosity improves its thermal insulation capacity. Figure 1.20 illustrates the variation in the properties of hardened concrete as a function of gradually increasing porosity [39].

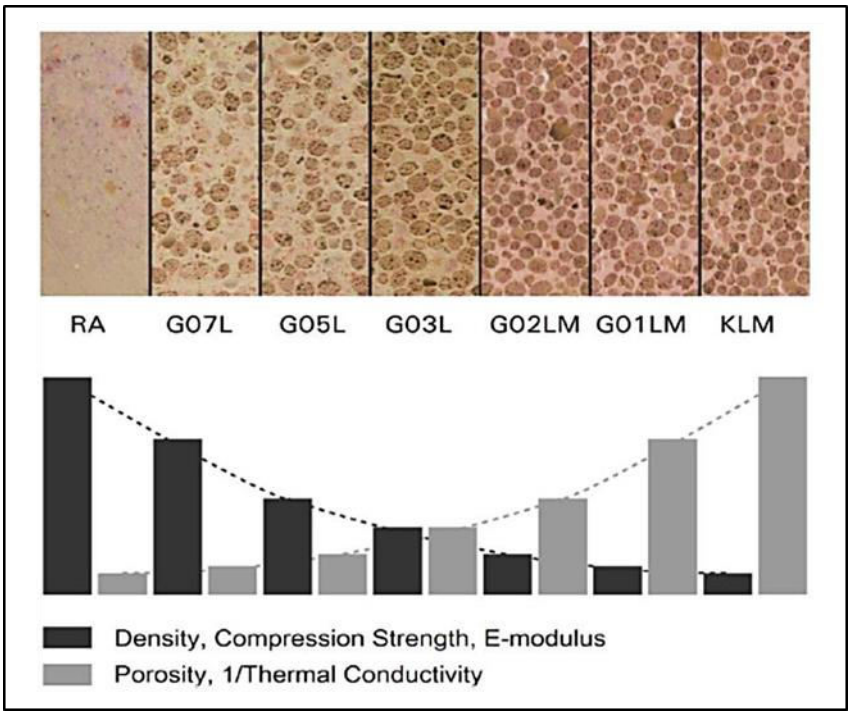

Fig 1. 20 Variation of hardened concrete characteristics with gradual porosity increase [25].

- **Electronic and semiconductor devices:** thanks to the ability to grade electrical or thermal properties at the microscopic scale.
- **Defense Applications:** In the defense sector, there is a growing emphasis on reducing vehicle weight and preventing crack propagation through the use of functionally graded materials (FGMs). These graded structures are employed as penetration-resistant materials for manufacturing armor plates and bulletproof vests, as well as other defensive components such as guide rods and precision rollers. For example, low-weight, high-impact resistant armor has been developed from Al_2O_3–ZrO_2 composites fabricated via powder metallurgy. Researchers conducted simulations to validate their experimental findings, demonstrating that FG Al_2O_3/ZrO_2 composites with graded properties exhibit superior performance compared to conventional composites, making them highly promising for defense applications as shown Figure 1.21.

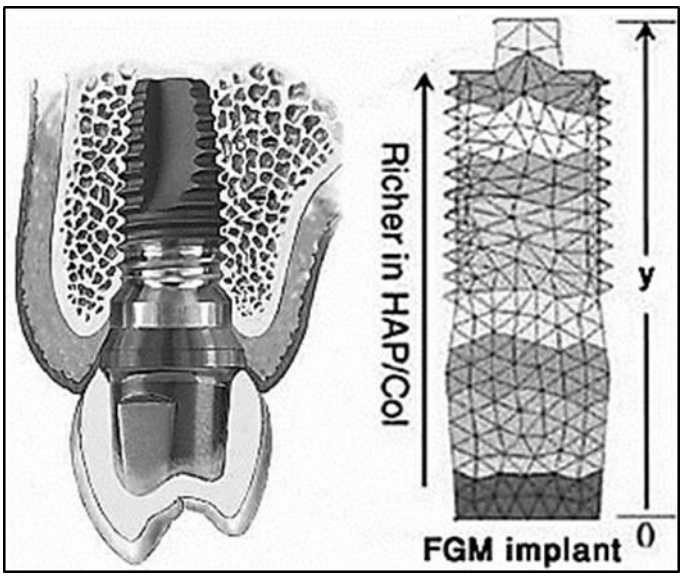

Fig 1. 21 Schematic representation of graded material distribution in an FGM dental implant [40]

- **Biomedical field:** in Functionally graded materials (FGMs) with tailored gradient structures provide enhanced biocompatibility while simultaneously offering improved bonding strength, corrosion resistance, and wear resistance compared to uniform materials. Consequently, FGMs have become widely applied in prosthetic devices and dental components. Recent developments include FG composites such as Ti-HA, Ti–Co, Ti–ZrO_2, HA-ZrO_2, Ti–SiO_2, and TiN-HA, which are used in dental implants and artificial bones to promote biocompatibility, wear resistance, hardness, and bone growth while preventing bone loss [41, 42]. Beyond dental and prosthetic applications, FGMs are also employed in cartilage repair [43]. Thieme et al. [44] fabricated porous FG titanium composites via powder metallurgy to study stress shielding effects on microstructure and mechanical properties relevant to orthopedic implants. Their results showed improved bone compatibility, suggesting suitability as a permanent skeletal replacement. Lee et al. [45] produced FG Al_2O_3–ZrO_2 composites using a fibrous monolithic process, demonstrating enhanced osteoconductivity and mechanical performance. They emphasized that graded structures without bulk defects depend critically on parameters such as porosity, powder size, and volume fraction. Akmal et al. [46] investigated FG 316L-HA composites fabricated via pressureless sintering, focusing on the influence of hydroxyapatite particle size on interfacial bonding and mechanical properties for bioimplant use. Their study revealed that nano-sized HA led to better densification, higher hardness, and stronger interfacial bonding compared to micro-sized HA, highlighting the advantages of nanoscale reinforcement in biomedical FGMs. More recently, Xiao et al. [47] designed and manufactured FG mandibular prostheses using 3D printing combined with metallic coating techniques (SLA and PVD). They created titanium-coated polymer lattices with graded porosity that matched stress distributions in the human mandible. These graded lattices exhibited compressive strain resistance

above 20% and increased compressive strength by 2–3 times, indicating strong potential for prosthetic and biomedical applications.

In summary, FGMs represent a class of advanced materials with extremely broad adaptability, providing effective solutions to the increasing demands of modern engineering in severe and multifunctional environments.

Chapter 2

2. Beam Theory

2.1. Beam Structures

2.1.1. Definition

In the context of mechanical structure modelling, it is essential to characterise the geometry of the elements in order to adopt appropriate formulations. A beam is commonly defined as an element whose length significantly exceeds its two other transverse dimensions, thickness and width. This configuration allows the reduction of the three-dimensional problem to a one-dimensional model, while maintaining sufficient accuracy for many engineering applications.

However, the nature of the mechanical loads applied to these elements necessitates an important terminological and functional distinction:

- When the applied forces are aligned with the longitudinal axis, primarily inducing tensile or compressive stresses, the element is generally referred to as a bar.
- Conversely, when subjected to torsional loads or involved in the transmission of rotational power, the element is rather termed a shaft.

This distinction is far from trivial. It determines the choice of modelling assumptions bending, shear, torsion, instabilities, etc. particularly in dynamic systems where structures are subjected to rotation or vibration. This is especially relevant in modern applications involving non-uniform, hollow or solid shafts made from materials with variable properties, such as functionally graded materials (FGMs).

Therefore, this chapter focuses on presenting both classical and advanced mechanical models that can represent these structures, taking into account their geometric, material, and functional characteristics.

2.1.2. Kinematic assumptions in classical beam

The modelling of the mechanical behaviour of beams is based on kinematic assumptions that simplify the description of deformations while maintaining sufficient accuracy for the majority of applications.
These assumptions directly determine the validity and limitations of the models employed.

a) **Fundamental assumption: plane sections**

Beam Theory

Navier's assumption, originally introduced in the 19th century, forms the common foundation of classical beam theories. It states that any straight section of a beam, initially plane and perpendicular to the neutral axis, remains plane after deformation. This assumption implies a local rigid-body behaviour for each cross-section, neglecting internal deformations within the section.

b) **Euler–Bernoulli theory: model without transverse shear**

The so-called Euler–Bernoulli or Navier–Bernoulli theory refines this assumption. It considers that:

- The straight section remains plane and perpendicular to the beam's neutral axis before and after deformation.
- The effects of transverse shear are neglected.
- This model is particularly suitable for slender beams (high length-to-thickness ratio) subjected to moderate bending loads.

However, this model becomes inaccurate when bending is significant or when the beam is not slender, as it underestimates transverse rotations and deformations.

c) **Timoshenko theory: inclusion of shear deformation**

To extend its applicability, Timoshenko's theory introduces a crucial modification: the cross-section remains plane but is no longer constrained to remain perpendicular to the beam's neutral axis. In other words, it may rotate independently, which allows for the inclusion of:

- Transverse shear effects, which are significant in thick, composite, or functionally graded beams.
- Improved accuracy in dynamic modelling, particularly at high frequencies.

This theory is now widely regarded as a reference in advanced structural modelling, especially for non-homogeneous media, rotating shafts, or vibrating systems.

In the present study, the dynamic behaviour of the rotating shaft is modelled using Timoshenko beam theory, which the geometry of a rotating shaft-rotor with non-uniform thickness composed of axially functionally graded materials FGM is presented in Figure 2.1.

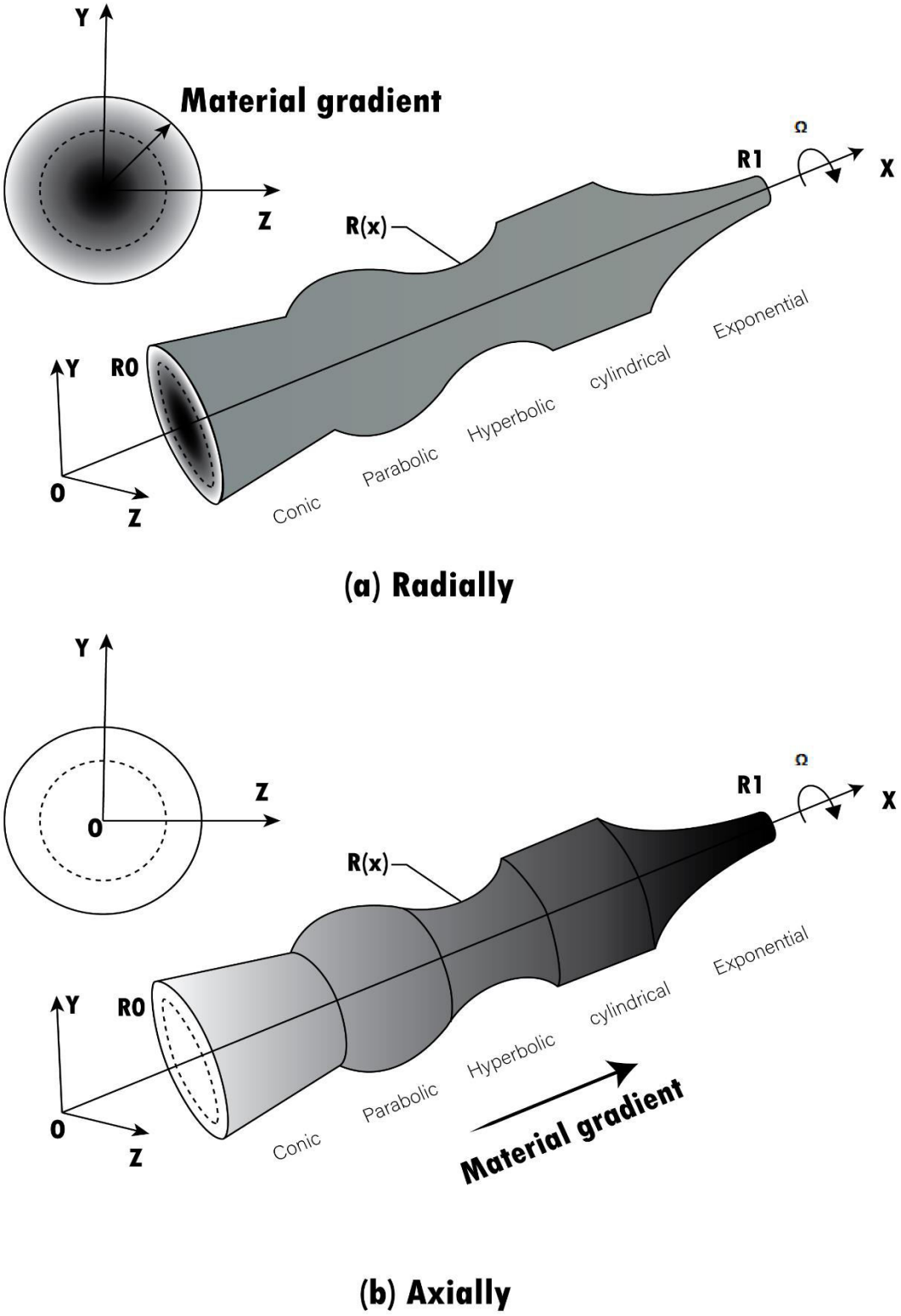

Fig 2. 1 Schematic of a Rotating Hollow Shaft with Axial and Radial Material Gradation.

a) View of spinning shaft, b) Orthogonal view of the cross-section

The radius R(x) of the hollow/solid variable profile is given by:

Shaft with parabolic profile: $$\mathbf{R(x) = \alpha x^2 + R_0} \quad (2.1)$$

Truncated conical shaft: $$\mathbf{R(x) = \alpha x + R_0} \quad (2.2)$$

Shaft with hyperbolic profile: $$\mathbf{R(x) = \frac{1}{a x + \frac{1}{R_0}}} \quad (2.3)$$

Shaft with exponential profile $$\mathbf{R(x) = R_0 e^{\alpha x}} \quad (2.4)$$

Cylindrical shaft: $$\mathbf{R(x) = R_0 = R_1 = R} \quad (2.5)$$

Where:

R_0 is the radius at $x = 0$.

R_1 is the radius at $x = L$.

R_i is the inner radius of the shaft.

a i*s* the radius coefficient.

L is the length of the shaft.

2.2. Kinematic Equations

Timoshenko beam theory, applied to shafts, describes the displacement field of a hollow non-uniform spinning shaft made of axially graded FGMs in the rotating reference frame (x, y, z), as

$$\begin{cases} U(x,y,z,t) = U_0(x,t) + z\beta_x(x,t) - y\beta_y(x,t) \\ V(x,y,z,t) = V_0(x,t) \\ W(x,y,z,t) = W_0(x,t) \end{cases} \quad (2.6)$$

With

$$\begin{cases} U_0(x,t) = U(x,0,0,t) \\ V_0(x,t) = V(x,0,0,t) \\ W_0(x,t) = W(x,0,0,t) \end{cases} \quad (2.7)$$

Here, we have two transverse displacements V, W, and one axial displacement U. The variables V_0 and W_0 correspond to the displacements caused by the bending of the shaft's central axis. Additionally, β_x and β_y represent the rotations of the cross-section around the y-axis and z-axis, respectively.

2.2.1. Deformation-displacement relationship

For small displacements, the deformation–displacement relations are given by [48]:

$$\varepsilon_{ij} = \frac{1}{2}\left(\frac{\partial U_i}{\partial x_j} + \frac{\partial U_j}{\partial x_i}\right) \tag{2. 8}$$

With:

$$(\mathrm{i, j=1,2,3});\ (\mathrm{x_1 = x, x_2 = y, x_3 = z});\ (\mathrm{U_1 = U, U_2 = V, U_3 = W}); \tag{2. 9}$$

The deformation field and displacement field relate as follows [48]:

$$\begin{cases} \varepsilon_{\mathrm{xx}} = \dfrac{\partial \mathrm{U}}{\partial \mathrm{x}} \\ \varepsilon_{\mathrm{yy}} = \dfrac{\partial \mathrm{V}}{\partial \mathrm{y}} \\ \varepsilon_{\mathrm{zz}} = \dfrac{\partial \mathrm{W}}{\partial \mathrm{z}} \\ \varepsilon_{\mathrm{xy}} = 1/2\left[\dfrac{\partial \mathrm{U}}{\partial \mathrm{y}} + \dfrac{\partial \mathrm{V}}{\partial \mathrm{x}}\right] \\ \varepsilon_{\mathrm{xz}} = 1/2\left[\dfrac{\partial \mathrm{U}}{\partial \mathrm{z}} + \dfrac{\partial \mathrm{W}}{\partial \mathrm{x}}\right] \\ \varepsilon_{\mathrm{yz}} = 1/2\left[\dfrac{\partial \mathrm{V}}{\partial \mathrm{z}} + \dfrac{\partial \mathrm{W}}{\partial \mathrm{y}}\right] \end{cases} \tag{2. 10}$$

The deformation field reduced to the displacement field is written:

$$\begin{cases} \varepsilon_{xx} = \dfrac{\partial U_0}{\partial x} + z\dfrac{\partial \beta_x}{\partial x} - y\dfrac{\partial \beta_y}{\partial x} \\ \varepsilon_{yy} = 0 \\ \varepsilon_{zz} = 0 \\ \varepsilon_{xy} = 1/2\left[-\beta_y + \dfrac{\partial V_0}{\partial x}\right] \\ \varepsilon_{yz} = 0 \\ \varepsilon_{xz} = 1/2\left[\beta_x + \dfrac{\partial W_0}{\partial x}\right] \end{cases} \tag{2. 11}$$

We have $\varepsilon_{xy} = \varepsilon_{yx}\ ;\ \varepsilon_{xz} = \varepsilon_{zx}$

The cylindrical coordinate system's strain components (x, r, θ) can be expressed in relation to the displacement variables as follows [48]:

$$\begin{Bmatrix} \varepsilon_{xx} \\ \varepsilon_{\theta\theta} \\ \varepsilon_{rr} \\ \varepsilon_{x\theta} \\ \varepsilon_{r\theta} \\ \varepsilon_{xr} \end{Bmatrix} = \begin{bmatrix} 1 & 0 & 0 & 0 & 0 & 0 \\ 0 & sin^2\,\theta & cos^2\,\theta & 0 & -2\cos\theta\sin\theta & 0 \\ 0 & cos^2\,\theta & sin^2\,\theta & 0 & 2\cos\theta\sin\theta & 0 \\ 0 & 0 & 0 & -\sin\theta & 0 & \cos\theta \\ 0 & -\cos\theta\ \sin\theta & \cos\theta\ \sin\theta & 0 & cos^2\,\theta - sin^2\ \theta & 0 \\ 0 & 0 & 0 & \cos\theta & 0 & \sin\theta \end{bmatrix} \begin{Bmatrix} \varepsilon_{xx} \\ \varepsilon_{yy} \\ \varepsilon_{zz} \\ \varepsilon_{xy} \\ \varepsilon_{yz} \\ \varepsilon_{xz} \end{Bmatrix} \quad (2.\ 12)$$

In its developed form, Equation 2.11 takes the following expression:

$$\begin{cases} \varepsilon_{xx} = \dfrac{\partial U_0}{\partial x} + r\sin(\theta)\dfrac{\partial \beta_x}{\partial x} - r\cos(\theta)\dfrac{\partial \beta_y}{\partial x} \\ \varepsilon_{rr} = \varepsilon_{\theta\theta} = \varepsilon_{r\theta} = 0 \\ \varepsilon_{x\theta} = \dfrac{1}{2}\left[\beta_y\sin(\theta) + \beta_x\cos(\theta) - \sin(\theta)\dfrac{\partial V_0}{\partial x} + \cos(\theta)\dfrac{\partial W_0}{\partial x}\right] \\ \varepsilon_{xr} = \dfrac{1}{2}\left[\beta_x\sin(\theta) - \beta_y\cos(\theta) + cos(\theta)\dfrac{\partial V_0}{\partial x} - \sin(\theta)\dfrac{\partial W_0}{\partial x}\right] \end{cases} \quad (2.\ 13)$$

And we have: $\varepsilon_{xr} = \varepsilon_{rx}$ and $\varepsilon_{x\theta} = \varepsilon_{\theta x}$

Thus, the strain tensor at a point expressed in cylindrical coordinates is given by:

$$[\varepsilon] = \begin{bmatrix} \varepsilon_{xx} & \varepsilon_{xr} & \varepsilon_{x\theta} \\ \varepsilon_{rx} & 0 & 0 \\ \varepsilon_{\theta x} & 0 & 0 \end{bmatrix} \quad (2.\ 14)$$

2.2.2. Stress-strain relationship

The linear elasticity relation can be written in the condensed form:

$$[\sigma] = [Q]\{\varepsilon\} \quad (2.\ 15)$$

The generalized Hooke's law describes the material behavior using the stiffness matrix [Q], which is symmetric by nature. In functionally graded materials, the elastic response is defined by the stiffness coefficients Q_{ij} and the law is written in matrix form to reflect the variation of properties along the material. For a functionally graded shaft, the constitutive relations can be written as in [49].

$$\begin{bmatrix}\sigma_{xx}\\ \sigma_{\theta\theta}\\ \sigma_{rr}\\ \tau_{r\theta}\\ \tau_{xr}\\ \tau_{x\theta}\end{bmatrix}=\begin{bmatrix}Q_{11} & Q_{12} & Q_{13} & 0 & 0 & 0\\ Q_{21} & Q_{22} & Q_{23} & 0 & 0 & 0\\ Q_{31} & Q_{32} & Q_{33} & 0 & 0 & 0\\ 0 & 0 & 0 & Q_{44} & 0 & 0\\ 0 & 0 & 0 & Q_{54} & K_s\,Q_{55} & 0\\ 0 & 0 & 0 & 0 & 0 & K_s\,Q_{66}\end{bmatrix}\begin{Bmatrix}\varepsilon_{xx}\\ \varepsilon_{\theta\theta}\\ \varepsilon_{rr}\\ \gamma_{r\theta}\\ \gamma_{xr}\\ \gamma_{x\theta}\end{Bmatrix} \quad (2.\ 16)$$

Where Q_{ij} (i, j = 1, 6) are the effective elastic constants.

So the constraints expressed in relation (2.16) in simplified form are:

$$\begin{Bmatrix}\sigma_{xx}\\ \tau_{xr}\\ \tau_{x\theta}\end{Bmatrix}=\begin{bmatrix}Q_{11} & 0 & 0\\ 0 & K_s\,Q_{55} & 0\\ 0 & 0 & K_s\,Q_{66}\end{bmatrix}\begin{Bmatrix}\varepsilon_{xx}\\ \gamma_{xr}\\ \gamma_{x\theta}\end{Bmatrix} \quad (2.\ 17)$$

The stress-strain relationships in the cylindrical coordinate system refer to Figure 5.1-b are formulated as follows:

$$\begin{cases}\sigma_{xx} = Q_{11}\varepsilon_{xx}\\ \tau_{x\theta} = \tau_{\theta x} = K_s\,Q_{66}\,\gamma_{x\theta}\\ \tau_{xr} = \tau_{xr} = K_s\,Q_{55}\,\gamma_{xr}\end{cases} \quad (2.\ 18)$$

We have

$$\tau_{xr} = \tau_{rx} \text{ and } \tau_{x\theta} = \tau_{\theta x} \quad (2.\ 19)$$

K_s Represents the factor accounting for transverse shear effects.

The stiffness, constants, expressed in terms of the elastic moduli for axially functionally graded materials (FGMs) can be defined as follows:

$$Q_{11}(x) = \frac{E(x)}{1-\nu(x)^2};\quad Q_{55}(x) = \frac{E(x)}{2\left(1+\nu(x)\right)};\quad Q_{66}(x) = Q_{55}(x) \quad (2.\ 20)$$

2.2.3. Expression of the strain energy of a non-uniform functionally graded rotating shaft

Consider a non-uniform shaft with a material gradient, modeled according to Timoshenko beam theory, which accounts for shear deformation and rotary inertia effects. The strain energy expression of hollow non-uniform profile with axially FGM is presented as follows [49]

$$E_d = 1/2 \int_V \{\sigma_{ij}\}^T \{\varepsilon_{ij}\} dV \tag{2. 21}$$

Replacing (2.14) and (2.18) in (2.20) we find:

$$E_d = \frac{1}{2} \int_V (\sigma_{xx}\varepsilon_{xx} + 2\tau_{xr}\varepsilon_{xr} + 2\tau_{\theta x}\varepsilon_{x\theta})\, dV \tag{2. 22}$$

The expression (2.21) can be rewritten as:

$$\mathrm{E_d} = 1/2 \int_0^{\mathrm{L}} \int_0^{2\pi} \int_{\mathrm{R_i}}^{\mathrm{R(x)}} \begin{bmatrix} \mathrm{Q_{11}}\ \varepsilon_{\mathrm{XX}} \\ \mathrm{K_s}\ \mathrm{Q_{55}}\ \gamma_{\mathrm{xr}} \\ \mathrm{K_s}\ \mathrm{Q_{66}}\ \gamma_{\mathrm{x\theta}} \end{bmatrix}^{\mathrm{T}} \begin{bmatrix} \dfrac{\partial U_0}{\partial x} + \mathrm{r}\sin\theta \dfrac{\partial \beta_x}{\partial x} - \mathrm{r}\cos\theta \dfrac{\partial \beta_y}{\partial x} \\ \beta_y \sin\theta + \beta_x \cos\theta - \sin\theta \dfrac{\partial \mathrm{V_0}}{\partial x} + \cos\theta \dfrac{\partial \mathrm{w_0}}{\partial x} \\ \beta_x \sin\theta - \beta_y \cos\theta - \sin\theta \dfrac{\partial \mathrm{W_0}}{\partial x} + \cos\theta \dfrac{\partial \mathrm{V_0}}{\partial x} \end{bmatrix} \mathrm{r}\, \mathrm{dr}\, \mathrm{d}\theta\, \mathrm{dx} \tag{2. 23}$$

The explicit form of equation (2.23) is expressed as follows:

$$\begin{aligned} \mathrm{E_d} = {} & \frac{1}{2} \int_{\mathrm{R_i}}^{\mathrm{R(x)}} \mathrm{A_{00}(x)} \left(\frac{\partial U_0}{\partial x}\right)^2 \mathrm{dx} + \frac{1}{2} \int_{\mathrm{R_i}}^{\mathrm{R(x)}} \mathrm{A_{11}(x)} \left(\frac{\partial \beta_x}{\partial x}\right)^2 \mathrm{dx} + \frac{1}{2} \int_{\mathrm{R_i}}^{\mathrm{R(x)}} \mathrm{A_{11}(x)} \left(\frac{\partial \beta_y}{\partial x}\right)^2 \mathrm{dx} \\ & + \frac{1}{2} \mathrm{K_s} \left[\int_{\mathrm{R_i}}^{\mathrm{R(x)}} \left(\mathrm{A_{55}(x)} + \mathrm{A_{66}(x)}\right) \left(\frac{\partial \mathrm{V_0}}{\partial x}\right)^2 \mathrm{dx} \right. \\ & + \int_{\mathrm{R_i}}^{\mathrm{R(x)}} \left(\mathrm{A_{55}(x)} + \mathrm{A_{66}(x)}\right) \left(\frac{\partial \mathrm{W_0}}{\partial x}\right)^2 \mathrm{dx} + \int_{\mathrm{R_i}}^{\mathrm{R(x)}} \left(\mathrm{A_{55}(x)} + \mathrm{A_{66}(x)}\right) \beta_x^2\, \mathrm{dx} \\ & + \int_{\mathrm{R_i}}^{\mathrm{R(x)}} \left(\mathrm{A_{55}(x)} + \mathrm{A_{66}(x)}\right) \beta_y^2\, \mathrm{dx} \\ & + 2 \int_{\mathrm{R_i}}^{\mathrm{R(x)}} \left(\mathrm{A_{55}(x)} + \mathrm{A_{66}(x)}\right) \beta_x \frac{\partial \mathrm{W_0}}{\partial x}\, \mathrm{dx} \\ & \left. - 2 \int_{\mathrm{R_i}}^{\mathrm{R(x)}} \left(\mathrm{A_{55}(x)} + \mathrm{A_{66}(x)}\right) \beta_y \frac{\partial \mathrm{V_0}}{\partial x}\, \mathrm{dx} \right] \end{aligned} \tag{2. 24}$$

With:

$$\mathrm{A_{00}(x)} = \pi \int_{\mathrm{R_i}}^{\mathrm{R(x)}} \mathrm{Q_{11}\,(x) r^3 dr};\ \mathrm{A_{11}(x)} = \pi \int_{\mathrm{R_i}}^{\mathrm{R(x)}} \mathrm{Q_{11}\,(x) r^3 dr}; \tag{2. 25}$$

$$A_{55}(x) = \pi \int_{R_i}^{R(x)} Q_{55}(x)\, r\, dr\,; \quad A_{66}(x) = A_{55}(x)$$

2.2.4. Expression of the kinetic energy of a non-uniform functionally graded rotating shaft

Figure 2.2 illustrates the motion of an arbitrary point **S** on the cross-section of a rotating flexible shaft, modeled here as a single beam element. The displacement of point **S** results from a combination of bending deformation, reflecting the mechanical response of the FGM rotating shaft.

The coordinate system (x, y, z) corresponds to a fixed inertial frame, whereas (x', y', z'), refers to a rotating coordinate system attached to both the shaft and its cross-section.

Prior to deformation, the geometric center Gc of the cross-section coincides with the origin point O.

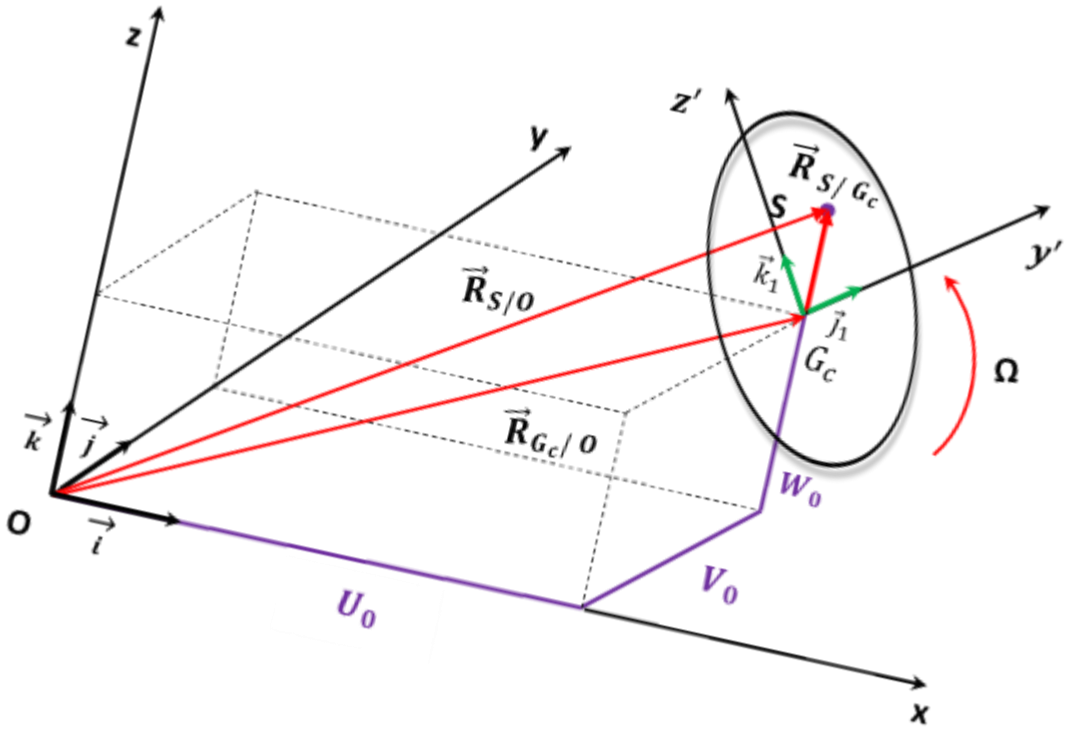

Fig 2. 2 Motion of an arbitrary point S located on the cross-section of the rotating shaft.

(O, x, y, z) : Fixed reference point

(Gc, x′, y′, z′) : Moving reference frame attached to the rotating shaft.

$\boldsymbol{\Omega}$	: Angular velocity of the rotating shaft.
$\vec{\boldsymbol{R}}_{\boldsymbol{S/O}}$	: Displacement vector of point **S** in the rotating shaft.
$\vec{\boldsymbol{R}}_{\boldsymbol{S/Gc}}$	: Displacement vector of point **S** in the moving reference frame.
$\vec{\mathbf{R}}_{\mathbf{GS/O}}$	: Displacement vector of the centroid Gc in the moving reference frame.

2.2.5. Position and velocity of a point on the shaft

The position vector$\vec{R}_{S/O}$ is given by:

$$\vec{\mathrm{R}}_{\mathrm{S/O}} = \vec{\mathrm{R}}_{\mathrm{GS/O}} + \vec{\mathrm{R}}_{\mathrm{S/Gc}} = \left(U_0\vec{\imath} + V_0\vec{\jmath} + W_0\vec{k}\right) + \left(\mathrm{y}_1\vec{\mathrm{j}}_1 + z_1\vec{\mathrm{k}}_1\right) \tag{2. 26}$$

It can be expressed in terms of the cross-section rotations shown in Figure 2.3, which represent the Euler angles of the section, listed respectively as follows.

$$\left(\beta_x, \beta_y, \emptyset\right) \text{With } \emptyset = \Omega\, t \tag{2. 27}$$

$$\begin{aligned}\vec{\mathrm{R}}_{\mathrm{S/O}} = {} & \left(\mathrm{U}_0 + \mathrm{y}_1\beta_\mathrm{y}\cos(\emptyset) + \mathrm{y}_1\beta_\mathrm{x}\cos(\emptyset) + \mathrm{z}_1\beta_\mathrm{y}\sin(\emptyset) + \mathrm{z}_1\beta_\mathrm{x}\cos(\emptyset)\right)\vec{\mathrm{i}} \\ & + \left(\mathrm{V}_0 + \mathrm{y}_1\cos(\emptyset) + \mathrm{y}_1\beta_\mathrm{x}\beta_\mathrm{y}\sin(\emptyset) + \mathrm{z}_1\sin(\emptyset + \mathrm{z}_1\beta_\mathrm{x}\beta_\mathrm{y}\cos(\emptyset)\right)\vec{\mathrm{j}} \\ & + \left(\mathrm{W}_0 + \mathrm{y}_1\sin(\emptyset) + \mathrm{z}_1\cos(\emptyset)\right)\vec{\mathrm{k}}\end{aligned} \tag{2. 28}$$

$$\frac{d\vec{R}_{S/O}}{dt} = \dot{\vec{R}}_{S/O} \tag{2. 29}$$

The velocity vector is:

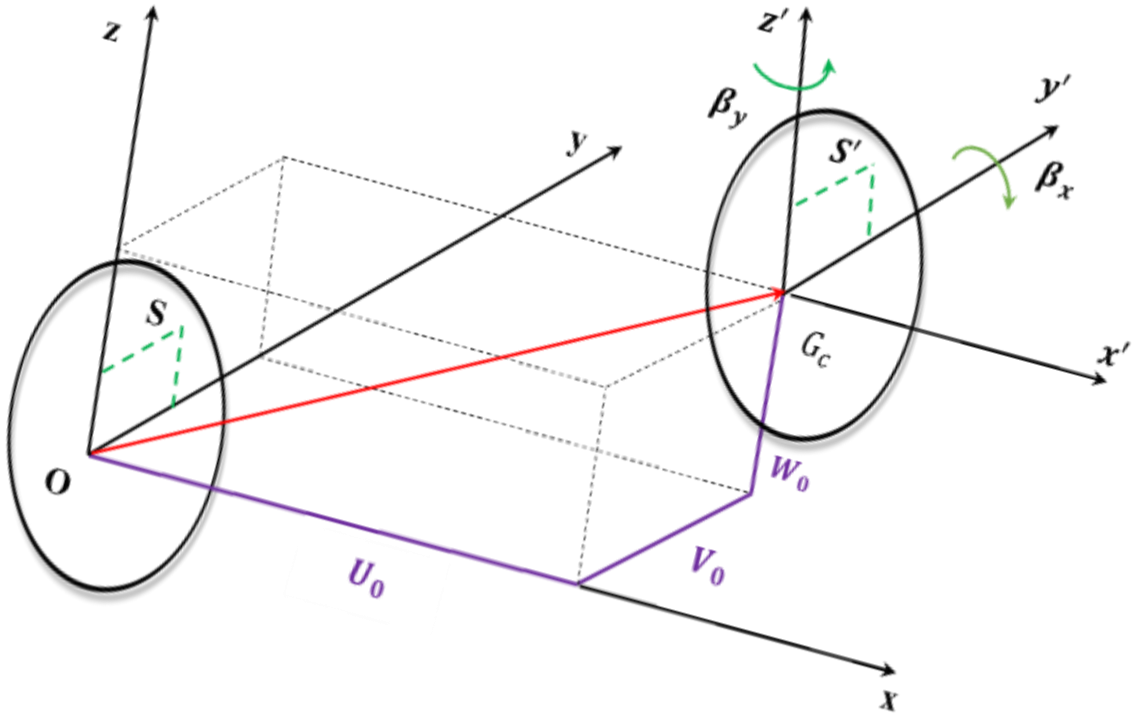

Fig 2. 3 Displacement of the rotating shaft's cross-section.

The kinetic energy of the shaft is given by the following equation:

$$E_c = 1/2 \int_V \rho \, (\dot{\vec{R}}_{S/O} . \dot{\vec{R}}_{S/O}) \, dV \tag{2. 30}$$

The kinetic energy associated with the rotation of the functionally graded material shaft, as presented by [49], can be expressed as:

$$E_c = \frac{1}{2}\int_0^L \Big[I_m(x)\left(\dot{U}_0^2 + V_0^2 + \dot{W}_0^2\right) + I_d(x)\left(\dot{\beta}_x^2 + \dot{\beta}_y^2\right) - 2\Omega I_p(x)\beta_x\dot{\beta}_y + \Omega^2 I_p(x) + \Omega^2 I_d(x)\left(\beta_x^2+\beta_y^2\right)\Big] dx \tag{2. 31}$$

Where $I_d(x)$ denotes the diametral mass moment of inertia, while $I_m(x)$ and $I_p(x)$ represent the mass moment and the polar moment of inertia, respectively. Ω is the constant rotational speed of the shaft, and L denotes its length.

The first term in Equation (2.31) corresponds to the classical expression of the kinetic energy associated with bending in beam theory. The second term accounts for the rotatory inertia, as

introduced in the Timoshenko beam model. The third term represents the gyroscopic effect. The fourth term is constant and has no influence on the equations of motion. The final term, being significantly smaller than the fourth, is neglected in the subsequent analysis.

$$I_p\,(x) = 2\pi \int_{R_i}^{R(x)} \rho\,(x) r^3 dr;\; I_d\,(\xi) = \pi \int_{R_i}^{R(x)} \rho\,(x) r^3 dr\;;\; I_m(\xi) = 2\pi \int_{R_i}^{R(x)} \rho\,(x) r dr \qquad (2.\,32)$$

2.2.6. Equations of motion for a non-uniform functionally graded shaft

The application of Timoshenko's beam theory combined with the Lagrange principle allows the derivation of the elementary stiffness, mass, and gyroscopic matrices, which yields the following Lagrange equation:

$$\frac{d}{dt}\left(\frac{\partial L}{\partial \dot{q}_i}\right) - \frac{\partial L}{\partial q_i} = 0 \qquad (2.\,33)$$

Where the Lagrangian L is defined as:

$$L = E_c - E_d \qquad (2.\,34)$$

Where E_c denotes the kinetic energy of the system and E_d represents the strain energy, which corresponds to the potential energy stored in the structure. The variable q_i refers to the *i-th* generalized coordinate, while $\dot{q}_i$ denotes the associated generalized velocity.

As a result, Equation (2.34) takes the following form:

$$[M]\{\ddot{q}\} + [G]\{\dot{q}\} + [K]\{q\} = \{0\} \qquad (2.\,35)$$

In this expression, $[M]$ denotes the mass matrix, $[K]$ represents the stiffness matrix, and $[G]$ corresponds to the gyroscopic matrix.

The determination of all matrices involved in system (2.35) will be carried out using the *p*-version of the finite element method.

Chapter 3

3. Numerical Modeling Based on the *p*-Version of the Finite Element Method

3.1. Introduction

The finite element method (FEM) is a widely used numerical technique for solving boundary value problems in engineering and applied sciences. It provides a versatile framework for modeling complex geometries, heterogeneous materials, and diverse boundary and loading conditions. Within the FEM, two main refinement strategies exist: the *h*-version and the *p*-version. While the *h*-version improves accuracy by subdividing the domain into smaller elements (mesh refinement), the *p*-version enhances the solution by increasing the polynomial degree of the shape functions used within each element, without altering the mesh density. The *p*-version of the finite element method has gained increasing attention due to its exponential convergence properties in problems with smooth solutions. It is particularly effective in problems involving material or geometric non-uniformities, where gradients of displacement or stress are significant but continuous. In the case of functionally graded materials (FGMs), where properties such as Young's modulus, density, and Poisson's ratio vary continuously along spatial directions, the *p*-version allows for highly accurate modeling with fewer degrees of freedom compared to the *h*-version.

In the context of rotating shafts made of functionally graded materials and exhibiting non-uniform geometry (e.g., conical or tapered profiles), traditional low-order FEM may require extremely fine meshing to capture the dynamic behavior with sufficient precision. This not only increases computational cost but may also lead to numerical instabilities or poor convergence. The *p*-version offers a powerful alternative, enabling high-order polynomial approximations of displacement fields, which are especially beneficial for problems governed by smooth variations in geometry and material properties. This chapter focuses on the development of a numerical model using the *p*-version of the finite element method to investigate the dynamic behavior of a non-uniform functionally graded shaft. The modeling is based on the Timoshenko beam theory, which incorporates both shear deformation and rotatory inertia making it suitable for thick and moderately slender shafts subjected to high-speed rotation. The dynamic formulation is carried out using Lagrange's equations, where the kinetic and strain energies are expressed in terms of generalized coordinates.

The approach involves computing the element-level mass, stiffness, and gyroscopic matrices, which are then assembled into the global system of equations. Each finite element is defined using hierarchical shape functions of variable polynomial degree, enabling flexible control over the approximation order without remeshing. This high-order formulation ensures accurate capture of displacement, velocity, and acceleration fields, as well as gyroscopic and inertial coupling effects that are critical in rotating FGM structures. The use of this method helps to overcome continuity issues along interfaces and effectively handles singularity problems. To enhance the accuracy of the solution, one can either increase the order of the hierarchical mode (p) or refine the mesh. In the hierarchical finite element method, several types of shape functions are employed. Among them are: polynomial functions, trigonometric functions, and combined polynomial–trigonometric functions.

3.1.1. Modeling of the rotating shaft using 3D hierarchical beam elements with trigonometric shape functions

In this study, a hierarchical finite element method employing trigonometric shape functions is adopted and combined with the classical finite element approach. The rotating shaft is modeled using 3D hierarchical beam elements. Each element, as illustrated in Figure 3.1, consists of two nodes, labeled 1 and 2. For stepped shafts, multiple elements can be assembled to represent the variation in geometry along the axis.

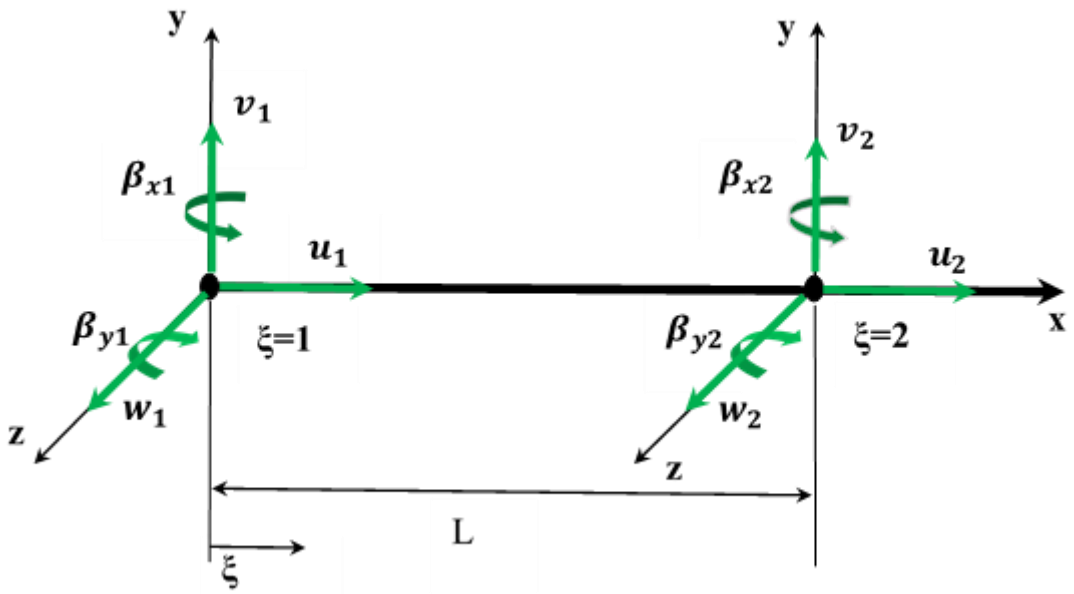

Fig 3. 1 Beam element 3D characterized by two nodes.

The relationship between the physical coordinate x and the non-dimensional coordinate ξ is defined as follows:

$$\xi = \frac{x}{L}\text{; With } (0 \leqslant \xi \leqslant 1) \tag{3. 1}$$

The shape function group corresponding to the translational degrees of freedom U_0, V_0, W_0 and the rotational degrees of freedom β_x and β_y is expressed as:

$$[\mathfrak{f}_1 \mathfrak{f}_2 \dots \dots \mathfrak{f}_{i+2}] \tag{3. 2}$$

Where

$$\left\{ \begin{array}{c} \mathfrak{f}_1 = 1 - \xi \\ \mathfrak{f}_2 = \xi \\ \mathfrak{f}_{i+2} = sin(\delta_i . \xi) \\ \delta_i = i\pi;\ \ i = 1,2,3,.. \end{array} \right\} \tag{3. 3}$$

The nodal displacements within the element are represented by the finite element shape functions $\mathfrak{f}_1$ and $\mathfrak{f}_2$, which govern the behavior at the element boundaries. In contrast, the trigonometric functions $\mathfrak{f}_{(i+2)}$ contribute solely to the internal shear field and do not influence the nodal degrees of freedom directly. One of the key advantages of using trigonometric shape functions lies in their numerical stability, especially in dynamic simulations.

In this study, the rotating shaft is modeled using a single hierarchical finite element enriched with *p*-type functions. This *p*-version approach allows for greater flexibility and accuracy in the formulation of the dynamic behavior. By employing the Euler–Lagrange equations along the longitudinal axis, the equations of motion for free rotational vibration of the spinning functionally graded material (FGM) shaft are derived efficiently. The combination of hierarchical modeling and high-order trigonometric enrichment ensures a robust and stable numerical framework for capturing the complex mechanical behavior of axially graded rotating structures.

The vector of generalized displacements, which contains all the nodal degrees of freedom relevant to the element, can be expressed as:

$$\{q\} = \left\{ U_0, V_0, W_0, \beta_x, \beta_y \right\}^T \tag{3. 4}$$

With

$$\{q\} = \begin{Bmatrix} \{q_u\} \\ \{q_v\} \\ \{q_w\} \\ \{q_{\beta_x}\} \\ \{q_{\beta_y}\} \end{Bmatrix} = \begin{Bmatrix} \{x_1, x_2, x_2, \dots\dots, x_{Pu}\}^T e^{j\omega t} \\ \{y_1, y_2, y_2, \dots\dots, y_{Pv}\}^T e^{j\omega t} \\ \{z_1, z_2, z_3, \dots\dots, z_{Pw}\}^T e^{j\omega t} \\ \{\beta_{x_1}, \beta_{x_2}, \beta_{x_3}, \dots\dots, \beta_{x_{P\beta_x}}\}^T e^{j\omega t} \\ \{\beta_{y_1}, \beta_{y_2}, \beta_{y_3}, \dots\dots, \beta_{y_{P\beta_y}}\}^T e^{j\omega t} \end{Bmatrix} \quad (3.5)$$

The displacement field at an arbitrary point along the beam can be expressed as:

$$\begin{cases} U_0 = [N_U]\{q_U\} = \sum_{m=1}^{PU} x_m(t) f_m(\xi) \\ V_0 = [N_V]\{q_V\} = \sum_{m=1}^{Pv} y_m(t) f_m(\xi) \\ W_0 = [N_w]\{q_w\} = \sum_{m=1}^{Pw} z_m(t) f_m(\xi) \\ \beta_x = [N_{\beta_x}]\{q_{\beta_x}\} = \sum_{m=1}^{P\beta_x} \beta_{x_m}(t) f_m(\xi) \\ \beta_y = [N_{\beta_y}]\{q_{\beta_y}\} = \sum_{m=1}^{P\beta_y} \beta_{y_m}(t) f_m(\xi) \end{cases} \quad (3.6)$$

Where

U_0 : Number of shape functions in the longitudinal direction x

V_0 : Number of shape functions in the transverse direction y

W_0 : Number of shape functions in the transverse direction z

β_x : Number of shape functions for rotation about the y-axis

β_y : Number of shape functions for rotation about the z-axis

The displacement vector {B} can be defined as follows:

$$\{B\}=[N]\ \{q\}=\begin{Bmatrix} U_0 \\ V_0 \\ W_0 \\ \beta_x \\ \beta_y \end{Bmatrix} = \begin{bmatrix} [N_U] & 0 & 0 & 0 & 0 \\ 0 & [N_V] & 0 & 0 & 0 \\ 0 & 0 & [N_w] & 0 & 0 \\ 0 & 0 & 0 & [N_{\beta_x}] & 0 \\ 0 & 0 & 0 & 0 & [N_{\beta_y}] \end{bmatrix} \begin{Bmatrix} q_U \\ N_V \\ q_w \\ q_{\beta_x} \\ q_{\beta_y} \end{Bmatrix} \tag{3. 7}$$

Where [N] represents the shape function matrix used to interpolate the displacement field within the finite element.

$$\left[N_U, \mathrm{N_V}, N_w, N_{\beta_x}, N_{\beta_y}\right] = \left[\mathrm{f_1}\, \mathrm{f_2} \ldots\ldots \mathrm{f_{Pu}}, \mathrm{f_{Pv}}, \mathrm{f_{Pw}}, \mathrm{f_{P\beta_x}}, \mathrm{f_{P\beta_y}}\right] \tag{3. 8}$$

3.1.2. Determination of the elemental stiffness matrix of the shaft $[\mathbf{K_s^e}]$

Based on equations (2.23) and (2.24), the strain energy can be expressed as follows:

$$\begin{aligned} \mathrm{E_d} = {} & \frac{1}{2}\int_0^{\mathrm{L}} \mathrm{A_{00}(x)}\left(\frac{\partial U_0}{\partial x}\right)^2 \mathrm{dx} + \frac{1}{2}\int_0^{\mathrm{L}} \mathrm{A_{11}(x)}\left(\frac{\partial \beta_x}{\partial \mathrm{x}}\right)^2 \mathrm{dx} + \frac{1}{2}\int_0^{\mathrm{L}} \mathrm{A_{11}(x)}\left(\frac{\partial \beta_y}{\partial \mathrm{x}}\right)^2 \mathrm{dx} \\ & + \frac{1}{2}\mathrm{K_s}\left[\int_0^{\mathrm{L}} \left(\mathrm{A_{55}(x)} + \mathrm{A_{66}(x)}\right)\left(\frac{\partial \mathrm{V_0}}{\partial \mathrm{x}}\right)^2 \mathrm{dx}\right. \\ & + \int_0^{\mathrm{L}} \left(\mathrm{A_{55}(x)} + \mathrm{A_{66}(x)}\right)\left(\frac{\partial \mathrm{W_0}}{\partial \mathrm{x}}\right)^2 \mathrm{dx} + \int_0^{\mathrm{L}} \left(\mathrm{A_{55}(x)} + \mathrm{A_{66}(x)}\right)\beta_{\mathrm{x}}^2\, \mathrm{dx} \\ & + \int_0^{\mathrm{L}} \left(\mathrm{A_{55}(x)} + \mathrm{A_{66}(x)}\right)\beta_{\mathrm{y}}^2\, \mathrm{dx} + 2\int_0^{\mathrm{L}} \left(\mathrm{A_{55}(x)} + \mathrm{A_{66}(x)}\right)\beta_{\mathrm{x}}\frac{\partial \mathrm{W_0}}{\partial \mathrm{x}}\mathrm{dx} \\ & \left. - 2\int_0^{\mathrm{L}} \left(\mathrm{A_{55}(x)} + \mathrm{A_{66}(x)}\right)\beta_{\mathrm{y}}\frac{\partial \mathrm{V_0}}{\partial \mathrm{x}}\mathrm{dx}\right] \end{aligned} \tag{3. 9}$$

The strain energy expression in non-dimensional coordinates is given as follows:

$$E_d = \frac{1}{2L}\int_0^1 A_{00}(\xi)\left(\frac{\partial U_0}{\partial \xi}\right)^2 d\xi + \frac{1}{2L}\int_0^1 A_{11}(\xi)\left(\frac{\partial \beta_x}{\partial \xi}\right)^2 d\xi + \frac{1}{2L}\int_0^1 A_{11}(\xi)\left(\frac{\partial \beta_y}{\partial \xi}\right)^2 d\xi$$
$$+ \frac{1}{2}K_s\left[\frac{1}{L}\int_0^1 \left(A_{55}(\xi) + A_{66}(\xi)\right)\left(\frac{\partial V_0}{\partial \xi}\right)^2 d\xi\right.$$
$$+ \frac{1}{L}\int_0^1 \left(A_{55}(\xi) + A_{66}(\xi)\right)\left(\frac{\partial W_0}{\partial \xi}\right)^2 d\xi \qquad (3.10)$$
$$+ L\int_0^1 \left(A_{55}(\xi) + A_{66}(\xi)\right)\beta_x^2\, d\xi + L\int_0^1 \left(A_{55}(\xi) + A_{66}(\xi)\right)\beta_y^2\, d\xi$$
$$+ 2\int_0^1 \left(A_{55}(\xi) + A_{66}(\xi)\right)\beta_x \frac{\partial W_0}{\partial \xi} d\xi$$
$$\left. - 2\int_0^1 \left(A_{55}(\xi) + A_{66}(\xi)\right)\beta_y \frac{\partial V_0}{\partial \xi} d\xi\right]$$

With

$$A_{00}(x) = \pi\int_{R_i}^{R(\xi)} Q_{11}(\xi)\, r^3 dr A_{11}(\xi) = \pi\int_{R_i}^{R(\xi)} Q_{11}(\xi)\, r^3\, dr; \qquad (3.11)$$

$$A_{55}(\xi) = \pi\int_{R_i}^{R(\xi)} Q_{55}(\xi)\, r\, dr\,; \quad A_{66}(\xi) = A_{55}(\xi)$$

By introducing the shape function matrices $[N_U, N_V, N_W, \quad N_{\beta x}, \quad N_{\beta y}]$ into equation (3.10), the resulting expression is obtained as follows:

$$
\begin{aligned}
\mathrm{E_d} = \frac{1}{2\mathrm{L}}\int_0^1 \mathrm{A}_{00}(\xi)\,\{q_u\}^T[N'_U]^T[N'_U]\{q_U\}\mathrm{d}\xi \\
+\frac{1}{2\mathrm{L}}\int_0^1 \mathrm{A}_{11}(\xi)\,\{q_{\beta_x}\}^T\left[N'_{\beta_x}\right]^T\left[N'_{\beta_x}\right]\{q_{\beta_x}\}\mathrm{d}\xi \\
+\frac{1}{2\mathrm{L}}\int_0^1 \mathrm{A}_{11}(\xi)\left\{q_{\beta_y}\right\}^T\left[N'_{\beta_y}\right]^T\left[N'_{\beta_y}\right]\left\{q_{\beta_y}\right\}\mathrm{d}\xi \\
+\frac{1}{2}\mathrm{K_s}\left[\frac{1}{\mathrm{L}}\int_0^1 \left(\mathrm{A}_{55}(\xi)+\mathrm{A}_{66}(\xi)\right)\{q_\mathrm{V}\}^T[N'_\mathrm{V}]^T[N'_\mathrm{V}]\{q_\mathrm{V}\}\,\mathrm{d}\xi\right. \\
+\frac{1}{\mathrm{L}}\int_0^1 \left(\mathrm{A}_{55}(\xi)+\mathrm{A}_{66}(\xi)\right)\{q_\mathrm{W}\}^T[N'_\mathrm{W}]^T[N'_\mathrm{W}]\{q_\mathrm{W}\}\,\mathrm{d}\xi \\
+\mathrm{L}\int_0^1 \left(\mathrm{A}_{55}(\xi)+\mathrm{A}_{66}(\xi)\right)\{q_{\beta_x}\}^T\left[N_{\beta_x}\right]^T\left[N_{\beta_x}\right]\{q_{\beta_x}\}\mathrm{d}\xi \\
+\mathrm{L}\int_0^1 \left(\mathrm{A}_{55}(\xi)+\mathrm{A}_{66}(\xi)\right)\left\{q_{\beta_y}\right\}^T\left[N_{\beta_y}\right]^T\left[N_{\beta_y}\right]\left\{q_{\beta_y}\right\}\mathrm{d}\xi \\
+2\int_0^1 \left(\mathrm{A}_{55}(\xi)+\mathrm{A}_{66}(\xi)\right)\{q_{\beta_x}\}^T\left[N_{\beta_x}\right]^T[N'_\mathrm{W}]\{q_\mathrm{W}\}\mathrm{d}\xi \\
\left.-2\int_0^1 \left(\mathrm{A}_{55}(\xi)+\mathrm{A}_{66}(\xi)\right)\left\{q_{\beta_y}\right\}^T\left[N_{\beta_y}\right]^T[N'_\mathrm{V}]\{q_\mathrm{V}\}\mathrm{d}\xi\right]
\end{aligned}
\tag{3. 12}
$$

Where:

$$[N'_i] = \frac{\partial[N_i]}{\partial\xi}, \text{ with i = } (U, V, \mathrm{W}, \ \beta_x, \ \beta_y) \tag{3. 13}$$

From equation (2.33), the elemental stiffness matrix $[\mathrm{K_s^e}]$ is derived as follows:

$$\frac{\partial E_a}{\partial\{q_U\}} = \left[\frac{1}{L}\int_0^1 A_{00}[N'_U]^T\,[N'_U]\mathrm{d}\xi\right]\{q_U\} \tag{3. 14}$$

$$\Rightarrow[K_U]\{q_U\} \tag{3. 15}$$

$$\frac{\partial E_a}{\partial\{q_V\}} = \frac{1}{2}\mathrm{K_s}\left[\frac{1}{\mathrm{L}}\int_0^1 \big(\mathrm{A_{55}}(\xi)+\mathrm{A_{66}}(\xi)\big)\{q_\mathrm{V}\}^T[N'_\mathrm{V}]^T[N'_\mathrm{V}]\{q_\mathrm{V}\}\,\mathrm{d}\xi \right. \tag{3. 16}$$

$$\left. -2\int_0^1 \big(\mathrm{A_{55}}(\xi)+\mathrm{A_{66}}(\xi)\big)\left\{q_{\beta_\mathrm{y}}\right\}^T\left[N_{\beta_\mathrm{y}}\right]^T[N'_\mathrm{V}]\{q_\mathrm{V}\}\mathrm{d}\xi\right]$$

$$\Rightarrow [K_V]\{q_U\} + [K_1]\{q_\mathrm{V}\} \tag{3. 17}$$

$$\frac{\partial E_a}{\partial\{q_w\}} = \frac{1}{\mathrm{L}}\int_0^1 \big(\mathrm{A_{55}}(\xi)+\mathrm{A_{66}}(\xi)\big)\{q_\mathrm{W}\}^T[N'_\mathrm{W}]^T[N'_\mathrm{W}]\{q_\mathrm{W}\}\,\mathrm{d}\xi \tag{3. 18}$$

$$+2\int_0^1 \big(\mathrm{A_{55}}(\xi)+\mathrm{A_{66}}(\xi)\big)\left\{q_{\beta_\mathrm{x}}\right\}^T\left[N_{\beta_\mathrm{x}}\right]^T[N'_\mathrm{W}]\{q_\mathrm{W}\}\mathrm{d}\xi =$$

$$\Rightarrow [K_W]\{q_U\} + [K_2]\{q_\mathrm{W}\} \tag{3. 19}$$

$$\frac{\partial E_a}{\partial\{q_{\beta_\mathrm{x}}\}} = \frac{1}{2\mathrm{L}}\int_0^1 \mathrm{A_{11}}(\xi)\left\{q_{\beta_\mathrm{x}}\right\}^T 0g\left[N'_{\beta_\mathrm{x}}\right]^T\left[N'_{\beta_\mathrm{x}}\right]\{q_{\beta_\mathrm{x}}\}\mathrm{d}\xi$$

$$+\mathrm{L}\int_0^1 \big(\mathrm{A_{55}}(\xi)+\mathrm{A_{66}}(\xi)\big)\left\{q_{\beta_\mathrm{x}}\right\}^T\left[N_{\beta_\mathrm{x}}\right]^T\left[N_{\beta_\mathrm{x}}\right]\{q_{\beta_\mathrm{x}}\}\mathrm{d}\xi \tag{3. 20}$$

$$+2\int_0^1 \big(\mathrm{A_{55}}(\xi)+\mathrm{A_{66}}(\xi)\big)\left\{q_{\beta_\mathrm{x}}\right\}^T\left[N_{\beta_\mathrm{x}}\right]^T[N'_\mathrm{W}]\{q_\mathrm{W}\}\mathrm{d}\xi =$$

$$\Rightarrow \left[K_{\beta_\mathrm{x}}\right]\{q_{\beta_\mathrm{x}}\} + [K_2]\{q_\mathrm{W}\} \tag{3. 21}$$

$$\frac{\partial E_a}{\partial\left\{q_{\beta_y}\right\}} = \frac{1}{2L}\int_0^1 A_{11}(\xi)\{q\ \}^T\left[N'_{\beta_y}\right]^T\left[N'_{\beta_y}\right]\left\{q_{\beta_y}\right\}d\xi + L\int_0^1\left(A_{55}(\xi)+A_{66}(\xi)\right)\left\{q_{\beta_y}\right\}^T\left[N_{\beta_y}\right]^T\left[N_{\beta_y}\right]\left\{q_{\beta_y}\right\}d\xi - 2\int_0^1\left(A_{55}(\xi)+A_{66}(\xi)\right)\left\{q_{\beta_y}\right\}^T\left[N_{\beta_y}\right]^T[N'_V]\{q_V\}d\xi = \tag{3. 22}$$

$$\Rightarrow\left[K_{\beta_y}\right]\left\{q_{\beta_y}\right\} - [K_1]\{q_V\} \tag{3. 23}$$

Thus, the elemental stiffness matrix $[K_s^e]$ of the rotating shaft can be written in the following form:

$$[K_s^e] = \begin{bmatrix} [K_U] & 0 & 0 & 0 & 0 \\ 0 & [K_V] & 0 & 0 & [K_1] \\ 0 & 0 & [K_W] & [K_2] & 0 \\ 0 & 0 & [K_2]^T & \left[K_{\beta_x}\right] & 0 \\ 0 & [K_1]^T & 0 & 0 & \left[K_{\beta_y}\right] \end{bmatrix} \tag{3. 24}$$

3.1.3. Formulation of the elemental Mass $[M_s^e]$ and Gyroscopic $[G_s^e]$ matrices of the rotating shaft

Based on the simplified form of the shaft element's kinetic energy expressed in equation (2.28), we have:

$$E_c = \frac{1}{2}\int_0^L\left[I_m(x)\left(\dot{U}_0^2 + V_0^2 + \dot{W}_0^2\right) + I_d(x)\left(\dot{\beta}_x^2 + \dot{\beta}_y^2\right) - 2\Omega I_p(x)\beta_x\dot{\beta}_y + \Omega^2 I_p(x) + \Omega^2 I_d(x)\left(\beta_x^2+\beta_y^2\right)\right]dx$$

The expression of the kinetic energy of the rotating shaft, written in non-dimensional coordinates and after the introduction of the shape functions, is given as follows:

$$E_c = \frac{1}{2}L\int_0^1\left[I_m(\xi)\left(\dot{U}_0^2 + \dot{V}_0^2 + \dot{W}_0^2\right) + I_d(\xi)\left(\dot{\beta}_x^2 + \dot{\beta}_y^2\right) - 2\Omega I_p(\xi)\beta_x\dot{\beta}_y + \Omega^2 I_p(\xi) + \Omega^2 I_d(\xi)\left(\beta_x^2+\beta_y^2\right)\right]d\xi \tag{3. 25}$$

$$E_c = \frac{1}{2} L \left[\int_0^1 I_m(\xi) \{\dot{q}_U\}^T [N_U]^T [N_U] \{\dot{q}_U\} d\xi + \int_0^1 I_m(\xi) \{\dot{q}_V\}^T [N_V]^T [N_V] \{\dot{q}_V\} d\xi \right.$$
$$\left. + \int_0^1 I_m(\xi) \{\dot{q}_W\}^T [N_W]^T [N_W] \{\dot{q}_W\} d\xi \right]$$
$$+ \frac{1}{2} L \left[\int_0^1 I_d(\xi) \left\{\dot{q}_{\beta_x}\right\}^T \left[N_{\beta_x}\right]^T \left[N_{\beta_x}\right] \left\{\dot{q}_{\beta_x}\right\} d\xi \right. \quad (3.26)$$
$$\left. + \int_0^1 I_d(\xi) \left\{\dot{q}_{\beta_y}\right\}^T \left[N_{\beta_y}\right]^T \left[N_{\beta_y}\right] \left\{\dot{q}_{\beta_y}\right\} d\xi \right]$$
$$- \Omega \; L \left[\int_0^1 I_p(\xi) \left\{q_{\beta_x}\right\}^T \left[N_{\beta_x}\right]^T \left[N_{\beta_y}\right] \left\{\dot{q}_{\beta_y}\right\} d\xi + \frac{L}{2} \Omega^2 \, I_p(\xi) \, d\xi \right]$$

From equation (2.33), the expressions for the elemental mass matrix $[\mathrm{M}_s^e]$ and the gyroscopic matrix $[\mathbf{G}_\mathbf{s}^\mathbf{e}]$ are obtained as follows:

$$\frac{d}{dt}\left(\frac{\partial E_C}{\partial \{\dot{q}_U\}}\right) - \frac{\partial E_c}{\partial \{q_U\}} = \left[L \int_0^1 I_m(\xi) \, [N_U]^T \, [N_U] \, d\xi \right] \{\ddot{q}_U\} = [M_U] \{\ddot{q}_U\} \quad (3.27)$$

$$\frac{d}{dt}\left(\frac{\partial E_C}{\partial \{\dot{q}_V\}}\right) - \frac{\partial E_c}{\partial \{q_V\}} = \left[L \int_0^1 I_m(\xi) \, [N_V]^T \, [N_V] \, d\xi \right] \{\ddot{q}_V\} = [M_V] \{\ddot{q}_V\} \quad (3.28)$$

$$\frac{d}{dt}\left(\frac{\partial E_C}{\partial \{\dot{q}_W\}}\right) - \frac{\partial E_c}{\partial \{q_W\}} = \left[L \int_0^1 I_m(\xi) \, [N_W]^T \, [N_W] \, d\xi \right] \{\ddot{q}_W\} = [M_W] \{\ddot{q}_W\} \quad (3.29)$$

$$\frac{d}{dt}\left(\frac{\partial E_C}{\partial \{\dot{q}_{\beta_x}\}}\right) - \frac{\partial E_c}{\partial \{q_{\beta_x}\}}$$
$$= \left[L \int_0^1 I_d(\xi) \left[N_{\beta_x}\right]^T \left[N_{\beta_x}\right] d\xi \right] \{\ddot{q}_{\beta_x}\} \quad (3.30)$$
$$+ \left[L\Omega \int_0^1 I_p(\xi) \left[N_{\beta_x}\right]^T \left[N_{\beta_y}\right] \, d\xi \right] \left\{\dot{q}_{\beta_y}\right\} = \left[M_{\beta_x}\right] \{\ddot{q}_{\beta_x}\} + [G_1] \left\{\dot{q}_{\beta_y}\right\}$$

$$\frac{d}{dt}\left(\frac{\partial E_C}{\partial\left\{\dot{q}_{\beta_y}\right\}}\right)-\frac{\partial E_c}{\partial\left\{q_{\beta_y}\right\}} = \left[L\int_0^1 I_d(\xi)\,\left[N_{\beta_y}\right]^T\left[N_{\beta_y}\right]\,d\xi\right]\left\{\ddot{q}_{\beta_y}\right\} + \left[L\Omega\int_0^1 I_p(\xi)\,\left[N_{\beta_y}\right]^T\left[N_{\beta_x}\right]d\xi\right] = \left[M_{\beta_x}\right]\left\{\ddot{q}_{\beta_y}\right\}-[G_1]^T\left\{\dot{q}_{\beta_x}\right\} \tag{3. 31}$$

So,

$$[\mathrm{M}_\mathrm{s}^\mathrm{e}] = \begin{bmatrix} [M_U] & 0 & 0 & 0 & 0 \\ 0 & [M_V] & 0 & 0 & 0 \\ 0 & 0 & [M_W] & 0 & 0 \\ 0 & 0 & 0 & \left[M_{\beta_x}\right] & 0 \\ 0 & 0 & 0 & 0 & \left[M_{\beta_y}\right] \end{bmatrix} \tag{3. 32}$$

and

$$[\mathrm{G}_\mathrm{s}^\mathrm{e}] = \begin{bmatrix} 0 & 0 & 0 & 0 & 0 \\ 0 & 0 & 0 & 0 & 0 \\ 0 & 0 & 0 & 0 & 0 \\ 0 & 0 & 0 & 0 & [G_1] \\ 0 & 0 & 0 & -[G_1]^T & 0 \end{bmatrix} \tag{3. 33}$$

The integrals in expression (3.24, 3.41 and 3.42) are of the following form

$$J_{mn}^{\alpha\beta} = \int_0^1 f_m^\alpha(\xi)\, f_n^\beta(\xi)\, d\xi \tag{3. 34}$$

3.1.4. Final form of the governing equations of motion

Accordingly, equation (2.8) after discretizing the system using the *p*-version of the finite element method and applying Lagrange's formalism, the following system of differential equations is obtained.

$$[M]\{\ddot{q}\} + [G]\{\dot{q}\} + [K]\{q\} = \{0\}$$

The shape functions of the spinning flexible shaft are discretized using a hierarchical beam element (*p*-element) consisting of two nodes is shown in Figure 3.1, at each node are U_0 V_0, W_0, β_x and β_y.

The variables U_0, V_0, W_0, β_x and β_y can form the following vector displacement [49]:

$$\begin{aligned} U_0 &= [N_V]\{q_U\} = \sum_{m=1}^{Pv} y_m\,(t)\mathfrak{f}_m(\xi)\,; \\ V_0 &= [N_V]\{q_V\} = \sum_{m=1}^{Pv} y_m\,(t)\mathfrak{f}_m(\xi)\,; \\ W_0 &= [N_w]\{q_w\} = \sum_{m=1}^{Pw} z_m\,(t)\mathfrak{f}_m(\xi)\,; \\ \beta_x &= \left[N_{\beta_x}\right]\{q_V\} = \sum_{m=1}^{P\beta_x} \beta_{x_m}\,(t)\mathfrak{f}_m(\xi)\,; \\ \beta_y &= \left[N_{\beta_y}\right]\{q_V\} = \sum_{m=1}^{P\beta_y} \beta_{y_m}\,(t)\mathfrak{f}_m(\xi)\,; \end{aligned} \tag{3. 35}$$

Thus, based on equation (3.5), the differential system described in equation (2.35) can be rewritten as:

$$(-\omega^2[M] + \mathrm{j}\omega[G] + [K])\{q\} = \{0\} \tag{3. 36}$$

Where ω is the system's natural pulsation, and $\{w\}$ is the corresponding eigenvector.

Chapter 4

4. Structure and Planning of the Programming Process

4.1. Introduction

The Finite Element Method (FEM) consists in discretizing a structure into simple-shaped elements and selecting an appropriate approximation of the displacement field within each subdivision. In the study of natural phenomena in general, or engineering problems in particular, it is often necessary to construct a mathematical model capable of representing the problem as accurately as possible. With the remarkable advancements in computer science and the increasing computational capabilities of modern machines, numerous numerical solution techniques have been developed and successfully applied to a wide range of engineering problems. Among these, the FEM stands out as one of the most powerful and versatile tools.

In the present research, a MATLAB-based computational program has been developed using the p-version formulation of the hierarchical finite element method to perform the modal analysis of rotating shafts composed of axially graded functionally graded material (FGM). The shafts considered exhibit non-uniform geometries, either solid or hollow, described by a variety of profiles, including parabolic, conical, hyperbolic, and exponential shapes. This formulation enhances numerical accuracy and flexibility by increasing the polynomial order of the element shape functions rather than refining the mesh, making it particularly suitable for complex structural dynamics problems.

The program computes the natural frequencies of the system for various boundary conditions and a wide range of physical and geometric parameters, while also accounting for different rotational speeds, from stationary conditions to high-speed regimes. The computational framework is organized into modular subroutines, covering data input, variable declaration, element-level matrix formulation, global matrix assembly, application of boundary conditions, and eigenvalue extraction. MATLAB's linear algebra capabilities are leveraged to efficiently solve the eigenvalue problem and obtain both the natural frequencies and the corresponding mode shapes of the rotating shaft.

The program consists of three main components:

- Input files used to define the geometric, material, and boundary condition data;
- The computational core implementing the *p*-version of the finite element method;
- An output file containing the results of the modal analysis.

4.2. Matlab – Historical Background

MATLAB is a powerful and user-friendly environment for scientific computation developed by **The MathWorks, Inc.** It integrates numerical analysis, graphical visualization, and programming within a single platform. Based on matrix manipulation, it enables efficient and reliable numerical and symbolic analyses. Through its specialized **Toolboxes**, MATLAB provides targeted solutions for various engineering and research fields. Its intuitive programming language and compatibility with **C** and **Fortran** make it an essential tool for modeling, simulation, and the analysis of complex systems.

4.3. Computational flowchart

Figure 4.1 presents the main stages of the implemented computational procedure, which are outlined as follows:

- Reading of all physical and geometrical input data for the system components (shaft, and bearings).
- Reading of all precomputed integral values $J_{mn}^{\alpha\beta}$.
- Construction of the element-level matrices $[K]^e$ $[M]^e$ and $[G]^e$ (refer to Chapter 3).
- Assembly of the global matrices $[K]$ $[M]$ and $[G]$, based on the prescribed boundary conditions.
- Formation of the transformed matrices $[A]$ and $[B]$, which define the generalized eigenvalue problem to be solved.
- The program outputs the eigenvalues $[\omega]$ and the corresponding eigenvectors $\{w\}$, representing the system's natural frequencies and mode shapes.

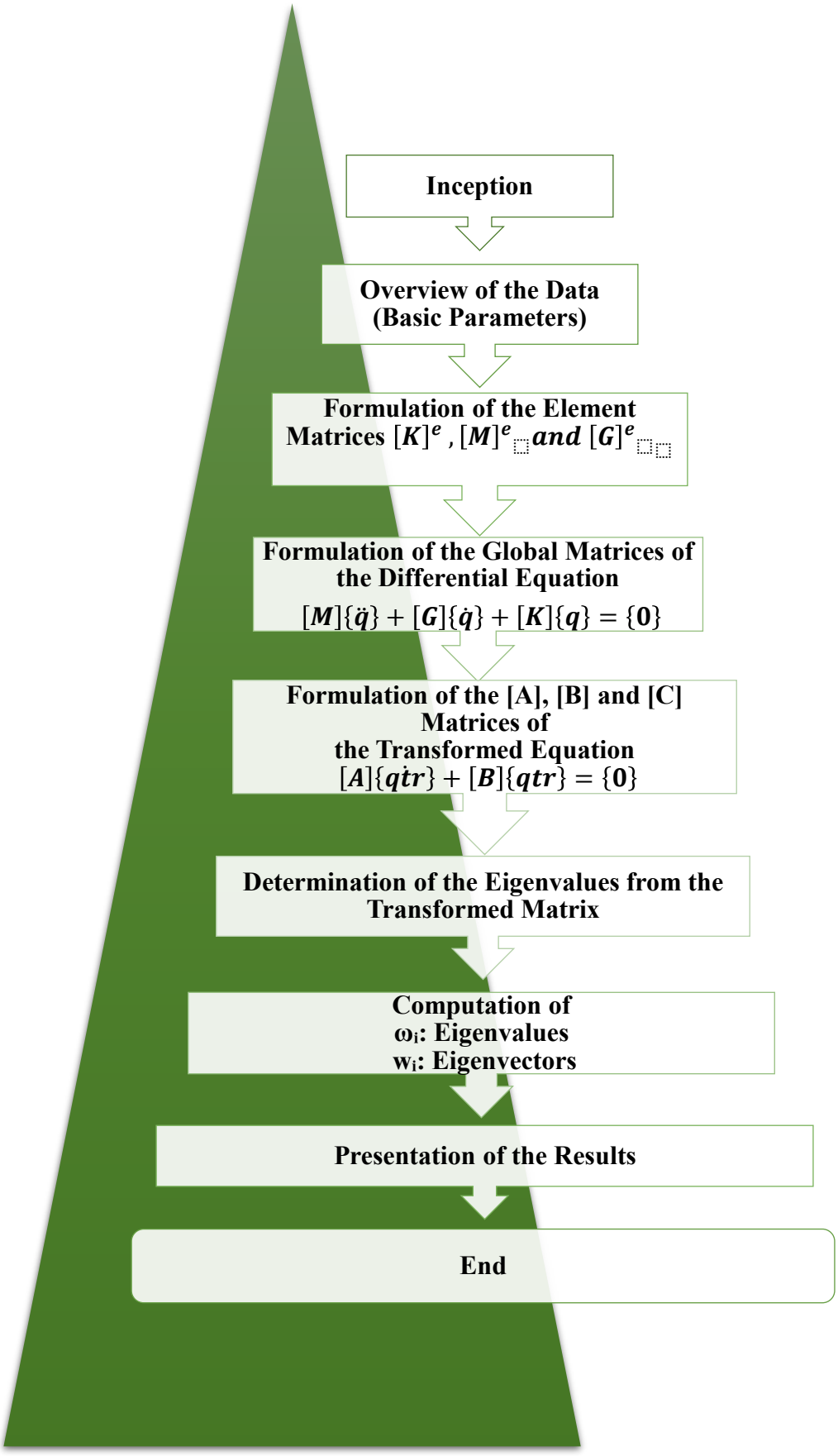

Fig 4. 1 Schematic Representation of the Computation

4.4. Program description

Our programming approach relies on subroutines, which are sequences of instructions that can be invoked from any point within the program. These subroutines may be called either from the main program or from another subroutine or function.

4.4.1. Input data files

The input file functions as a data entry module. It must provide sufficient information to the other modules to enable the problem to be solved. The data can be entered through the following steps:

1) The parameters of the hierarchical finite element method
   - $$\left\{\begin{array}{c} \mathrm{f}_1 = 1 - \xi \\ \mathrm{f}_2 = \xi \\ \mathrm{f}_{i+2} = sin(\delta_i.\xi) \\ \delta_i = i\pi;\ \ i = 1,2,3,.. \end{array}\right\}$$
2) The physical and geometric parameters of the non-uniform FGM shaft
   - R_0 of the radius at $x = 0$,
   - R_1 the radius at $x = L$ of the non-uniform shaft
   - a is the radius coefficient
   - L is the length of the shaft.
   - *E1,2* Young's modulus
   - $\rho 1,2$ Density
   - $\nu 1,2$ Poisson's ratio
   - $\mathrm{K_s}$ factor accounting for transverse shear effects
   - n Power law index
   - P Number of the shape functions or number of hierarchical terms.
   - Ω Rotating speed
3) Variable declaration,
   - $\rho(x)$
   - $\nu(\xi)$
   - $E(x)$
   - $R(x)$
   - $A_{11}(\xi);\ A_{11}(\xi);\ A_{11}(\xi)$
   - $I_p\ (\xi)$

- $I_m\ (\xi)$
- $I_d\ (\xi)$
- $Q_{11}(\xi), Q_{55}(\xi)$

4) The boundary conditions.
   - C-C; Clamped-Clamped
   - P-P; Pinned-Pinned
   - C-P; Clamped-Pinned
   - P-F; Pinned-Free
   - C-F. Clamped-Free

Node: Number of nodes (1 and 2).
Each node has 5 degrees of freedom, which are:

- U**:** Displacement along the x-axis.
- V**:** Displacement along the y-axis.
- W**:** Displacement along the z-axis.
- β_x**:** Rotation of the cross-section about the y-axis.
- β_y**:** Rotation of the cross-section about the z-axis.

Table 4. 1 Introduction of boundary conditions

Node	U	V	W	β_x	β_y
Node 1	1 or 0	1 or 0	1 or 0	1 or 0	1 or 0
Node 2	1 or 0	1 or 0	1 or 0	1 or 0	1 or 0

The cells in Table 4.1 take the value 0 if the displacement or rotation is constrained (zero), and 1 if the nodes are free.

5) Calcul integrales
   - $[K]^e$, $[M]^e$, $[G]^e$.

6) Matrix Assembly based on the equation $[\mathrm{A}]\{\dot{\mathrm{q}}\mathrm{tr}\} + [\mathrm{B}]\{\mathrm{qtr}\} = \{0\}$
   - $[K]$, $[M]$, $[G]$,
   - $[A] = \begin{bmatrix} [M] & [0] \\ [0] & [I] \end{bmatrix}$
   - $[B] = \begin{bmatrix} [G] & [K] \\ -[I] & [0] \end{bmatrix}$

- $[C] = [A]^{-1}[B]$

7) Problem solving Eigenvalues and Eigenvectors
   - $[\omega_i, w_i]$ = eig (C)
   - ω_i: Eigenvalues
   - w_i: Eigenvectors

Each set of data is essential to ensure the accurate resolution of the problem by the computational modules.

Chapter 5

5. Numerical Results and Discussion

5.1. Introduction

In this chapter, we present the results obtained from our computational model through various application examples. The convergence behavior is examined by increasing the number of hierarchical shape functions per element. The reliability of the proposed model is validated through extensive comparisons between the numerical and analytical results, as well as with reference data from the literature. This study paves the way for innovative industrial applications involving advanced rotating structures.

The developed model enables the analysis of the system's whirl frequencies, critical rotational speeds, and the influence of key parameters on the dimensionless natural frequencies and overall dynamic stability. These parameters include slenderness ratio, material composition, axial variation, variable rotational speed, and the power-law index, all assessed under different boundary conditions (B.C.). The results provide insights into the impact of these factors on the performance of rotating hollow non-uniform shafts as shown in the Figure 5.1.

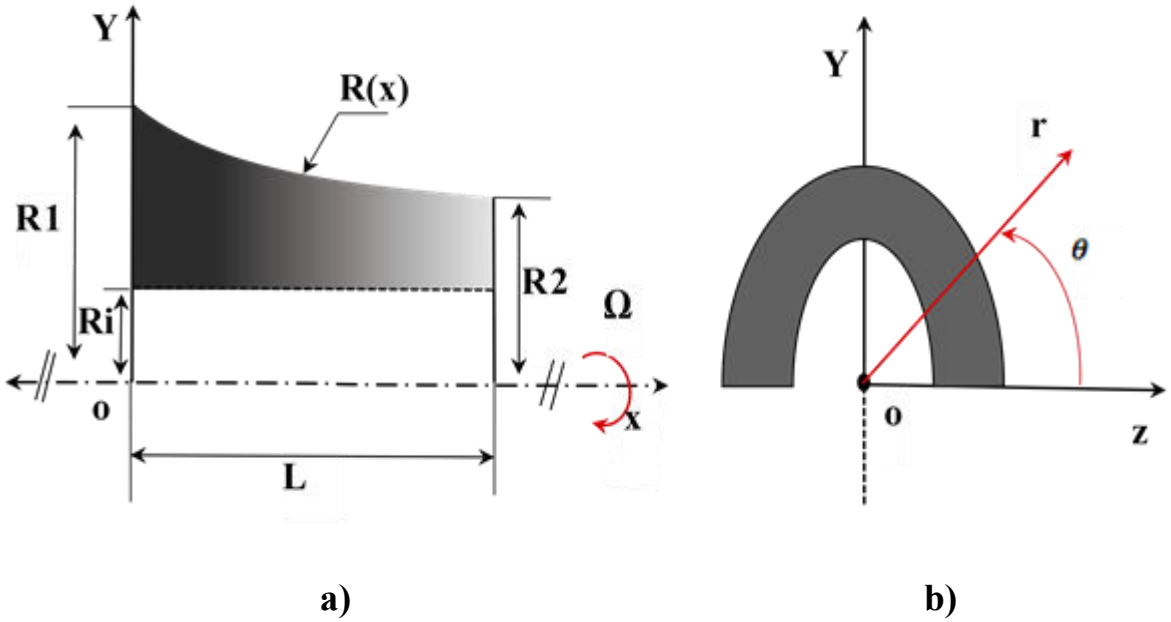

Fig 5. 1 Schematic representation of a hollow rotating shaft with axial material gradation.
a) Perspective view of the spinning shaft, b) orthogonal view of its cross-section.

5.2. Numerical convergence and validation study

5.2.1. Convergence

In this section, Figure 5.2 presents the first four bending mode results for the proposed rotating hollow parabolic shaft, defined by a radius coefficient of $a = 0.01$, a rotational speed of $\Omega = 2500$ rad/s, and a material power-law index $n = 2$. The results are shown for varying numbers of hierarchical shape functions (p ranging from 5 to 15) and under different boundary conditions: clamped-free (C–F), clamped-clamped (C–C), pinned-pinned (P–P), pinned-free (P–F), and clamped-pinned (C–P). The plot clearly demonstrates the rapid convergence of the computed dimensionless natural frequencies as the number of shape functions increases. Both backward and forward frequency modes are observed and their values tend to converge and stabilize, particularly when the number of elements exceeds six. Remarkably, at $p = 10$, the solution achieves substantial convergence, validating the accuracy and efficiency of the proposed method. Consequently, a value of $p = 10$ is adopted for all subsequent calculations.

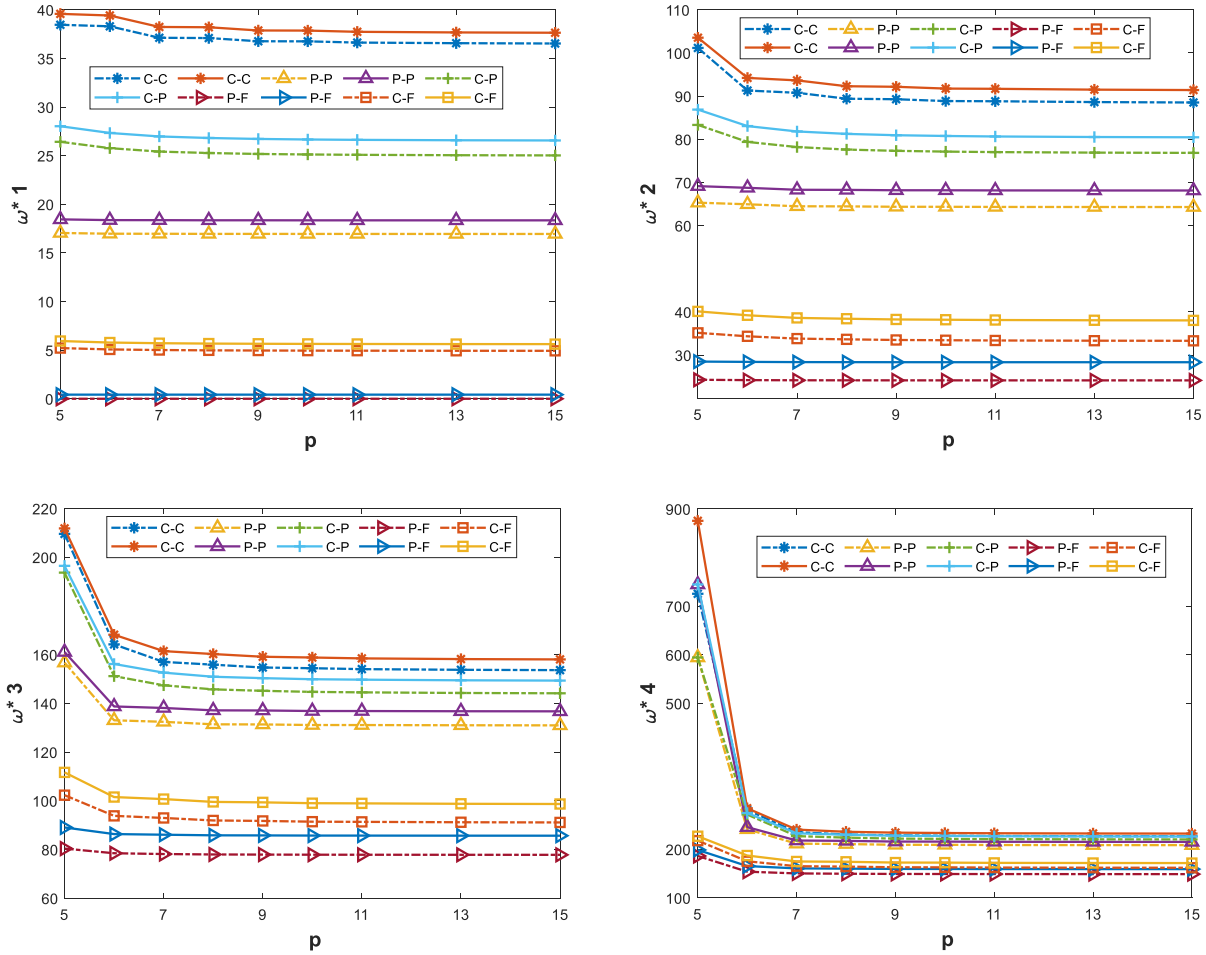

Fig 5. 2 Beam Convergence of the first four dimensionless natural frequencies for different boundary conditions; C-C; P-P C-P and C-F as the number of hierarchies of functions p at a speed of 2500 $rad.s^{-1}$.

5.2.2. Validation

This section aims to validate the accuracy of the natural frequencies computed using the *p*-version of the finite element method *p*-FEM through comparisons with established results from the literature.

The first validation case involves a uniform, homogeneous rotating shaft subjected to various boundary conditions. Reference results are obtained using the Differential Quadrature Method (DQM) [50], the Spectral Chebyshev Method STM [29], and the State-Space Method (SSM) based on Euler–Bernoulli beam theory [51]. The shaft's physical and mechanical properties are defined as: density $\rho = 7800$ kg/m³, Young's modulus $E = 200$ GPa, length $L = 1.3$ m, radius $R_0 = 0.025$ m, rotational speed $\Omega = 500$ rad/s, and shear correction factor $K_s = 0.88$. The corresponding results, listed in Table 5.1, include both forward (*Fw*) and backward (*Bw*) natural frequencies. The minimal discrepancies observed reinforce the accuracy, validity, and robustness of the proposed formulation. These differences can be primarily attributed to distinct modeling assumptions and numerical discretization schemes.

The second validation case focuses on a uniform shaft composed of axially functionally graded materials (FGMs), as investigated by [29, 52]. Results are obtained under both stationary and rotating conditions using the Differential Transformation Element Method (DTEM) and the SCM. Comparative values are presented in Tables 5.2 and 5.3, showing deviations of less than 5%, thereby confirming the method's accuracy even for rotating systems incorporating material gradation.

The third case considers a non-uniform shaft geometry under various boundary conditions and conicity parameters. Numerical results, summarized in Tables 5.4 and 5.5, are compared with those reported by [52, 53], and [54], who employed DTEM, DQEL, standard FEM, and the Spectro-Geometric Method (SGM) within the framework of Timoshenko beam theory. Despite differences in numerical schemes and modeling assumptions, the proposed p-version FEM consistently aligns with published data, highlighting its effectiveness and robustness for analyzing non-uniform spinning shafts.

Table 5. 1 First four angular frequencies rad. s^{-1} of uniform rotating shaft made homogeneous materials.

BC		DQM [50]		STM [29]		SSM [51]		**Present**	
		Fw	Bw	Fw	Bw	Fw	Bw	Fw	Bw
S–S	*f*	735.818	732.258	735.820	732.260	741.127	737.477	770.784	767.236
	f	2882.80	2869.54	2882.86	2869.60	2964.50	2949.90	3015.31	3002.23
	f	6280.74	6254.04	6281.43	6254.77	6670.14	6637.29	6553.77	6527.79
	f	10,717.9	10,676.6	10663.3	10623.0	11,858.0	11,799.6	11170.1	11130.6
C–	*f*	1631.02	1626.94	1631.04	1626.96	1678.18	1673.63	1749.69	1745.58
	f	4343.24	4329.44	4343.42	4329.60	4628.23	4611.20	4614.62	4601.03
	f	8163.07	8136.95	8162.21	8136.43	9074.78	9038.21	8693.58	8668.46
	f	12,847.4	12,809.1	12630.2	12594.1	15,002.58	14,939.1	13527.8	13491.4
C–	*f*	1137.83	1133.80	1137.84	1133.81	1157.05	1152.80	1205.71	1201.67
	f	3587.19	3573.51	3587.30	3573.61	3750.64	3734.78	3785.74	3772.2
	f	7206.41	7179.96	7207.82	7181.40	7826.26	7791.48	7595.59	7569.9
	f	11,781.4	11,741.4	11683.8	11645.3	13,384.1	13,323.1	12354.1	12315.9
C–	*f*	263.334	261.635	263.335	261.636	264.503	262.782	279.388	277.67
	f	1618.49	1607.18	1618.52	1607.20	1662.43	1650.37	1713.38	1702.02
	f	4395.50	4370.97	4395.54	4370.99	4663.03	4634.13	4636.38	4612.01
	f	8272.69	8232.56	8279.47	8239.30	9157.59	9103.94	8710.73	8671.47
S–F	*f*	0	0	/	/	0	0	0	0
	f	1147.01	1137.25	/	/	1163.36	1153.24	1201.26	1191.53
	f	3626.27	3602.57	/	/	3775.70	3749.13	3790.29	3766.89
	f	7305.65	7265.40	/	/	7893.68	7843.11	7621.2	7581.84
F–F	*f*	0	0	/	/	0	0	0	0
	f	0	0	/	/	0	0	0	0
	f	1658.89	1641.36	/	/	1687.45	1675.95	1736.86	1719.41
	f	4444.36	4408.59	/	/	4661.26	4632.29	4642.58	4607.22

Table 5. 2 Dimensionless natural frequencies of uniform shaft made axially FGM.

BC	*fi*	*n = 1*			*n* = 2			*n* = 3		
		DTEM [52]	**Present**	Error	DTEM [52]	**Present**	Error	DTEM [52]	**Present**	Error
CF	*f1*	3.8963	4.0571	4.13%	3.8829	4.0437	4.14%	3.7957	3.9534	4.15%
	f2	15.0512	15.4563	2.69%	15.2597	15.6632	2.64%	15.2943	15.6946	2.62%
	f3	30.942	31.6088	2.15%	31.6198	32.303	2.16%	31.998	32.6886	2.16%
	f4	46.382	47.0973	1.54%	47.6387	48.3927	1.58%	48.3373	49.1042	1.59%
PP	*f1*	7.8461	8.1336	3.66%	7.9874	8.2741	3.59%	8.0646	8.3522	3.57%
	f2	23.9417	24.5334	2.47%	24.2532	24.8412	2.42%	24.3543	24.9392	2.40%
	f3	41.6814	42.388	1.70%	42.305	43.0163	1.68%	42.5036	43.2159	1.68%
	f4	53.7201	53.7737	0.10%	54.8862	54.9436	0.10%	55.3972	55.4622	0.12%
CC	*f1*	12.9072	13.1537	1.91%	12.6879	12.9296	1.90%	12.6036	12.8442	1.91%
	f2	26.7614	27.1357	1.40%	26.6433	27.0182	1.41%	26.5827	26.9587	1.41%
	f3	43.0446	43.6039	1.30%	43.3724	43.9566	1.35%	43.4988	44.0969	1.37%
	f4	58.5242	59.2341	1.21%	59.2817	60.009	1.23%	59.5763	60.3143	1.24%

Table 5. 3 Naturel frequencies of the rotating uniform shaft made of axially FGM at Ω = 1500 Hz.

BC		n = 1		*n* = 2		*n* = 3	
		STM [29]	**Present**	STM [29]	**Present**	STM [29]	**Present**
C-F	Bw_1	158.6	167.9	157.7	167.3	153.9	163.3
	Fw_1	165.1	174.5	164.2	173.9	160.2	169.7
	Bw_2	818.2	865.3	835.9	884.6	842.6	891.8
	Fw_2	855.3	902.3	872.3	921	879	928.2
	Bw_3	2111.7	2224.3	2162.6	2279	2192.7	2310.9
	Fw_3	2192	2303.7	2242.1	2357.5	2271.8	2389.1
C-C	Bw_1	762.5	814.9	750.5	804.5	745.7	800.7
	Fw_1	769.2	827.9	756.7	816.9	751.6	812.8
	Bw_2	2015.9	2148.3	2018.2	2153.4	2018.9	2155.7
	Fw_2	2075.7	2191.4	2077.2	2195.9	2077.4	2197.9
	Bw_3	3739.5	4046.5	3772.7	4088.7	3786.4	4105.9
	Fw_3	3948.6	4125.3	3982	4166.8	3995.5	4183.7
P-P	Bw_1	347.9	360.2	356.8	369.7	361	374.3
	Fw_1	350.6	371.5	359.3	380.4	363.5	384.6
	Bw_2	1353.5	1414.7	1381	1444.1	1392.8	1456.7
	Fw_2	1392.4	1456.5	1419.9	1485.1	1431.6	1497.3
	Bw_3	2899.1	3067.7	2958.1	3131.1	2984.3	3159.1
	Fw_3	3068.6	3150.3	3129.2	3212.8	3155.9	3240.4

Table 5. 4 Dimensionless natural frequencies of tapered shaft made of axially FGM (C–C, n = 2)

a	fi	DTEM [52]	DQEL [52]	FEA [53]	**Present**
0.1	f1	12.4633	12.4631	12.4689	12.0877
	f2	26.3804	26.38	26.4153	26.1435
	f3	42.9606	42.96	43.0904	42.7645
	f4	59.3916	59.3907	59.6829	60.0199
0.2	f1	12.2068	12.2067	12.2126	11.8284
	f2	26.068	26.0677	26.1023	25.8040
	f3	42.4941	42.4935	42.6211	42.2729
	f4	59.1821	59.1812	59.4873	59.5420
0.3	f1	11.9112	11.911	11.9172	11.5408
	f2	25.6899	25.6895	25.7236	25.4064
	f3	41.952	41.9514	42.0759	41.7110
	f4	58.7488	58.7479	59.0576	58.9548

Table 5. 5 Dimensionless natural frequencies of shaft with parabolic profile made of axially FGM

BC		C-C			C-F			P-P		
	fi	SGM [54]	**Present**	Error	SGM [54]	**Present**	Error	SGM [54]	**Present**	Error
n = 0	*f*1	20.4	21.1693	3.77%	2.5968	2.7219	4.82%	6.7763	7.0929	4.67%
	*f*2	46.445	47.8311	2.98%	16.1178	16.8001	4.23%	27.6868	28.8054	4.04%
	*f*3	79.9726	81.8769	2.38%	42.5372	44.0433	3.54%	60.1835	62.1744	3.31%
	*f*4	118.7607	120.6287	1.57%	77.2404	79.4634	2.88%	99.9577	102.5802	2.62%
n = 1	*f*1	19.9815	20.7488	3.84%	3.5198	3.6794	4.53%	6.7239	7.0377	4.67%
	*f*2	45.8655	47.247	3.01%	17.8649	18.5986	4.11%	27.8181	28.9366	4.02%
	*f*3	79.3142	81.2274	2.41%	44.1997	45.7372	3.48%	60.2387	62.2265	3.30%
	*f*4	118.0639	119.9478	1.60%	78.8305	81.0766	2.85%	99.9512	102.5776	2.63%
n = 2	*f*1	19.123	19.8877	4.00%	3.5163	3.673	4.46%	6.7656	7.0799	4.65%
	*f*2	44.7408	46.1175	3.08%	17.7166	18.4435	4.10%	27.899	29.016	4.00%
	*f*3	78.0625	79.987	2.47%	44.1692	45.6999	3.47%	60.2037	62.1845	3.29%
	*f*4	116.7557	118.6624	1.63%	78.8983	81.1287	2.83%	99.8401	102.4708	2.63%

5.3. Parametric study

In this section, a computational program has been developed to investigate the influence of various physical and geometrical parameters on the vibrational behavior of spinning hollow shafts both uniform and non-uniform profile composed of axially functionally graded materials (FGMs). The studied FGM configurations include **Al/Al_2O_3**, **Al/ZrO_2**, **Ti–6Al–4V/Al_2O_3**, and **SUS304/Si_3N_4**, with the corresponding constituent material properties listed in Table 5.6.

The first four dimensionless natural frequencies were computed and are presented in Table 5.7, for several boundary conditions: clamped-free (C–F), clamped-clamped (C–C), pinned-pinned (P–P), pinned-free (P–F), and clamped-pinned (C–P). The shaft dimensions are defined by inner and outer radius: R_i = 0.019 m and R_1 = 0.024 m, respectively, and a length L = 0.78 m. The power-law index is set to n = 2, with a shear correction factor K_s = 0.5. The dimensionless radius of gyration is taken as I_0/A_0 = 0.000144. The dimensionless natural frequencies are defined according to equation 5.1, as proposed by [54]

Table 5. 6 Material properties of FGM materials [55].

Material	Elasticity modulus (GPa)	Poisson's ratio	Density
Aluminium (Al)	70	0.3	2707
Alumina (Al2O3)	380	0.3	3800
Ti-6Al-4V	105.7	0.298	4429
Aluminium oxide	320.2	0.26	3750
Zirconia (ZnO2)	200	0.3	5700
Stainless steel SUS304	207.78	0.3177	8166
Silicon nitride	322.27	0.24	2370

Table 5. 7 First four-frequency naturel of different types axially functionally graded materials

BC		Ti-6Al-4V Titan /Aluminium oxide	Zirconia ($\mathbf{ZrO_2}$) /Aluminium (Al)	SUS304/Silicon nitride $\mathbf{Si_3N_4}$	Aluminium (Al) /Alumina ($\mathbf{Al_2O_3}$)
C-C	f1	177.3269	127.9511	166.4459	194.4161
	f2	456.3336	337.3557	437.3163	493.8131
	f3	838.4149	626.8229	811.036	901.2978
	f4	1282.1281	963.0762	1245.3851	1373.3056
C-F	f1	24.8369	27.5309	31.867	22.0399
	f2	164.3401	144.1943	175.7957	168.4357
	f3	453.3256	365.0842	459.323	479.9524
	f4	841.0756	662.4798	838.2733	894.2661
P-P	f1	77.1586	60.5978	74.5896	83.4749
	f2	304.5111	234.0939	297.4733	328.8314
	f3	652.6147	499.3311	639.4973	701.7627
	f4	1092.0777	834.4909	1069.9139	1171.4893
C-P	f1	118.1691	96.2729	118.0185	124.0939
	f2	374.9011	290.1739	367.3568	401.3826
	f3	738.947	568.2406	723.3553	790.3027
	f4	1181.1173	906.6016	1154.7068	1261.6972
P-F	f1	0	0	0	0
	f2	116.2219	103.2392	125.4859	119.987
	f3	377.2754	304.7049	384.324	401.385
	f4	752.5165	591.5466	753.2154	803.4511

The dimensionless natural frequency is defined as follows equation 5.1:

$$\omega^* = \omega L^2 \sqrt{\frac{\rho_0 A_0}{E_0 I_0}} \tag{5. 1}$$

where ω is the natural frequency in rad/s.

Following a comparative analysis of various axially functionally graded materials, and based on the results presented in Table 5.7, the FGM composed of Zirconia (ZrO_2) and Aluminum (Al) was selected for the remainder of the study. This choice is motivated by its balanced performance in terms of dimensionless natural frequencies under different boundary conditions. Specifically, this material shows lower frequencies under the Clamped-Free (C–F) condition, which is advantageous for vibration mitigation, and higher frequencies under the Clamped-Clamped (C–C) condition, which promotes dynamic stability. These characteristics make it a suitable candidate for rotating shaft applications.

Accordingly, the subsequent analysis focuses on the ZrO_2/Al configuration. Table 5.8 presents the first dimensionless natural frequencies for various hollow shaft geometries namely **parabolic**, **exponential**, **conical**, and **cylindrical** profiles under different boundary conditions, and for both stationary and rotating cases. The shaft geometry is defined by an inner radius R_i = 0.05 m, outer radius R_1 = 0.15 m, and length L = 3 m. The power-law index is set to n = 0.2, and the transverse shear correction factor is K_s=0.5. The mechanical properties of the ZrO_2/Al FGM are provided in Table 5.8.

Table 5. 8 First dimensionless natural frequencies for different hollow profiles made of axially FGM.

Profile Hollow:		Cylandrique		Conical		Parabolic		Exponential	
Radius coefficient		a= 0		a=0.04		a= 0.01		a = 0.1	
B.C	[Rad/s]	Bw1	Fw1	Bw1	Fw1	Bw1	Fw1	Bw1	Fw1
C-C	Ω = 0	31.4854	31.4854	30.2498	30.2498	37.3073	37.3073	34.875	34.875
	Ω = 15000	28.9637	34.0208	27.8733	32.6574	33.9585	40.5636	31.8895	37.801
C-F	Ω = 0	7.0487	7.0487	7.4991	7.4991	5.2888	5.2888	6.0925	6.0925
	Ω = 15000	5.539	8.8019	6.0603	9.152	3.5182	7.4583	4.3535	8.1942
P-F	Ω = 0	0	0	0	0	0	0	0	0
	Ω=15000	0	2.2652	0	2.2416	0	2.4387	0	2.5145
P-P	Ω = 0	15.4753	15.4753	14.541	14.541	17.6386	17.6386	17.7109	17.7109
	Ω = 15000	13.0278	18.2898	12.2541	17.1764	13.8521	22.1413	14.6157	21.2715

5.3.1. Influence of the gyroscopic effect and the boundary conditions.

In this study, a computational model was developed to analyze the influence of various physical and geometric parameters on the vibrations of a spinning hollow parabolic shaft-rotor made of axially functionally graded materials (FGMs). The material properties are provided in Table 5.6, with a shear modulus ratio of K_s = 0.5. Figure 5.3 presents the Campbell diagram, illustrating the gyroscopic effect on the first backward Bw_1 and forward Fw_1 vibration modes under different boundary conditions: pinned-pinned, clamped-clamped, clamped-free, and clamped-pinned. Here, f(Ω) denotes the dimensionless natural frequency when $\Omega \neq 0$, while f_0 corresponds to the stationary frequency Ω = 0, which corresponds to the stationary case. The gyroscopic effect in spinning shafts induces processional motion. As the rotational speed increases, the forward modes increase, whereas the backward modes decrease. This phenomenon has a significant impact on the dynamic behavior of spinning shafts. The numerical results in Figure 5.3 clearly demonstrate the influence of the gyroscopic effect, highlighting the shifts in vibration modes as a function of rotational speed and boundary conditions. These findings provide valuable insights into the dynamic response of spinning

shafts made of axially graded materials, contributing to a deeper understanding of their vibrational behavior under various operating conditions.

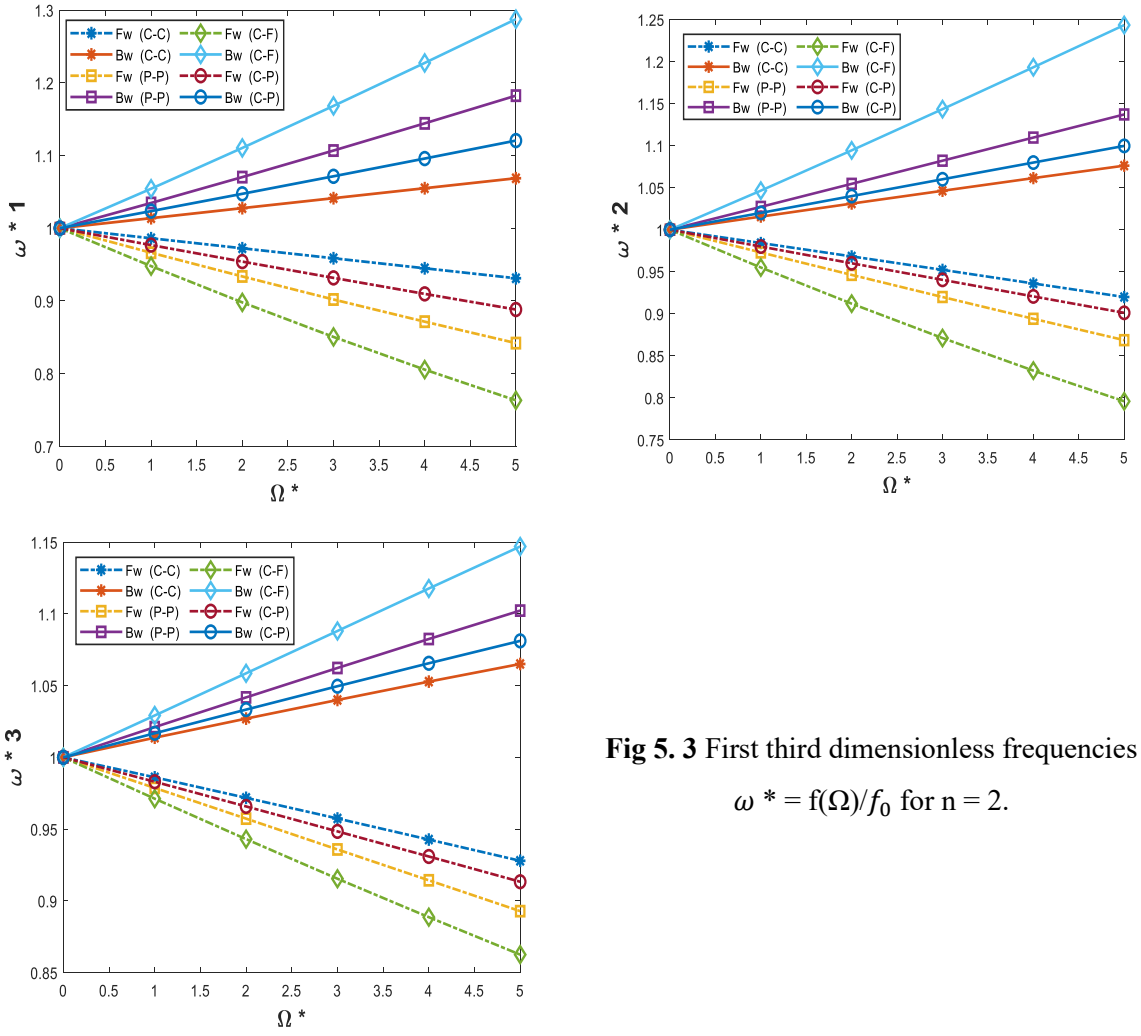

Fig 5. 3 First third dimensionless frequencies $\omega^* = f(\Omega)/f_0$ for n = 2.

5.3.2. Influence of the gradient parameter n, spinning speeds Ω, and boundary conditions

In the second part of the analysis, we investigate the influence of the power-law index n and the rotational speed Ω on a hollow parabolic shaft made from various materials, including a homogeneous material (n = 0) and functionally graded materials (FGMs) with n ranging from 1 to 12. This analysis is carried out under multiple boundary conditions, using the same physical and geometrical parameters as in the previous section. Figure 5.4 illustrates the observed trend: as the rotational speed increases, backward frequencies rise while forward frequencies decrease. In the figure, solid lines represent the backward whirling motion, while dash-dot lines correspond to the forward whirling motion. The dimensionless fundamental whirling

frequencies for these cases at a rotational speed of Ω = 5000 rad/s are summarized in Table 5.9, where the bold values denote the maximum frequencies associated with each boundary condition.

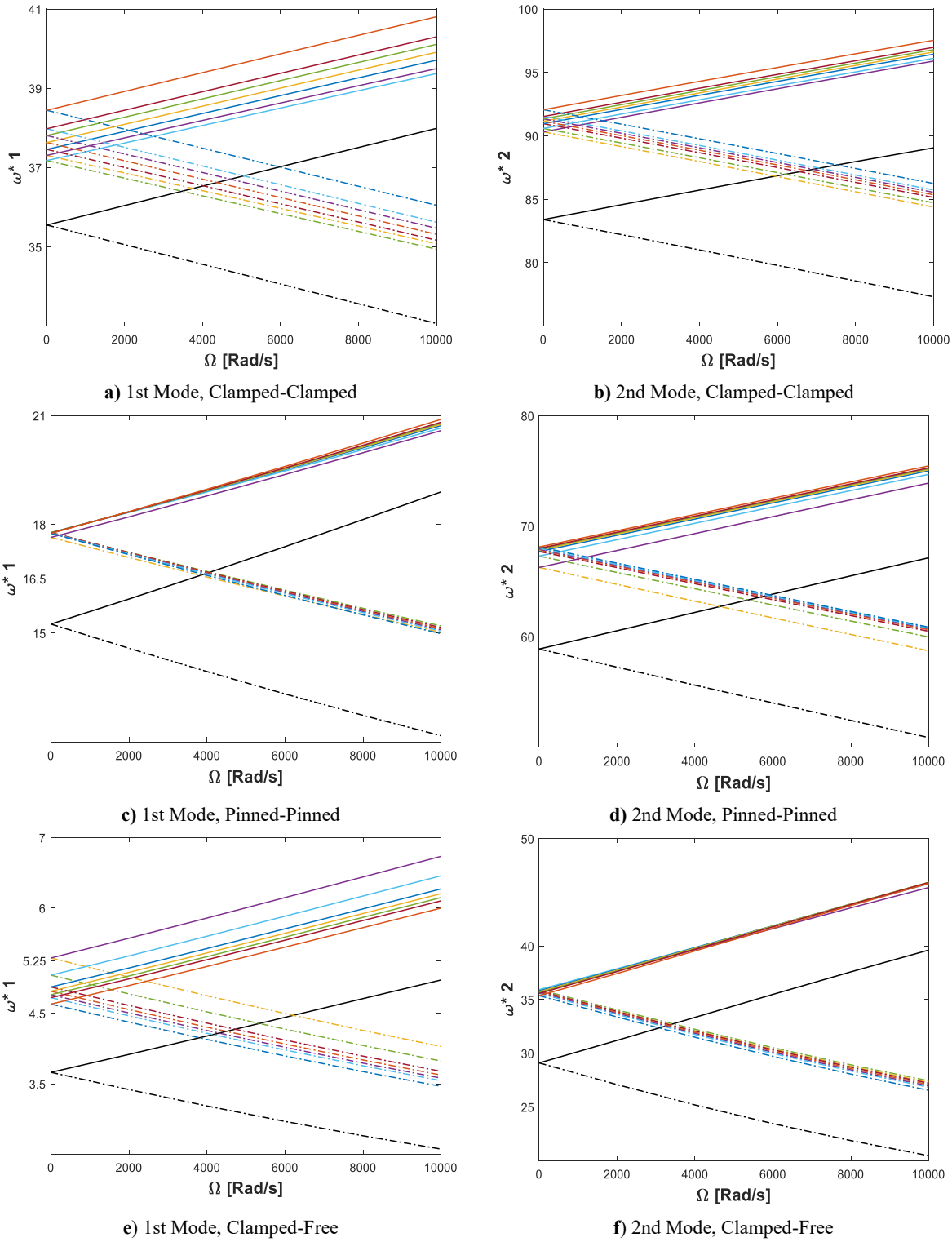

a) 1st Mode, Clamped-Clamped

b) 2nd Mode, Clamped-Clamped

c) 1st Mode, Pinned-Pinned

d) 2nd Mode, Pinned-Pinned

e) 1st Mode, Clamped-Free

f) 2nd Mode, Clamped-Free

Fig 5. 4 Dimensionless frequencies as the n and Ω with different boundary conditions

Furthermore, Figure 5.5 reveals a similar trend, emphasizing the inverse relationship between backward and forward modes. Notably, the first-order dimensionless natural frequency experiences a pronounced increase when the index n changes from 0 to 1. For values n ≈ 1 a peak typically occurs across different boundary conditions, beyond which the frequency either increases or decreases gradually with further increases in n. Under clamped–clamped (C–C) boundary conditions, however, instability is observed in the frequency behavior for the range 1≤ n ≤7, as reflected in Figure 5.5 and Table 5.9.

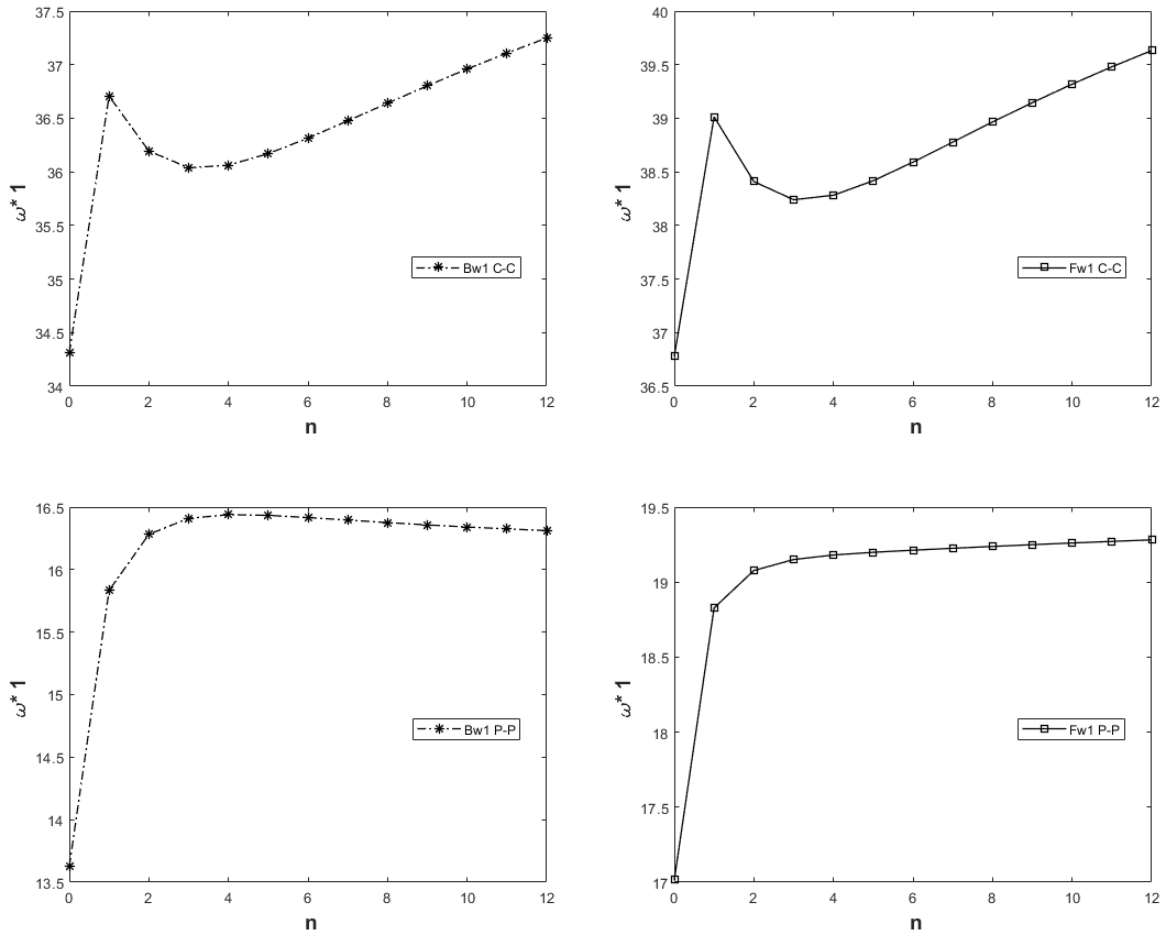

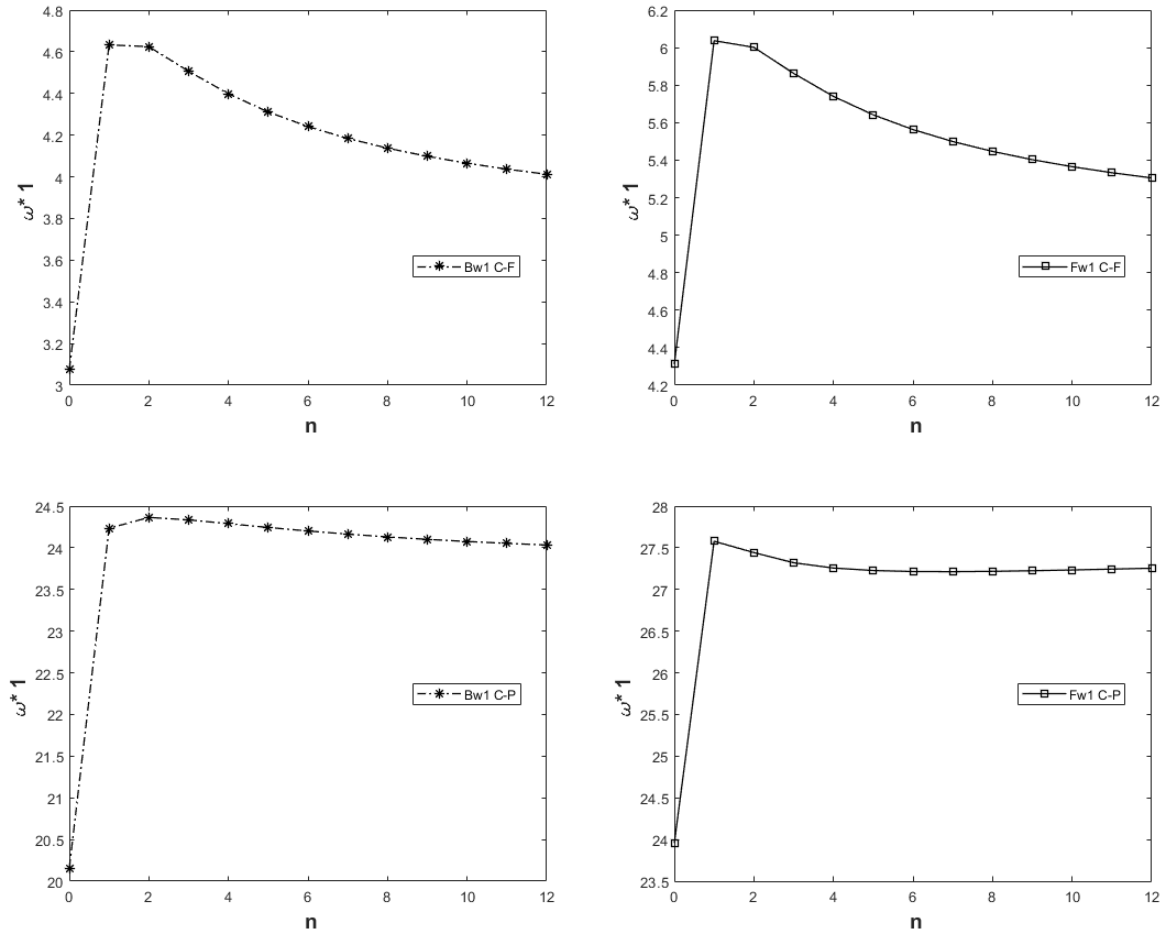

Fig 5. 5 Fundamental whirling frequency for different material gradient index and boundary conditions.

This instability can be attributed to both physical and numerical factors. The nonlinear variation of Young's modulus E(x) and density ρ(x), shown in Figure 1.16, modifies the rotor's stiffness and mass distribution, resulting in discontinuities in the frequency response. Additionally, the non-uniform geometry of the parabolic hollow shaft introduces a nonlinear distribution of bending and torsional stiffness, which can lead to localized changes in the system's dynamic behavior.

Table 5. 9 First fundamental whirling frequency with material gradient index and different boundary conditions, Ω = 5000rad/s

	C-F		C-P		P-P		C-C	
n	Bw_1	Fw_1	Bw_1	Fw_1	Bw_1	Fw_1	Bw_1	Fw_1
0	3.074	4.3122	20.1566	23.9569	13.6254	17.0148	34.311	36.7787
1	**4.633**	**6.037**	24.2341	27.5782	15.8338	18.8281	**36.7063**	**39.0136**
2	4.6245	6.0015	**24.3641**	**27.4424**	16.282	19.0772	36.1945	38.4095
3	4.5065	5.8626	24.3345	27.3202	16.4105	19.1506	36.0379	38.2397
4	4.3986	5.74	24.2893	27.2571	**16.4394**	**19.1808**	**36.0622**	**38.282**
5	4.3112	5.6416	24.2438	27.2272	16.4338	19.1987	36.1697	38.4171
6	4.2411	5.563	24.2015	27.2152	16.4165	19.2127	36.3151	38.5909
7	4.1842	5.4992	24.1637	27.2134	16.3962	19.2256	**36.4761**	**38.7778**
8	4.1374	5.4466	24.1303	27.2174	16.3761	19.2378	36.6409	38.965
9	4.0983	5.4025	24.101	27.2247	16.3575	19.2496	36.8032	39.1462
10	4.0652	5.3651	24.0754	27.2339	16.3407	19.2608	36.9595	39.3184
11	4.0368	5.333	24.0529	27.244	16.3256	19.2715	37.1082	39.4803
12	4.0122	5.3051	24.0331	27.2546	16.3121	19.2817	37.2486	39.6316

This phenomenon is consistent with the findings reported by Yagci et al. (2009), Huang et al. (2018), and Li et al. (2021), who showed that beams with non-uniform geometrical characteristics exhibit comparable variations in natural frequencies. In the clamped–clamped (C–C) configuration, the observed instability is attributed to the reorganization of eigenmodes induced by gyroscopic effects, which is further exacerbated by the rigidity of the boundary conditions.

The bold values in Table 5.9 indicate the maximum whirling frequencies corresponding to each boundary condition. The analysis presented in Figures 5.4 and 5.5, along with Table 5.9, underscores the significant influence of axially functionally graded materials on the system's whirling behavior. These frequencies undergo a marked shift due to the material gradation.

At a rotational speed of Ω = 5000 rad/s, the first pair of dimensionless forward and backward whirling frequencies for the homogeneous profile are 3.074 and 4.3122, respectively. In contrast, for the FGM shaft with a power-law index of n = 1, these values increase to 4.633 and 6.037, corresponding to an increase of approximately 51.71% and 40%, respectively. This demonstrates the substantial effect of material gradation on the dynamic response of rotating non-uniform structures.

5.3.3. Influence of the radius coefficient a, spinning speeds Ω, and boundary conditions

Furthermore, Figure 5.6 presents the influence of the radius coefficient *a*, rotational speed Ω and various boundary conditions on the natural frequencies of a rotating shaft system. The radius coefficient *a* has a direct impact on the rotor's stiffness: as *a* increases, the stiffness of the structure is enhanced, resulting in elevated natural frequencies. This trend is observed consistently across all boundary conditions and rotational speeds. The rotational speed Ω also plays a key role in modifying the vibrational behavior. Specifically, the natural frequencies associated with the forward whirl modes increase with higher Ω, reflecting an augmentation in dynamic stiffness. In contrast, the backward whirl modes exhibit a decrease in natural frequencies as Ω increases, which may potentially raise the risk of dynamic instability at high speeds. The boundary conditions further modulate this response: the clamped–clamped (C–C) configuration yields the highest natural frequencies due to its increased constraint, compared to other support types.

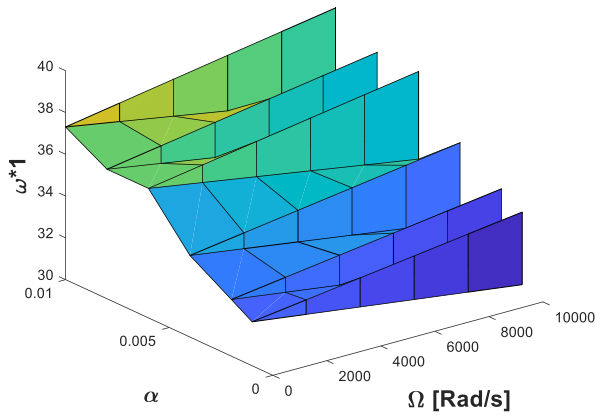

a) 1st Mode, Clamped-Clamped

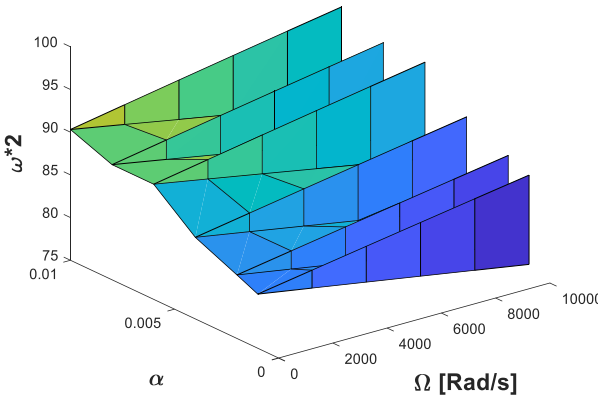

b) 2nd Mode, Clamped-Clamped

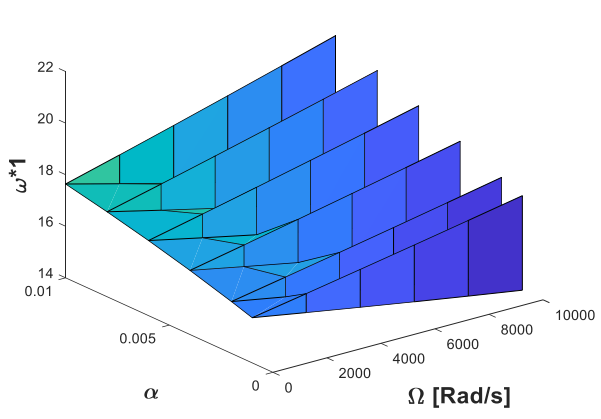

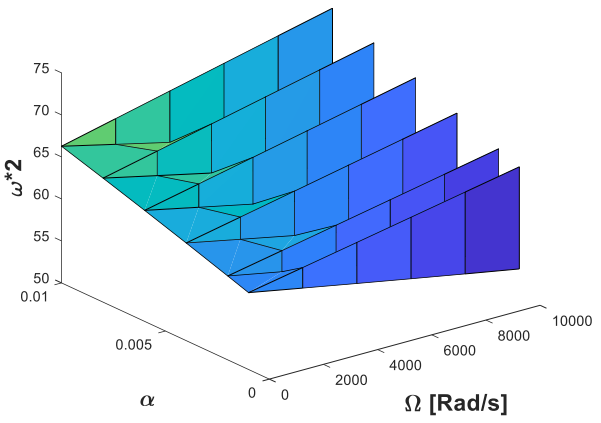

c) 1st Mode, Pinned-Pinned

d) 2nd Mode, Pinned-Pinned

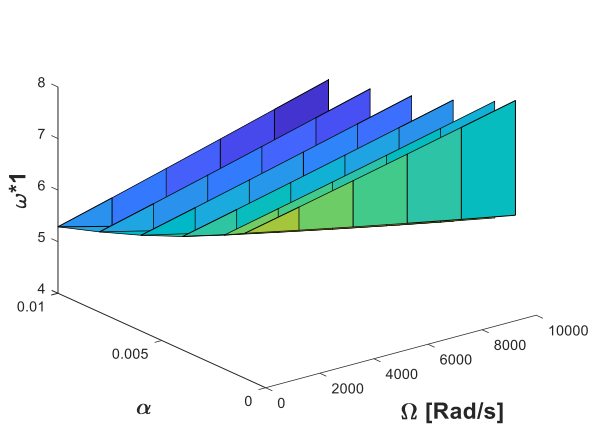

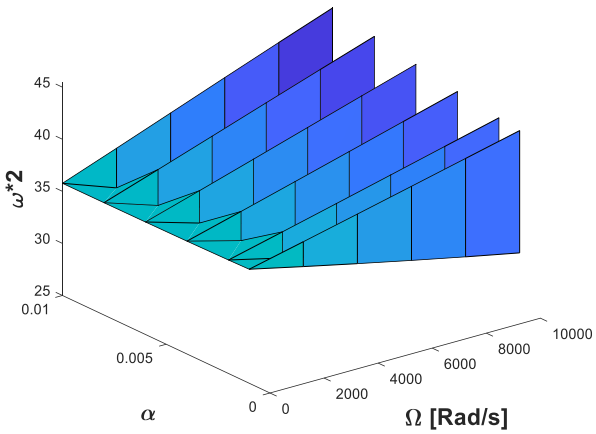

e) 1st Mode, Clamped-Free

f) 2nd Mode, Clamped-Free

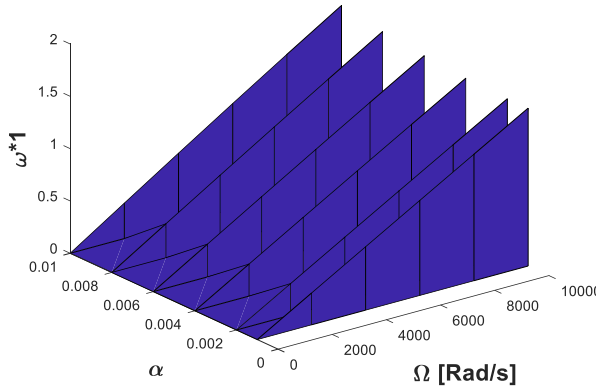

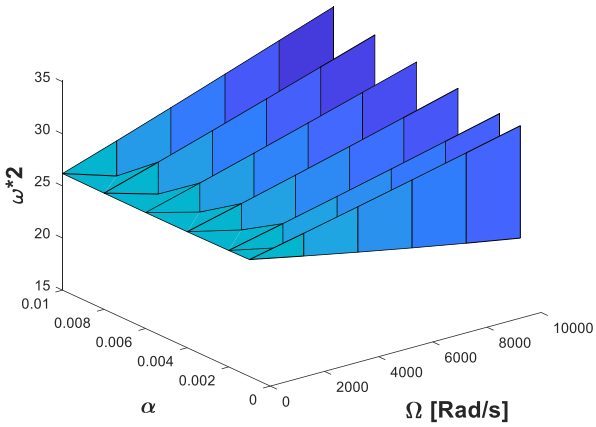

g) 1st Mode, Pinned -Free

h) 2nd Mode, Pinned -Free

Fig 5. 6 Backward and Forward fundamental whirling Variation of $\boldsymbol{\alpha}$ and **Ω** for beams with different boundary conditions

Clamped–clamped (C–C) configurations indicate the highest stiffness, resulting in the highest natural frequencies. In contrast, pinned–pinned (P–P) systems exhibit comparatively lower stiffness and reduced frequencies, while clamped–free (C–F) and pinned–free (P–F) configurations show the lowest frequency values, reflecting increased structural flexibility. Overall, the interplay between the radius coefficient *a*, rotational speed **Ω**, and boundary conditions governs the vibrational characteristics of the system in a complex manner. In general, increasing either *a* or **Ω** tends to elevate the natural frequencies of forward whirl modes, whereas backward modes are progressively reduced as rotational speed rises. Among the boundary conditions, clamped configurations offer the highest dynamic stiffness, leading to elevated natural frequencies compared to more flexible support types.

5.3.4. Influence of the gradient parameter n, radius coefficient *a* and boundary conditions.

This section investigates the influence of the radius coefficient *a*, the power-law index n, and various boundary conditions (BCs) on the dynamic response of a hollow shaft with a parabolic geometry. Figure 5.7 illustrates the variation in dimensionless natural frequencies as functions of these parameters. The results reveal that, for both pinned–pinned (P–P) and clamped–clamped (C–C) configurations, the natural frequencies consistently increase with higher values of *a* and n. In contrast, under clamped–free (C–F) conditions, the dimensionless frequencies exhibit a decreasing trend with increasing parameters. At lower values of n, particularly in the first vibration mode, the frequencies rise sharply, after which the increase becomes more gradual as n continues to grow. For the pinned–free (P–F) configuration, the first-order dimensionless frequency is zero. As n and *a* increase, the frequencies initially decrease, reaching a minimum around n = 6 and *a* = 0.004, after which they begin to increase steadily. This non-monotonic behavior is attributed to geometric alterations that enhance the structural stiffness and consequently modify the dynamic characteristics of the system.

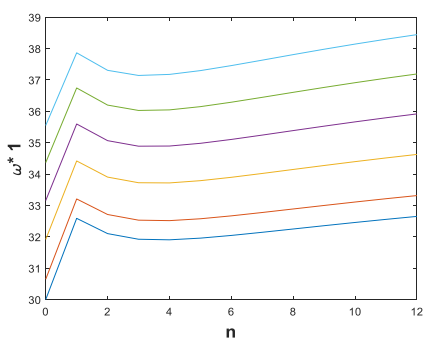

a) 1st Mode, Clamped-Clamped

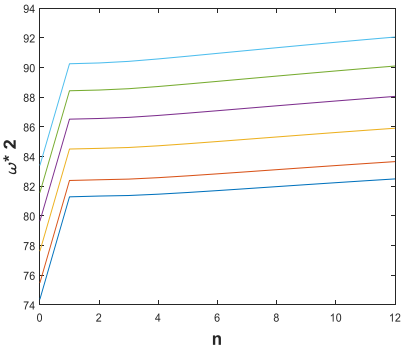

b) 2nd Mode, Clamped-Clamped

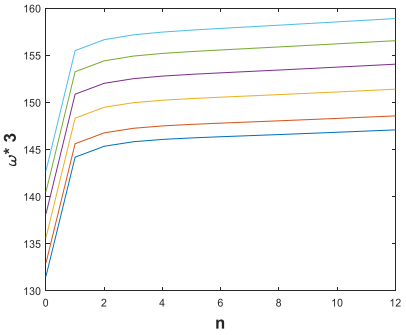

c) 3rd Mode, Clamped-Clamped

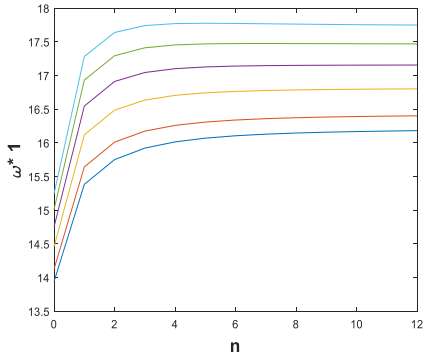

d) 1st Mode, Pinned-Pinned

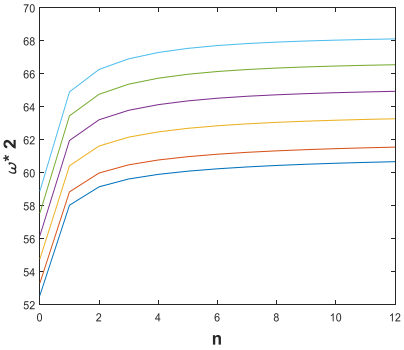

e) 2nd Mode, Pinned-Pinned

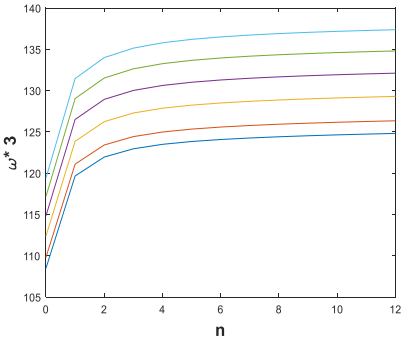

f) 3rd Mode, Pinned-Pinned

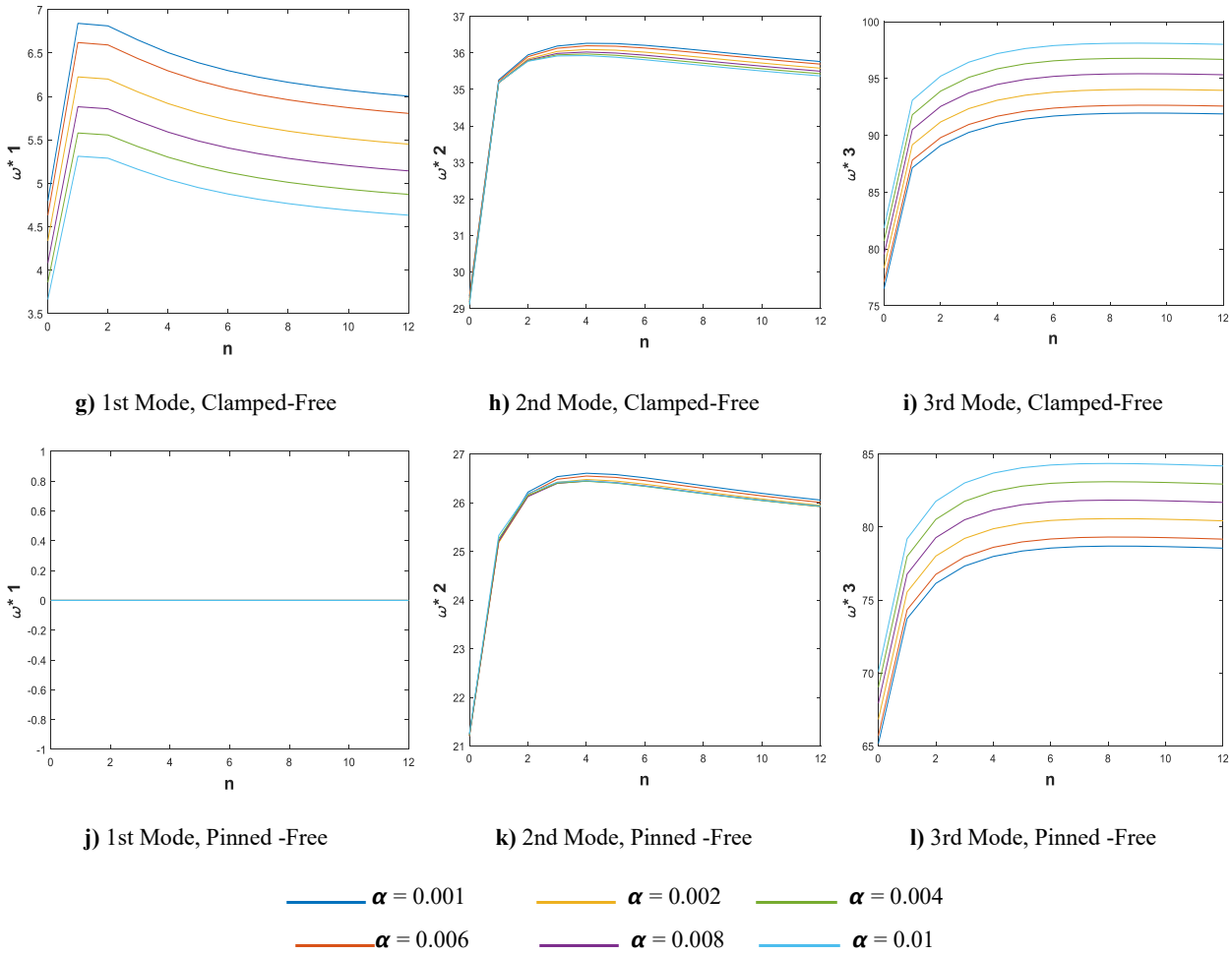

g) 1st Mode, Clamped-Free **h)** 2nd Mode, Clamped-Free **i)** 3rd Mode, Clamped-Free

j) 1st Mode, Pinned -Free **k)** 2nd Mode, Pinned -Free **l)** 3rd Mode, Pinned -Free

Fig 5. 7 First three dimensionless frequencies as a function of n and α for parabolic shaft with different boundary conditions

5.3.5. Influence of slenderness ratio with different boundary conditions

Figure 5.8 illustrates the impact of shaft length on the dimensionless natural frequencies for various boundary conditions in the case of a hollow shaft with a parabolic geometry. Overall, an increase in the slenderness ratio (L/R) leads to a rise in the dimensionless frequencies. This trend is primarily due to the enhanced flexibility of longer shafts, which allows higher vibration modes to emerge despite a reduction in overall structural stiffness. The influence of boundary conditions, however, varies significantly. The clamped–clamped (C-C) configuration consistently yields the highest frequencies across increasing lengths, while the pinned–pinned (P-P) case exhibits lower values due to its reduced constraint. The clamped–free (C-F) configuration displays a distinct behavior: in the first vibration mode, the frequency initially decreases with increasing length, followed by an increase in the higher modes (second and third). This effect is attributed to the interaction between the geometric profile and the flexibility

introduced by the free end, which alters the stiffness distribution along the shaft. These findings underscore the critical role of boundary conditions in shaping the dynamic response of slender shafts and emphasize the importance of selecting appropriate constraints based on the intended engineering application.

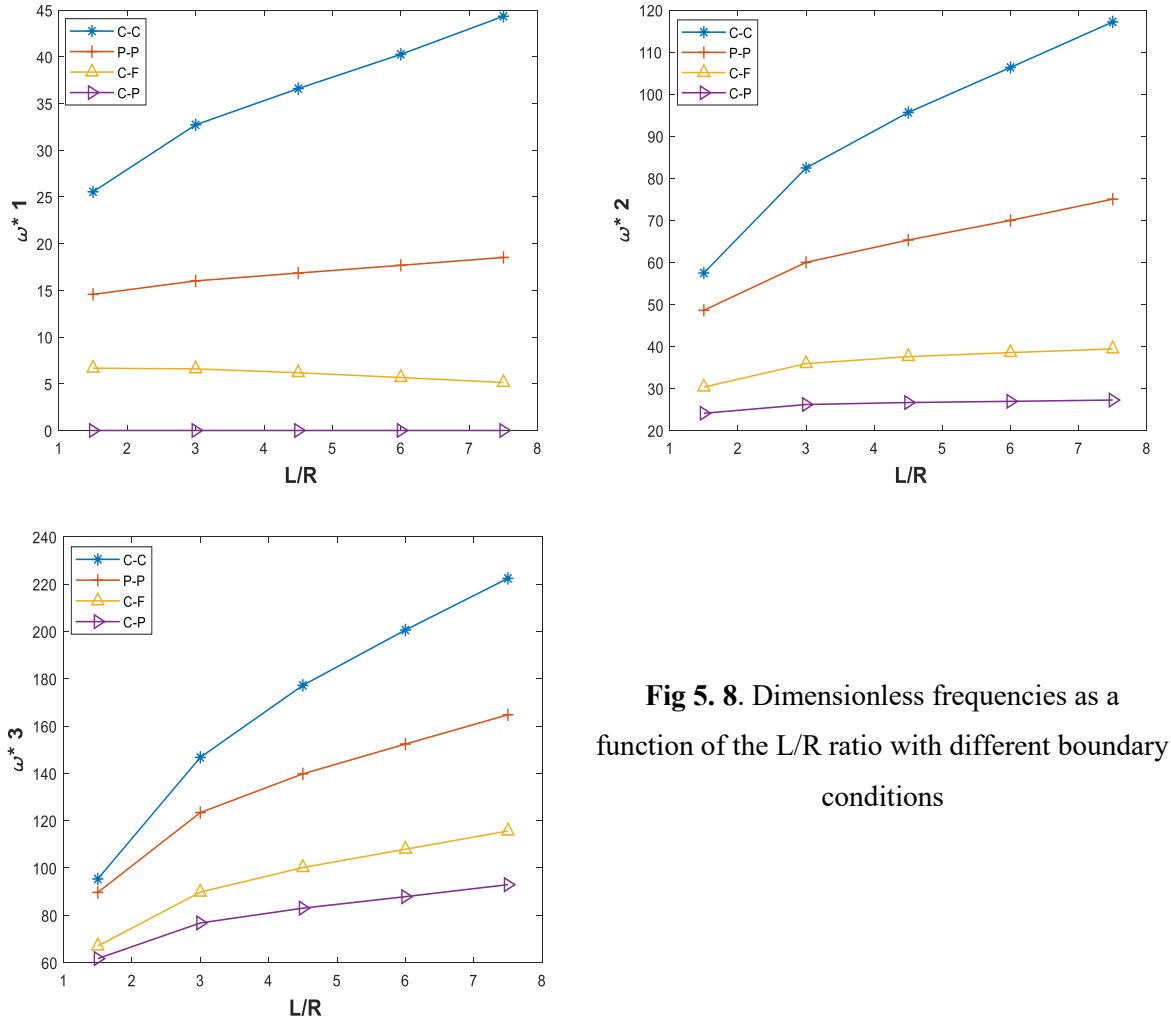

Fig 5. 8. Dimensionless frequencies as a function of the L/R ratio with different boundary conditions

5.3.6. Influence of slenderness ratio with different profiles

Figure 5.9 explores the influence of different shaft profiles on the dimensionless natural frequencies as a function of the slenderness ratio (L/R). For most profiles and boundary conditions, a general trend is observed wherein natural frequencies increase with rising slenderness ratio. However, under the clamped–free (C–F) boundary condition, the hollow parabolic and hollow cylindrical shafts exhibit an atypical behavior: the first natural frequency initially decreases with increasing slenderness, before rising again in the higher modes. This trend corroborates the observations discussed earlier in Figure 5.9. In contrast, solid parabolic and solid cylindrical profiles demonstrate a more uniform increase in natural frequencies across all vibration modes. The distinctive behavior seen in the C–F case is attributed to the combined

effects of free-end flexibility, cross-sectional geometry (hollow versus solid), and axial material gradation. Hollow profiles are particularly sensitive to local flexibility near the free end, leading to a reduction in stiffness for lower modes, while solid profiles preserve more uniform global stiffness. This interaction between boundary conditions, geometric characteristics, and material distribution plays a decisive role in shaping the frequency response, especially in the fundamental mode.

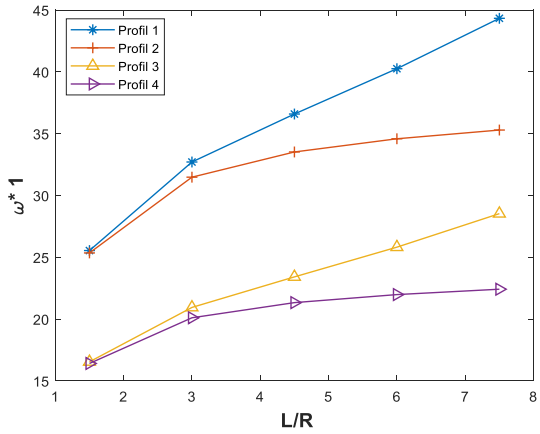

a) 1st Mode, Clamped-Clamped

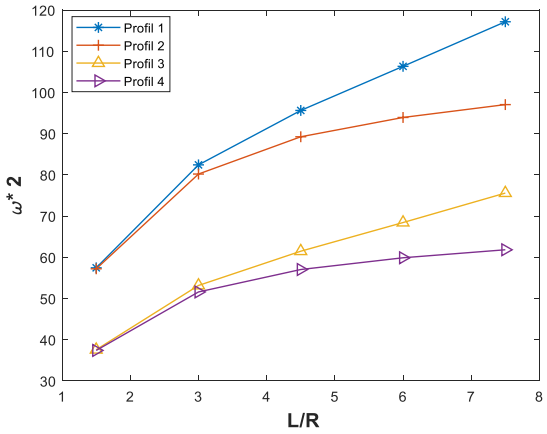

b) 2nd Mode, Clamped-Clamped

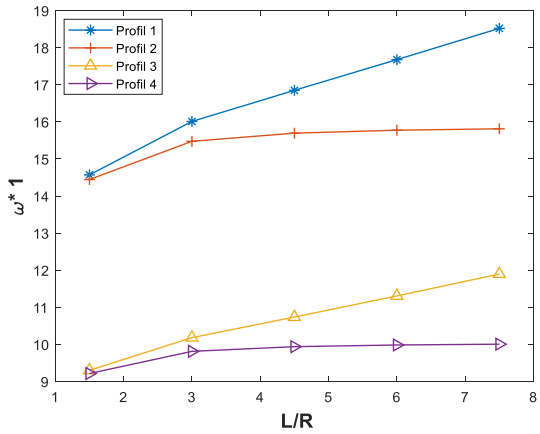

c) 1st Mode, Pinned-Pinned

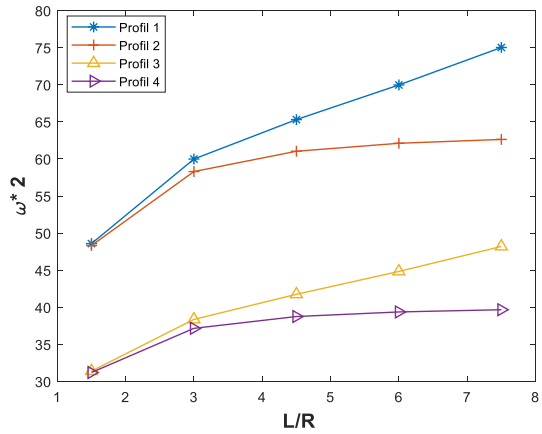

d) 2nd Mode, Pinned-Pinned

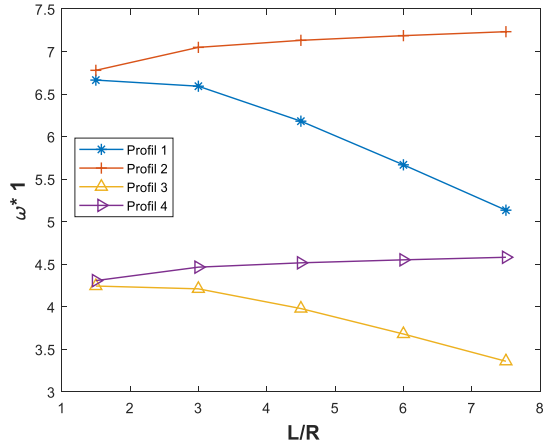

e) 1st Mode, Clamped-Free

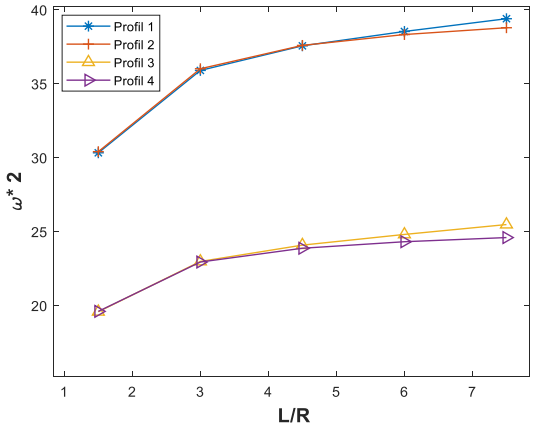

f) 2nd Mode, Clamped-Free

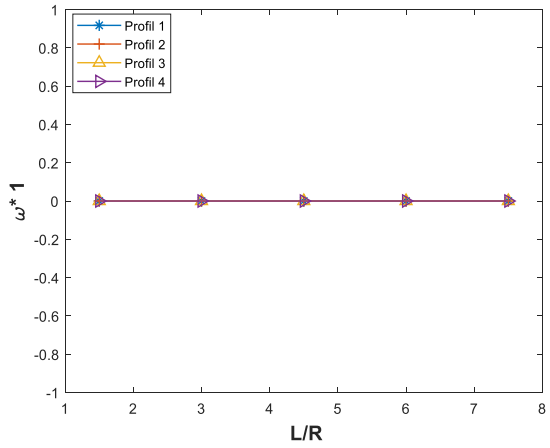

i) 1st Mode, Pinned -Free

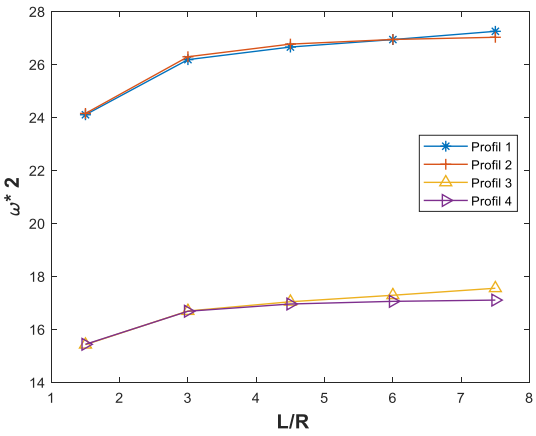

j) 2nd Mode, Pinned -Free

Profile 1 (Hollow parabolic); Profile 2 (Solid parabolic); Profile 3 (Hollow cylindrical); Profile 4 (Solid cylindrical).

Fig 5. 9 Dimensionless frequencies as a function of the L/R ratio with different boundary conditions and different profile.

5.4. Conclusions

This research focuses on the dynamic analysis of a hollow spinning shaft with a parabolic geometry, composed of axially functionally graded materials (FGMs). The shaft's material properties are assumed to vary continuously along the axial direction according to a power-law distribution. To model the system, the Timoshenko beam theory is adopted, which incorporates the effects of transverse shear deformation, rotary inertia, and gyroscopic forces. The numerical formulation is based on a hierarchical *p*-version finite element method using trigonometric shape functions, allowing for accurate and efficient simulation. The results demonstrate excellent consistency with established studies, validating the reliability of the proposed approach. A series of parametric investigations is carried out to assess the impact of key geometric and material parameters on the dynamic performance of the rotating shaft.

1) Convergence and validation

The convergence behavior of the proposed model is verified by progressively increasing the number of shape functions up to p = 10, ensuring the stability and accuracy of the numerical solutions. The obtained results show excellent agreement with benchmark data from the literature, thereby confirming the reliability of the formulation. Furthermore, the validity of the model is substantiated using a two-node beam element for comparative analysis.

2) Gyroscopic effects

The gyroscopic coupling in a hollow parabolic spinning shaft intensifies with larger radius coefficients, markedly shifting the bending natural frequencies for any boundary configuration. This coupling links the two orthogonal lateral motions about the rotation axis, splitting each bending mode into separate backward- and forward-whirl branches.

3) Influence of rotational speed

At higher rotational speeds, the frequencies of the forward precession modes increase, whereas those of the backward modes decrease. This divergence amplifies the gyroscopic effect and significantly alters the overall dynamic response of the spinning shaft.

4) Impact of material composition and geometry

The dynamic behavior of a hollow parabolic spinning shaft composed of axially functionally graded materials (FGMs), particularly its natural frequencies, is strongly influenced by the power-law index governing the material distribution. Moreover, the fundamental dimensionless

frequency can be effectively tuned by varying the radius coefficient or altering the volume fraction distribution of the constituent materials, offering a practical means for optimizing the shaft's dynamic performance.

5) Effect of boundary conditions

The clamped–clamped (C–C) configuration yields the highest natural frequencies, attributed to its maximum structural rigidity. In contrast, the pinned–pinned (P–P) and clamped–free (C–F) conditions introduce increased flexibility, resulting in lower frequency values. Interestingly, for the C–F case, the first natural frequency exhibits an initial decrease followed by an increase in higher modes. This non-monotonic behavior arises from the interplay between the free-end flexibility, parabolic geometry, and axial gradation of material properties.

These results highlight the critical role of boundary conditions, geometric design, and material distribution in the dynamic performance of axially graded rotating shafts. A thorough understanding of these influences is essential for the optimal design, stability enhancement, and structural reliability of functionally graded rotating components in advanced engineering systems.

The present work opens several promising directions for future research. A first extension could involve developing a model that incorporates internal damping and disk flexibility in the case of a rotor made of Functionally Graded Materials (FGMs). Such an approach would enhance the accuracy of the dynamic analysis and provide a more realistic representation of the system's behavior.

Furthermore, considering the effects of hydrodynamic (oil) bearings and external excitations, such as aerodynamic unbalance, thermal variations, or seismic disturbances, would allow for a deeper understanding of transient phenomena and the dynamic stability of rotating systems.

Another important perspective concerns the experimental validation of the numerical results. Setting up a dedicated test rig would make it possible to compare theoretical predictions with measured data, thus ensuring the reliability and applicability of the proposed model.

Finally, the integration of Artificial Intelligence (AI) and Machine Learning (ML) techniques into rotor dynamics analysis represents an innovative and forward-looking research direction. These methods could be employed for the prediction of critical speeds, early detection of instability, and optimization of the dynamic behavior of FGM rotors under various operating conditions.

5.5. References

1. Phoenix Rotor ™ Frame 6B. 6
2. La E, Borel L (2005) Copyright 2001-2005 Gicquel Renaud. 40–43
3. 2025_audi_q6_e-tron_119_1600x1200
4. Lin L, He M, Ma W, Wang Q, Zhai H, Deng C (2022) Dynamic Characteristic Analysis of the Multi-Stage Centrifugal Pump Rotor System with Uncertain Sliding Bearing Structural Parameters. Machines 10:. https://doi.org/10.3390/machines10060473
5. IMG_9572-1184x888
6. S.P. Timoshenko (1921) On the correction for shear of the differential equation for transverse vibrations of prismatic bars. The London, Edinburgh, and Dublin Philosophical Magazine and Journal of Science 41:744–746
7. Screenshot 2025-07-22 at 13-35-17 Pysb-1324 Cone Drive Shaft - Crusher Parts and Conical Fitting
8. adar BakhshBaloch Q (2017) adar BakhshBaloch Q (2017) Covariance-free structure analysis of health-related indicators in older people living at home, focusing on subjective health. Title. 11:92–105. 11:92–105
9. Rao JS (2011) Rotor Dynamics Methods. History of Mechanism and Machine Science 20:185–251. https://doi.org/10.1007/978-94-007-1165-5_14
10. Saleh B, Jiang J, Ma A, Song D, Yang D (2019) Effect of Main Parameters on the Mechanical and Wear Behaviour of Functionally Graded Materials by Centrifugal Casting: A Review. Metals and Materials International 25:1395–1409. https://doi.org/10.1007/s12540-019-00273-8
11. Anastasiou E, Lorentz KO, Stein GJ, Mitchell PD (2014) Prehistoric schistosomiasis parasite found in the Middle East. The Lancet Infectious Diseases 14:553–554. https://doi.org/10.1016/S1473-3099(14)70794-7
12. Veres C, Tănase M (2025) A Bibliometric Review of 3D-Printed Functionally Graded Materials, Focusing on Mechanical Properties. Machines 13:. https://doi.org/10.3390/machines13030232
13. Chauhan PK, Khan S (2019) Microstructural examination of aluminium-copper functionally graded material developed by powder metallurgy route. Materials Today:

Proceedings 25:833–837. https://doi.org/10.1016/j.matpr.2019.10.007

14. Sola A, Bellucci D, Cannillo V (2016) Functionally graded materials for orthopedic applications – an update on design and manufacturing. Biotechnology Advances 34:504–531. https://doi.org/10.1016/j.biotechadv.2015.12.013

15. Lin D, Li Q, Li W, Zhou S, Swain M V. (2009) Design optimization of functionally graded dental implant for bone remodeling. Composites Part B: Engineering 40:668–675. https://doi.org/10.1016/j.compositesb.2009.04.015

16. Marianna Coelho DR and K-UB (2016) Computational Modeling, Optimization and Manufacturing Simulation of Advanced Engineering Materials

17. Mannan S, Knox JP, Basu S (2017) Correlations between axial stiffness and microstructure of a species of bamboo. Royal Society Open Science 4:. https://doi.org/10.1098/rsos.160412

18. Saleh B, Jiang J, Ma A, Song D, Yang D, Xu Q (2020) Review on the Influence of Different Reinforcements on the Microstructure and Wear Behavior of Functionally Graded Aluminum Matrix Composites by Centrifugal Casting. Metals and Materials International 26:933–960. https://doi.org/10.1007/s12540-019-00491-0

19. Ganapathysubramanian S, Zabaras N (2002) A continuum sensitivity method for finite thermo-inelastic deformations with applications to the design of hot forming processes. International Journal for Numerical Methods in Engineering 55:1391–1437. https://doi.org/10.1002/nme.543

20. Hack E, Fruehmann RK, Roos R, Feligiotti M, Schuetz P, Tyler JP, Dulieu-Barton JM (2015) Flaw and damage assessment in torsionally loaded CFRP cylinders using experimental and numerical methods. Composite Structures 132:109–121. https://doi.org/10.1016/j.compstruct.2015.05.025

21. Murugan S B, Behera R (2024) Finite Element Modelling and Dynamic Stability Analysis of a Functionally Graded Rotor Shaft-Bearing System. pp 315–324

22. Shi Z, Yao X, Pang F, Wang Q (2017) An exact solution for the free-vibration analysis of functionally graded carbon-nanotube-reinforced composite beams with arbitrary boundary conditions. Scientific Reports 7:1–18. https://doi.org/10.1038/s41598-017-12596-w

23. (2010) Free vibration analysis of an embarked rotating composite shaft using the hp-

version of the FEM NOMENCLATURE. 7:105–141

24. Endris S (2008) Gene Conserve - Articles - Gene Conserve - Articles - Articles - Volume 7 - Issue 30 - October / December , 2008 . Production 7:2008–2010. https://doi.org/10.1007/s

25. Amira S (2022) Modeling of Functionally Graded structures behavior Modélisation du comportement des structures en Matériaux Fonctionnellement Gradués (FGM).

26. Ford RG (2015) Functionally Graded

27. Li Y, Feng Z, Hao L, Huang L, Xin C, Wang Y, Bilotti E, Essa K, Zhang H, Li Z, Yan F, Peijs T (2020) A Review on Functionally Graded Materials and Structures via Additive Manufacturing: From Multi-Scale Design to Versatile Functional Properties. Advanced Materials Technologies 5:. https://doi.org/10.1002/admt.201900981

28. Saleh B, Jiang J, Fathi R, Al-hababi T, Xu Q, Wang L, Song D, Ma A (2020) 30 Years of functionally graded materials: An overview of manufacturing methods, Applications and Future Challenges. Composites Part B: Engineering 201:108376. https://doi.org/10.1016/j.compositesb.2020.108376

29. Huang Y, Wang T, Zhao Y, Wang P (2018) E ff ect of axially functionally graded material on whirling frequencies and critical speeds of a spinning Timoshenko beam. Composite Structures. https://doi.org/10.1016/j.compstruct.2018.02.039

30. Udupa G, Rao SS, Gangadharan KV (2014) Functionally Graded Composite Materials: An Overview. Procedia Materials Science 5:1291–1299. https://doi.org/10.1016/j.mspro.2014.07.442

31. Zhao P, Wang S, Guo S, Chen Y, Ling Y, Li J (2012) Bonding W and W-Cu composite with an amorphous W-Fe coated copper foil through hot pressing method. Materials and Design 42:21–24. https://doi.org/10.1016/j.matdes.2012.05.057

32. Kumar S, Murthy Reddy KVVS, Kumar A, Rohini Devi G (2013) Development and characterization of polymer-ceramic continuous fiber reinforced functionally graded composites for aerospace application. Aerospace Science and Technology 26:185–191. https://doi.org/10.1016/j.ast.2012.04.002

33. Udupa G, Shrikantha Rao S, Gangadharan K V. (2012) Future applications of carbon nanotube reinforced functionally graded composite materials. IEEE-International Conference on Advances in Engineering, Science and Management, ICAESM-2012

399–404

34. Kimberly FPR, Oo Z, Sujan D (2015) Microstructure analysis, physical and thermal properties of Al2O3- Al2TiO5 functionally graded ceramics for the application of car brake rot. Pertanika Journal of Science and Technology 23:153–161

35. Ram SC, Chattopadhyay K, Chakrabarty I (2017) High temperature tensile properties of centrifugally cast in-situ Al-Mg2Si functionally graded composites for automotive cylinder block liners. Journal of Alloys and Compounds 724:84–97. https://doi.org/10.1016/j.jallcom.2017.06.306

36. Müller E, Drašar Č, Schilz J, Kaysser WA (2003) Functionally graded materials for sensor and energy applications. Materials Science and Engineering: A 362:17–39. https://doi.org/10.1016/S0921-5093(03)00581-1

37. Niino M, Kisara K, Mori M (2005) Feasibility Study of FGM Technology in Space Solar Power Systems (SSPS). Materials Science Forum 492–493:163–170. https://doi.org/10.4028/www.scientific.net/msf.492-493.163

38. Bharti I, Gupta N, Gupta KM (2013) Novel Applications of Functionally Graded Nano, Optoelectronic and Thermoelectric Materials. International Journal of Materials, Mechanics and Manufacturing 1:221–224. https://doi.org/10.7763/ijmmm.2013.v1.47

39. Herrmann M, Sobek W (2017) Functionally graded concrete: Numerical design methods and experimental tests of mass-optimized structural components. Structural Concrete 18:54–66. https://doi.org/10.1002/suco.201600011

40. Sadollah A, Bahreininejа A, Eskandar H, Abd Shukor M (2013) Optimum Material Gradient for Functionally Graded Dental Implant Using Particle Swarm Optimization. Advanced Materials Research 647:30–36. https://doi.org/10.4028/www.scientific.net/AMR.647.30

41. Anné G, Vanmeensel K, Vleugels J, Van der Biest O (2006) Electrophoretic Deposition as a Novel Near Net Shaping Technique for Functionally Graded Biomaterials. Key Engineering Materials 314:213–218. https://doi.org/10.4028/www.scientific.net/kem.314.213

42. Miao X, Sun D (2010) Graded/gradient porous biomaterials. Materials 3:26–47. https://doi.org/10.3390/ma3010026

43. Abedi G, Sotoudeh A (2012) Journal of Biomaterials Science , A Collagen – Poly (Vinyl

Alcohol) Nanofiber Scaffold for Cartilage Repair. 2445–2455

44. Thieme M, Wieters KP, Bergner F, Scharnweber D, Worch H, Ndop J, Kim TJ, Grill W (2001) Titanium powder sintering for preparation of a porous functionally graded material destined for orthopaedic implants. Journal of Materials Science: Materials in Medicine 12:225–231. https://doi.org/10.1023/A:1008958914818

45. Lee BT, Kang IC, Gain AK, Kim KH, Song HY (2006) Fabrication of pore-gradient Al2O3-ZrO2 sintered bodies by fibrous monolithic process. Journal of the European Ceramic Society 26:3525–3530. https://doi.org/10.1016/j.jeurceramsoc.2005.12.017

46. Akmal M, Khalid FA, Hussain MA (2015) Interfacial diffusion reaction and mechanical characterization of 316L stainless steel-hydroxyapatite functionally graded materials for joint prostheses. Ceramics International 41:14458–14467. https://doi.org/10.1016/j.ceramint.2015.07.082

47. Xiao R, Feng X, Fan R, Chen S, Song J, Gao L, Lu Y (2020) 3D printing of titanium-coated gradient composite lattices for lightweight mandibular prosthesis. Composites Part B: Engineering 193:108057. https://doi.org/10.1016/j.compositesb.2020.108057

48. Cheng J, Xu H, Yan A (2006) Frequency analysis of a rotating cantilever beam using assumed mode method with coupling effect. Mechanics Based Design of Structures and Machines 34:25–47. https://doi.org/10.1080/15367730500501587

49. Boukhalfa A (2014) Dynamic analysis of a spinning functionally graded material shaft by the p - version of the finite element method. Latin American Journal of Solids and Structures 11:2018–2038. https://doi.org/10.1590/S1679-78252014001100007

50. Choi ST, Wu J Der, Chou YT (2000) Dynamic analysis of a spinning Timoshenko beam by the differential quadrature method. AIAA journal 38:851–856. https://doi.org/10.2514/2.1039

51. Aouinat AL, Boukhalfa A, Belalia SA (2023) Analytical Solution Using the State-Space Method for Free Vibration Analysis of Rotating Functionally Graded Nanotubes. Journal of Vibration Engineering and Technologies 11:3267–3280. https://doi.org/10.1007/s42417-022-00747-x

52. Rajasekaran S (2013) Free vibration analysis of axially functionally graded tapered Timoshenko beams using differential transformation element method and differential quadrature element method of lowest-order. https://doi.org/10.1007/s11012-013-9847-z

References

53. Shahba A, Attarnejad R, Marvi MT, Hajilar S (2011) Free vibration and stability analysis of axially functionally graded tapered Timoshenko beams with classical and non-classical boundary conditions. Composites Part B: Engineering 42:801–808. https://doi.org/10.1016/j.compositesb.2011.01.017

54. Li G, Wang G, Ni J, Li L (2021) The vibration analysis of the elastically restrained functionally graded Timoshenko beam with arbitrary cross sections. Journal of Low Frequency Noise Vibration and Active Control 40:1853–1875. https://doi.org/10.1177/14613484211019648

55. Sharma AK, Sharma P, Chauhan PS, Bhadoria SS (2018) Study on harmonic analysis of functionally graded plates using fem. International Journal of Applied Mechanics and Engineering 23:941–961. https://doi.org/10.2478/ijame-2018-0053